Title	Elemental composition analysis of seawater using atomic emission spectroscopy of micro-arc discharge
Author(s)	GAMALEEV, Vladislav
Citation	高知工科大学, 博士論文.
Date of issue	2018-03
URL	http://hdl.handle.net/10173/1865
Rights	
Text version	ETD

Elemental composition analysis of sea water using atomic emission spectroscopy of micro-arc discharge

by

Vladislav Gamaleev

Student ID Number: 1196001

A dissertation submitted to the
Engineering Course, Department of Engineering,
Graduate School of Engineering,
Kochi University of Technology,
Kochi, Japan

in partial fulfillment of the requirements for the degree of
Doctor of Engineering

Assessment Committee:
    Supervisor: Akimitsu Hatta
    Co-Supervisor: Kazuya Kobiro
    Co-Supervisor: Hiroshi Furuta
    Committee Member: Kei Okamura
    Committee Member: Sadao Momota

March 2018

(Intentionally left blank)

Abstract

The subject of this work is to develop a novel technique for on-site identification of elemental composition of deep-sea water. In the present study, a systematic analysis of the microplasma discharge in sea water and optical emission spectra of the plasma is presented in order to develop compact device for on-site measurements. Recently marine resources are taking a lot of attention owing to their growing role in sustainable development. Growing interest to exploration of marine resources and numerous studies on ecology and biochemistry are requiring high precision analysis of sea water. Development of the compact analytical tool could be essential for noted above studies and could make measurements faster and cheaper.

In the first part of the thesis, microplasma discharge in sea water was investigated using a needle-to-plane electrode system with various types of needle electrodes and insulation. A needle-to-plane electrode system was placed with a gap of 10-50 μm in the artificial or natural sea water. A pulse current source, consisting of a MOSFET switch, a capacitance and inductance was used. The sea water between the electrodes performed as resistance for the current source circuit. The circuit parameters were optimized to decrease the breakdown voltage and the microplasma discharge duration to suppress erosion of the electrodes. Using a microgap configuration, micro-arc discharges were reproducibly ignited in the highly conductive sea water at low breakdown voltages below 1 kV. The ignition of micro-arc discharges required not only a critical voltage sufficient for breakdown, but also a critical energy for pre-heating of the sea water, sufficient for bubble formation. In order to significantly decrease the current dispersing into the surrounding water, and to enable more accurate investigation of the pre-heating and bubble formation processes before the breakdown, the side face of needle electrode was insulated. For the first time, it was confirmed that the microplasma discharge was ignited after formation of bubble of a size sufficient to cover entire discharge gap between the electrodes. Influence of the needle electrode insulation on the microplasma discharge parameters was investigated. Mathematical model was developed for more detailed analysis of the discharge process. The modelling showed good agreement with experimental results and confirmed that the needle electrode could be reused for generation of reproducible micro-arc discharges even after erosion caused by the arc by precise tuning the working gap length. Moreover, it was confirmed that the shape of the needle electrodes tip does not affect the measurement of optical emission spectra while, in the case of damaged needle electrode, it required further precise focusing and arrangement of the lens. Possibility of use of damaged needle electrodes could be essential for development of durable measurement tools for on-site analysis of deep-sea water.

In the second part of the thesis, possibility of atomic emission spectroscopy of micro-arc discharges operated in sea water for elemental composition analysis has been studied. The discharge process and optical emission spectra from micro-arc discharges have been analyzed in three types of liquid, namely artificial sea water composed of 10 main components, reference solutions each containing a single component, and naturally sampled deep sea water. Micro-arc discharges were operated under low breakdown voltage using the needle-to-plane electrode system immersed into each liquid in a quartz cuvette. In the spectra, the emission peaks for the main components of sea water and contaminants from the electrodes were detected. Owing to the complex composition of sea water, spectra from discharges in reference solutions were compared for assignment of the emission peaks. The proposed method showed good potential for detection of Fe and other metals in sea water. Using the present setup, it was possible to detect Fe impurities at a concentration of 300 ppm. To study the effect of materials of the electrodes on the optical emission spectra and plasma parameters, three types of needle electrodes were used. Effect of the experimental conditions on measured optical emission spectra was studied, and applicability of proposed method for on-site composition analysis was confirmed. The plasma parameters of electron temperature and electron density in the micro-arc discharge were also investigated by analysis of broadening of Hydrogen atomic emission peaks.

In the third part, micro-arc discharges generated in sea water at high pressure were investigated. For generation of micro-arc discharges, electrodes were introduced into a high pressure chamber and a current pulse was supplied by the same pulse current source as for the atmospheric pressure case. By using pin-to-pin electrodes system, micro-arc discharges were successfully generated in highly conductive sea water at high pressure up to 17.5 MPa for the first time. Analysis of current and voltage waveforms showed that micro-arc discharge process at high pressure was same to the atmospheric pressure case and could be divided into three phases; pre-heating, micro-arc discharge and subsequent oscillation. A difference to atmospheric pressure was increase of power consumption during pre-heating phase with increase of pressure. Use of pin-to-pin electrode system with insulation of side faces allowed us to generate micro-arc discharges with relatively low energy even at high pressure due to concentration of strong electric field between the electrodes with a small volume. Due to erosion of the electrodes caused by high current during the discharge, however, repetition number of reproducible discharges using same electrodes was limited below 30. A rod-to-rod electrode system consisting of two parallel metal rods aligned with a small gap was developed instead. In the case of rod-to-rod electrode system, due to increase of the surface of the facing electrodes, local erosion caused by high current does not have significant impact on the reproducibility of the discharges while the energy increased by 30% compared to the pin-to-pin electrode system due to increased volume between the electrodes in the gap. By using the rod-to-rod electrode system, it was succeeded to generate reproducible micro-arc discharges at high pressures up to 19 MPa due to improved durability of the electrodes. The reproducible discharge enabled to analyze the effect of pressure on the power consumption during pre-heating phase. It has been confirmed, that increase of pressure results in increase of power required for pre-heating phase. It was evaluated that preheating energy at 19 MPa was seven times larger than for the atmospheric pressure case.

Acknowledgements

Foremost, I would like to acknowledge my supervisor *Prof. Akimitsu Hatta* for having faith in my abilities and giving me the chance to study at Kochi University of Technology. I would like to express my gratitude to him for guiding me, providing me with valuable feedback that helped me deal with many challenging problems as well as for encouragement and support during my study.

I would like to express my very sincere gratitude to *Assoc. Prof. Hiroshi Furuta* and *Prof. Kazuya Kobiro* for being very good advisors during the course of study. Their ideas and comments very indispensable and allowed me to improve my work many times. I am thankful *Prof. Kei Okamura* and *Assoc. Prof. Sadao Momota*, for their great help, advice, and valuable feedback during the preparation of this thesis.

I am thankful to all the members of the Hatta-Furuta laboratory for their assistance during my research. I am especially thankful to *Dr. Jun-Seok Oh*, for his countless advice, ideas, and guidance. Big appreciation to my fellow doctoral students *Udorn Junthorn, Adam Pander,* and *Md Abdullah Al Mamun* for being great friends during the last years. I'm also thankful to my Japanese friends *Kotaro Ogawa, Kouki Ishimoto, Hiroki Miyaji*, *Hideki Yajima* and *Keisuke Noguchi* for many interesting discussions and relaxing times. Their presence in the laboratory always introduced a spark of happiness to my daily life.

I am also very thankful to the staff members of International Relations Division for their support, hard work and commitment. I'm especially grateful to *Mikako Takataru, Miki Okauchi*, *Saki Hamamura* and *Yoko Morio* for being great help and support during my study. Nevertheless, I am also grateful to *Prof. Shinichiro Sakikawa* for his time, guidance, big help and countless advice regarding Japanese and university life. I am very thankful to *I-house advisor Shane Yoshida* for his help and support during my stay in KUT.

I had a chance to meet many extraordinary and interesting people, some of whom became my very close friends. First of all, I would like to thank *Sergey, Michelle, Yuki, Rika*, *Erina*, *Hiyori, Chika* and *Yuka* for the introduction to the Japanese culture and life. Also big thanks to *Adam, Ono, Rebecca*, *Peter* and *Cristina*, for being great friends both in the moments of happiness and trouble. And finally, I would really like to thank *Katada and Yoshita families* from Kanazawa, for their hospitality and all the good memories we have made together.

Special thanks to *Shoko Suesada* for countless talks in Japanese, introduction to Japanese culture and for being a very good friend. Mostly because of this communication I can finally speak Japanese.

I would also like to thank my *Russian friends*, with whom, despite the big distance, I was able to keep contact. Their endless jokes and comments made my life happier during the last 3 years I have spent in Japan.

Finally, I take this opportunity to express my profound gratitude to *my family* for supporting me in my decisions, for the unconstrained encouragement, and truthful love they have shown me all these years.

This research was supported by JSPS KAKENHI Grant (no. 26600129).

Disclaimer

Some passages in this work have been quoted *verbatim* from the previous publications and work of the author (listed according to the state in time of writing the thesis):

Journal Papers:

1) V. Gamaleev, H. Furuta, A. Hatta, *"Detection of metal contaminants in seawater by spectral analysis of micro-arc discharge"*, Japanese Journal of Applied Physics (Selected Topics in Applied Physics, Plasma in Solution and Its Applications), Vol. 57, no. 1, p. 0102B8, 2018
2) V. Gamaleev, Y. Hashimoto, J.-S. Oh, H. Furuta, A. Hatta, *"Investigation of Effect of Needle Electrode Configuration on Microplasma Discharge Process in Sea Water"*, IEEE transactions on Plasma Science, vol. 45, no. 4, pp. 754-760, 2017
3) V. Gamaleev, Y. Okamura, K. Kitamura, Y. Hashimoto, J.-S. Oh, H. Furuta, A. Hatta, *"Investigation of microplasma discharge in sea water for optical emission spectroscopy"*, Japanese Journal of Applied Physics, vol. 55, no. 7S2, p. 07LC03, 2016.

Conference Publications:

1) Gamaleev V., Furuta H., Hatta A., *"Investigation of micro-arc discharge in seawater"*, 6th International Symposium on Frontier Technology (November 5-6, 2017, Kochi University of Technology, Kami, Japan), Book of abstracts, pp. 217-220.
2) Gamaleev V., Furuta H., Hatta A., *"EFFECT OF THE LOCAL PROCESSES IN THE DISCHARGE GAP ON MICRO-ARC GENERATION IN SEA WATER",* Proceeding of the XIII International Conference "Gas-discharge Plasma and Its Application" (September 5-7, 2017, Khristianovich Institute of Theoretical and Applied Mechanics, SB RAS, Novosibirsk, Russia).
3) Gamaleev V., Furuta H., Hatta A., *"Investigation of micro-arc discharge in sea water for chemical composition analysis"*, Proceeding of 23rd International Symposium on Plasma Chemistry (July 30 – August 4, 2017, Montreal, Canada).
4) Gamaleev V., Morita H., Oh J.-S., Furuta H., Hatta A., *"Analysis of microplasma discharge process in sea water"*, Proceedings of the 7th International Workshop on Plasma Spectroscopy (June 26–29, 2016, Meitetsu Inuyama Hotel, Inuyama, Japan), p. O-18.

5) Gamaleev V., Okamura Y., Kitamura K., Hashimoto Y, Oh J.-S., Furuta H., Hatta A., *"INVESTIGATION OF MICROPLASMA DISCHARGE IN SEA WATER"*, Proceedings of the International Scientific - Technical Conference "INTERMATIC - 2015" (December 1-5, 2015, Moscow, Russia), no. 1. pp 51-54.

6) Gamaleev V., Okamura Y., Kitamura K., Hashimoto Y, Oh J.-S., Furuta H., Hatta A., *"Characterization of Microplasma Discharge in Sea Water"*, Proceedings of the Joint Symposium APSPT-9/SPSM-28 (December 12 –15, 2015, Nagasaki Univ., Japan).

7) Gamaleev V., Okamura Y., Kitamura K., Hashimoto Y, Oh J.-S., Furuta H., Hatta A., *"Optical Emission Spectroscopy of Microplasma Discharge in Sea Water"*, Proceedings of the Joint Symposium 9th ICPR/ 68th GEC/ 33rd SPP (October 12–16, 2015 Hawaii Convention Center Honolulu, U.S.A.), ISBN: 978-4-86348-529-7.

All of the quoted sources were originally written by the author of this thesis.

Table of contents

List of figures

List of tables

Abbreviations

UV – ultraviolet

ICP – inductively coupled plasma

ICP-MS – inductively coupled plasma mass spectrometry

LIBS – laser induced breakdown spectroscopy

UPW – ultrapure water

DSW – deep-sea water

ASW – artificial sea water

MOSFET – metal–oxide–semiconductor field-effect transistor

OES – optical emission spectroscopy

TTL – transistor-transistor logic

UV-vis – ultraviolet-visible range

LEP – liquid electrode plasma

PTFE – polytetrafluoroethylene

RLC – resistor (R), inductor (L) and capacitor (C) circuit

FWHM – full width at half maximum

Chapter 1. Introduction

1.1 Background

Currently there is continuous contamination of available water resources by industry and agriculture, which makes pollution control and ecological monitoring necessary for saving water resources. On the other hand, marine resources are taking growing role in the sustainable development of industry. With the growing needs in industrial resources there is significant interest in new sources of materials that can meet the growing demands of the industry. The problem of limited resources available for industry can be solved partially by use of marine resources and underwater deposits [1–4]. There are many researches, dedicated to exploration and use of marine resources; however, due to numerous possible applications and huge amount of water under various condition (temperature, pressure, elemental composition), precise analysis of sea water is complicated [5–8]. In both cases, for the exploration of marine resources and ecological monitoring, a high precision analysis of sea water is required. Moreover, detection of trace amounts of Fe and other metals in sea water is an important topic owing to numerous marine biochemical studies being conducted, such as growth of phytoplankton, chlorophyll production, and nutrition of marine microorganisms. Complex composition of sea water results in problems with identification and separation of the elements (sometimes at low concentrations), which makes composition analysis complicated [5–10].

1.2 Motivation and research issue

There are many methods of determining of the composition of sea water, such as inductively coupled plasma (ICP) mass spectroscopy of sprayed liquid and optical absorption spectroscopy of examined liquid. However, most of these methods are operated in laboratories in specialized locations, require large equipment (depending on the accuracy of measurements, the sizes of laboratory devices can vary from a table top to a room), sampling of water, transport of the samples and sometimes special preparation of the samples before the measurements. The necessity of sampling, long time of analysis, usage of complex equipment and high power consumption makes elemental composition analysis of deep sea water using noted methods complicated, long and costly [5–16]. Most perspective way to solve stated above problems is development of a diagnostic tools which can provide rapid on-site elemental composition analysis and contaminants detection. However, on-site identification of elemental composition of natural deep sea water is still challenging [12–15,17–19].

One of the promising methods to identify elemental composition of water is a spectral analysis of different types of plasmas generated in examined liquid. Plasmas generated in dielectric and low conductivity liquids and plasmas that come in contact with the liquid are studied extensively and are already used in various applications such as water treatment, medicine, nanoparticles formation etc. However, in the case of highly conductive sea water, operation of reproducible plasma discharges directly in liquid is extremely difficult. One of the reasons for that is the main mechanism of plasma discharges in highly conductive liquids. High conductivity of the liquid results in high electric currents through the liquid during the discharge causing Joule heating and local boiling. Upon the formation of vapor bubbles electrical breakdown initiates in a gaseous medium. Conventional systems for generating plasma discharges in water require high voltages (1-100 kV). Necessity in usage of high voltage power supply and complex control units makes development of compact tool for on-site measurements problematic. One of the ways to solve the problem of size is the use of microplasma discharges, which enables the operation of discharges using a compact setup [6,12,13,17–45].

There are many ways to generate microplasmas in highly conductive liquids, such as electrolyte cathode and liquid electrode plasma (LEP), which allows to operate discharges under low voltages (less than 1 kV). Moreover, there are already designed prototypes of on-chip devices for compositional analysis and impurity detection. However, in cases of use of liquid electrodes there are limitations related to adjustment of the discharge gap, generation of the microplasma in liquids with different conductivity, and problems with carrying out experiments in liquid under high pressure [13–15,18,33]. The above-mentioned problems could be solved using electrode system with precisely controlled microgap [18].

Promising approach for the development of compact tool for on-site measurements is use of needle-to-plane or needle-to-needle electrode system with precise micromanipulator, owing to possibility of adjustment of the discharge gap before each discharge. Recent research shows that in the case of microgaps, plasma discharges can be reproducibly ignited in different types of conductive liquids, by applying low voltages to the electrodes. Microplasmas generated using low voltages could be potentially applied to on-site measurements in sea water and elemental composition analysis. For that purpose, atomic emission spectroscopy of short (1-100 μs) microplasma discharges has a big potential, due to its small energy consumption and simple discharge setup. Moreover, usage of micro-arc discharges is perspective for on-site analysis of deep sea water (1 km and more depth), owing to the increase of optical emission intensity of the arc discharges with increase of pressure. On the other hand, in the available research resources there is almost no information about micro-arc discharges generated in highly-conductive liquids at high pressure, and it is important from the scientific point of view to understand the discharge process and perform precise study of it [4,5,8,13–19,46–52].

1.3 Research objectives

The main objective of this dissertation is development of the analytical method for on-site elemental composition analysis of deep sea water. For that purpose, atomic emission spectroscopy of micro-arc discharges in deep sea water is utilized. For development of the analytical method it is important to perform the following studies:

- Investigation of the micro-arc discharge is sea water – understanding of the plasma generation mechanism, study of effect of experimental conditions on plasma parameters, reproducible generation of the plasma and optimized parameters for reproducible discharge.
- Investigation of the optical emission spectra – analysis of the effect of the experimental conditions on recorded OES, reproducibility of measurements, analysis of plasma parameters using OES, elemental composition analysis of the liquid using OES
- Investigation of the micro-arc discharge is sea water at high pressure – understanding of the phenomena and plasma generation mechanism, study of effect of experimental conditions on plasma parameters, reproducible generation of the plasma and optimized parameters for reproducible discharge.

Chapter 2. Research background

2.1 Plasma

Plasma is partially or fully ionized gas, formed by neutral atoms (or molecules) and charged particles (ions and electrons). One of important features of plasma is quasineutrality, which means that volume concentration of positive and negative charged particles, which are forming plasma, are almost same. Gas turns to plasma if some of gas atoms (or molecules) will lose one or more electrons owing to some external impact. Due to interactions in the plasma, negative ions could be formed by attachment of electrodes. If no neutral particles remained in the gas, plasma is called fully ionized [53].

There is no significant border between plasma and gas. Any solid material with increase of temperature starts to melt and finally evaporates (turns to the gas phase). In the case of molecular gas (H_2, N_2), with further increase of temperature gas molecules start to dissociate to single atoms. Further increase of temperature will cause formation of positive ions and free electrons and gas will become ionized. The process of formation of the plasma by introducing more energy to observed system is presented on Figure 2.1. Free electrons can easily move in the medium causing electric current, that's why plasma is also called "conductive gas" [53].

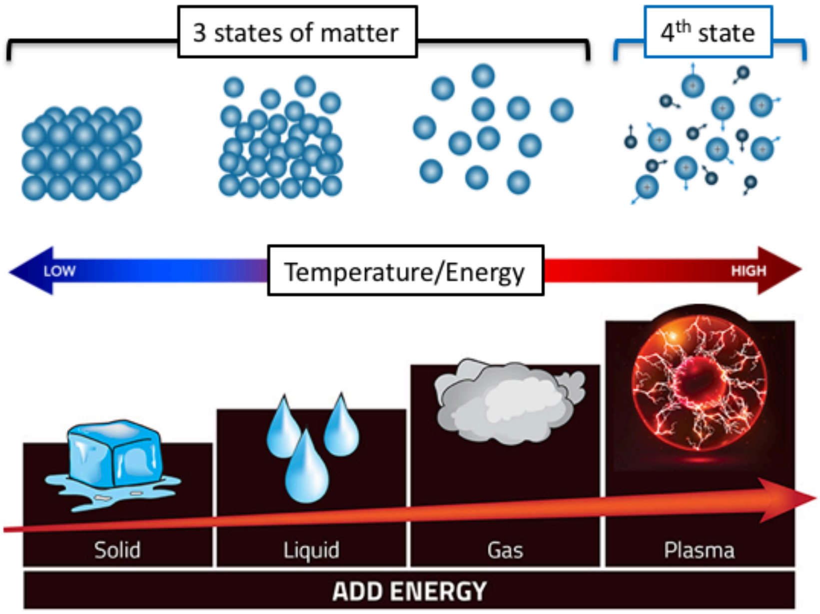

Figure 2.1. Formation of the plasma with increase of the temperature.

Plasma follows most of the principles of the gas physics; however, in some of the cases it acts different. One of the biggest differences in behavior of plasma, comparing to gases, could be observed when plasma interacts with electric or magnetic field, which could be explained by existence of charged particles in the plasma. Due to extraordinary behavior of plasmas in electric and magnetic fields, plasma is also called 4th state of matter. For the first time phenomena of plasma was discovered by William Crookes in 1879. During the study of the electric discharges in glass tubes filled with low pressure air he wrote: “Phenomena in pumped pipes open up for a physical science a new world in which matter can exist in the fourth state”. The term "plasma" for quasineutral ionized gas was introduced by American physicists Langmuir and Tonks in 1923 when they were describing phenomena in a gas discharge. In his article published in the Proceedings of the National Academy of Sciences in 1928, he wrote: “Except near the electrodes, where there are sheaths containing very few electrons, the ionized gas contains ions and electrons in about equal numbers so that the resultant space charge is very small. We shall use the name plasma to describe this region containing balanced charges of ions and electrons.” Until then, the word "plasma" was used only by physiologists and denoted a colorless liquid component of blood, milk or living tissues; however, soon the concept of "plasma" became firmly established in the international physical dictionary and received the widest distribution [53].

Recently plasma technologies are widely used in various fields and having huge impact in our daily lives. Almost all microelectronic devices are produced using plasma processes (plasma-based deposition and etching). Plasma technologies are taking growing role in biomedical sector in such applications as plasma coating (coating of prostheses, such as artificial hips or knee), sterilization of equipment by plasma, plasma treatment of drugs and plasma medicine (treatment of cancer and wounds by non-thermal plasmas).

2.2 Generation of plasma

The way to create a plasma by ordinary heating of the substance, which was described above, is not the most common. To get a thermal ionization of most gases, it is necessary to heat the gas to temperatures of tens and even hundreds of thousands of degrees. Only in vapors of alkali metals (such as potassium, sodium or cesium), the electrical conductivity of the gas can be observed already at 2000-3000 °C. This phenomenon could be explained by the fact that in the atoms of monovalent alkali metals the outer state of electron is much less bounded with the nucleus (has a lower ionization energy), comparing to the atoms of other elements of the periodic system of elements. In such gases at the temperatures indicated above, the number of particles with energy above the ionization point is sufficient to create a weakly ionized plasma.

A common method of obtaining plasma in laboratory conditions and technology is the use of an electric gas discharge. For formation of the gas discharge, two electrodes should be connected to DC power source and placed inside the glass tube, which could be filled by various gasses under various pressure. This simple device is already used for more than 150 years and allows to generate various types of plasma. Current and voltage characteristics of the discharge generated in neon gas at 1 Torr pressure between flat electrodes placed with the gap of 50 cm are presented in Figure 2.2.

After application of small voltage (10-50 V) to the discharge gap, no visible effect could be observed in the gas. However, very sensitive measurement devices could detect very small electric current (about 10^{-15} A) passing through the gap. It could be explained by existence of charged particles in the gas formed by natural sources of radiation (e.g. cosmic rays). Charged particles are moving under effect of electric field generating electric current. Generation of charged particles in the discharge gap could be stimulated by external x-ray or radioactive radiation resulting in increase of current up to 10^{-6} A; however, ionization rate in this case is still not enough for emission of light from the gas. In this case discharge is formed only due to external ionization sources or due to emission of electrons and ions from the electrodes (for example thermal electron emission from cathode). Such a discharge maintained by external sources is called non-self-sustaining discharge (Figure 2.2, region A-B). With increase of voltage, current increases owing to increase of amount of charged particles which can reach electrodes before recombination. However, at some point current saturates (point B on Figure 2.2), due to limitation of ionization rate. With further increase of voltage, after acceleration in the electric field electron reaches enough energy to liberate new free electron after a random collision. The original ionization event liberates one electron, and each subsequent collision liberates a further electron, causing so-called cascade multiplication of carriers or avalanche multiplication. This type of discharge is called the Townsend discharge or Townsend avalanche and corresponds to the B-D region on the Figure 2.2. The A-D region in Figure 2.2 is called a dark discharge. There is some ionization in this type of discharge, but the current is below 10 microamperes and there is no significant amount of radiation produced [53].

With further increase of voltage, at some point current starts to grow rapidly and emission of the light from gas could be observed. This is called breakdown of the gas, which is one of most important processes in the gas discharges. After breakdown, discharge transits to normal glow discharge and becomes self-sustaining. In the Figure 2.2 region D-F corresponds to the breakdown and transition to normal glow discharge and region G corresponds to normal glow discharge [53–55].

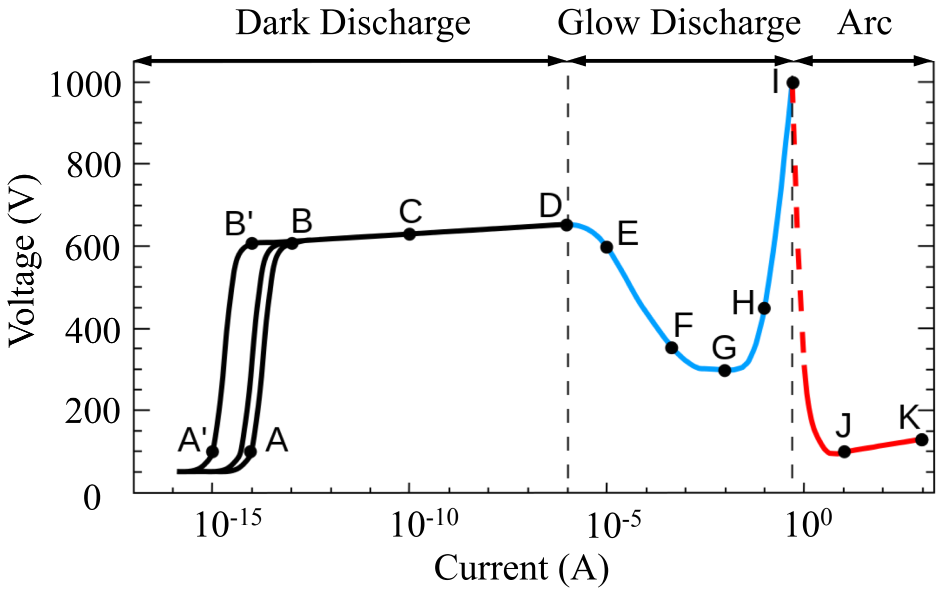

Figure 2.2. Voltage versus current characteristics for neon gas at 1 Torr pressure between flat electrodes spaced 50 cm. **A**: random pulses caused by cosmic radiation, **B**: saturation of the current, **C**: avalanche Townsend discharge, **D**: self-sustained Townsend discharge, **E**: unstable region (corona discharge), **F**: sub-normal glow discharge, **G**: normal glow discharge, **H**: abnormal glow discharge, **I**: unstable region of glow-arc transition, **J-K**: electric arc.

In a glow discharge, the carrier generation process reaches a point where the average electron leaving the cathode allows another electron to leave the cathode. For example, the average electron may cause dozens of ionizing collisions via the Townsend avalanche; the resulting positive ions head toward the cathode, and a fraction of those that cause collisions with the cathode will dislodge an electron by secondary emission. In this way, electrons multiply in the discharge and establish a steady-state current. Typically, the glow discharge is characterized by low currents (10^{-6}-10^{-1} A) and relatively high voltages (hundreds or thousands of volts). Mostly in entire discharge volume (excluding sheath next to the electrodes) ionized gas is electroneutral. In glow discharge plasma is weakly ionized (ionization degree 10^{-8}-10^{-6}) and not equilibrium. Electrons are having average energies of about 1 eV (10^4 K), when temperature of gas and ions is close to normal temperature (300 K). In the glow discharge emission of light is produced by excitation of atoms. Once excited, atoms will lose their energy and one of the various ways that this energy can be lost is radiation, which means that a photon is released to carry the exceed energy away. In optical atomic emission spectroscopy, the wavelength of this photon can be used to determine the identity of the atom and the number of photons is directly proportional to the concentration of that element in the sample [53–55].

With further increase of voltage, current density starts to increase rapidly (abnormal glow discharge, Figure 2.2 region H-I) and if gas pressure is sufficient and resistivity of electric circuit is low enough to carry high current, glow discharge will transit to the arc discharge (Figure 2.2 region I-J). Typically, the arc discharge is characterized by high currents (more than 1 A) and low voltages (tens of volts) and high pressure of the gas comparing to glow discharge. During the arc discharge plasma is concentrated in a narrow channel along the center of the tube and a great amount of radiation is produced. In the case of arc discharge, on the contrary to glow discharge, plasma is equilibrium and highly ionized (typically 100%, but at least 5%). Electrons and heavy species are having similar energies from 1 to 2 eV (from 10000 to 20000 K). Moreover, high electron densities (~ 10^{23} m^{-3}) are typical for arc discharges and plasma is dominated by collisions [20,26,48,56–58]. Comparison of typical electron densities and temperatures for variable types of plasma are presented in Figure 2.3.

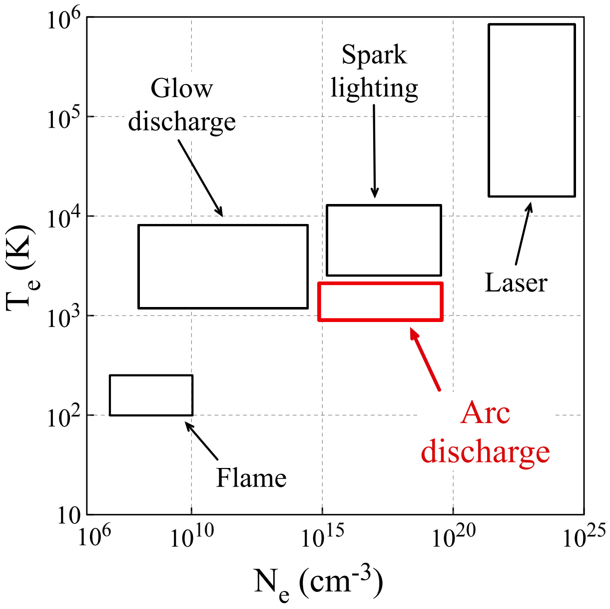

Figure 2.3. Electron temerature and dencity depending on the type of the plasma.

Due to high temperature of gas and high electron density arc discharges and other thermal plasmas could generate high power fluxes and high fluxes of reactive species, which is widely used in manufacturing and other industries. On the other hand, strong radiative emission of the arc is widely used in production of light sources and atomic emission spectroscopy measurements

2.3 Plasma in liquids and in contact with liquid

Recently interest to plasma discharges generated in liquids is rapidly growing owing to the potential applications in various biological, environmental, and medical technologies. For example, electric breakdown is developed as a nonchemical method for biofouling removal and contaminant abatement in water, with a potential for extension into a wide range of other water treatment applications. Plasma methods that effectively combine the contributions of ultraviolet (UV) radiation, active chemicals, and high electric fields can be considered as an alternative to conventional water treatment methods. However, knowledge of the electric breakdown of liquids has not kept pace with this increasing interest, mostly due to the complexity of phenomena related to the plasma breakdown process [37,47,51,59].

Generally, plasmas which are interacting with liquids could be separated into two types: plasmas which come in contact with liquid and plasmas generated directly in liquid.

In the first case of plasmas in contact with liquid, plasma is generated in gaseous medium and interacts with liquid. Due to generation of plasma in the gaseous medium, there is no significant difference between this type of plasma and convenient plasmas generated in gaseous medium. Considering fact, that plasma discharges in gaseous medium were studied extensively for more than 100 years and plasma phenomena and generation process are well known and described in numerous works, recent researches are mostly focused on the plasma-liquid interaction and the effect of plasma on the liquid. Plasmas in contact with liquid are already widely used in water treatment, sterilization and other biomedical applications.

On the other hand, plasmas generated directly in liquids are still not studied completely due to complicated mechanism of generation of the plasma. Historically, plasmas in liquids were studied mostly by electrical engineering community for pulsed power applications and high voltage insulation. Dielectric liquids with high dielectric constant have been widely used as insulating media for high voltage systems, owing to higher dielectric constant of liquids comparing to gases. However, recently there is increasing interest in plasma discharges generated in liquid, which is mostly related to its potential applications for various biological, environmental, and medical technologies. Moreover, plasmas in liquids are already widely used in various applications such as degradation of emerging contaminants in wastewater and drinking water, nanomaterials synthesis, plasma medicine, and even sensing and composition measurements. Another application is use of plasma as an etching tool for the removal of biological tissues. A plasma scalpel in saline solution is able to etch flesh and clean wounds during surgery and is close to widespread practical use. In these applications, it is important to understand the mechanism and dynamics of the electric breakdown process in liquids, for that reason it is important to complete the study of the plasma discharges in liquids, which could be generated various possible conditions [36,37,40,51,59–65].

Electrical discharges in liquid are usually divided into partial and full discharges. In the case of partial discharge, plasma discharge is not reaching second electrode. Partial discharge is also called pulsed corona discharge, and branches of this type of discharge are called streamers (in analogy with the plasma discharges generated in the gas phase). In the partial discharge, the current is transferred by slow ions, producing corona-like discharges (i.e., non-thermal plasma). However, the phenomena of the partial discharges in liquids and the mechanism of streamer formation are much less understood comparing to discharges in the gas phase; moreover, sometimes partial discharges in liquids could be completely different from those for discharges in gases. If a streamer reaches the opposite electrode, it makes a conductive channel between the two electrodes and in this case, discharge is usually called a full discharge. Furthermore, if the current through the full discharge is high (above 1 A), it is called an arc discharge. While arc discharge is usually continuous, the transient phase of the arc discharge is referred to as a pulsed spark discharge. For generation of partial or full electrical discharges in liquid with low conductivity, pulsed high-voltage (from tens kilovolts to megavolts) power supply with a voltage rise time shorter than the Maxwellian relaxation time of the liquid is typically used. High electric field strength can usually be achieved by using needle electrodes with sharp tips, from which electric discharges in water usually start. Owing to history of applications described above, discharges in liquids with low conductivity are studied much better than discharges in highly-conductive liquids. One more reason for that is change in mechanism of the formation of the discharge. In the case of highly conductive liquid usually breakdown could be considered as sequence of a bubble formation process and electronic process within the bubble. The bubble formation process starts from a microbubble formed by the vaporization of liquid from local heating in the strong electric field region at the inter-electrode gap. As the bubble grows, an electrical breakdown subsequently takes place within the bubble. In this case, a cavitation mechanism is taking a key role in the plasma discharge formation [18,28,31,34,36–38,41,42,63,66–69].

Moreover, for a case of a liquid with a high electrical conductivity, a larger discharge current flows, resulting in shortening of the streamer length due to the faster compensation of the space charge electric fields on the head of the streamer. Subsequently, a higher power density (i.e., a higher plasma density) in the channel is obtained, resulting in a higher plasma temperature, higher UV radiation, and the generation of acoustic waves. In the full discharges, such as arc or spark, the current is transferred by electrons. The high current heats a small volume of plasma in the gap between the two electrodes generating a quasithermal plasma with the temperatures of electrons and heavy particles almost equal. There are many experimental conditions which can change mechanism of formation of the discharge and type of plasma. Most important ones are electrical parameters which are usually defined by the electrical circuit and inter-electrode gap length. Order of the inter electrode gap length could also change mechanism of the discharge dramatically and provide new requirements to the electrical circuit. Change of the structure of generated in liquid plasma depending on the inter-electrode gap is presented on Figure 2.4 [18,28,31,33–36,42,44,64,65,67–71].

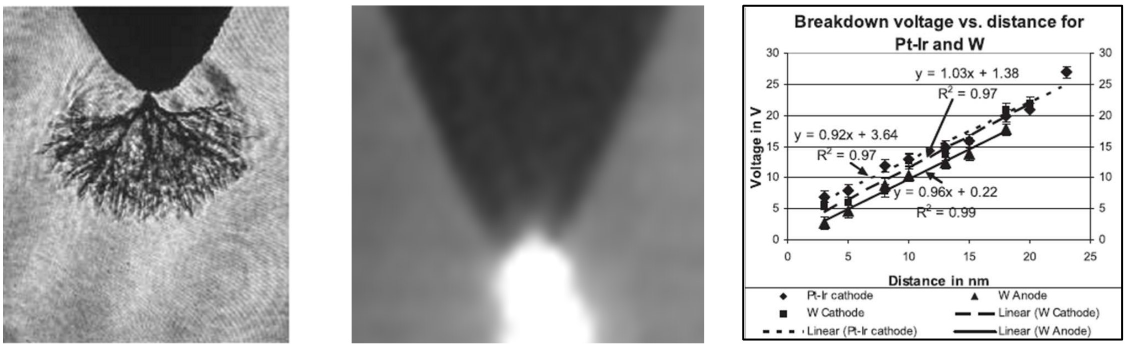

(a) (b) (c)

Figure 2.4. Structure of the plasma in liquid for the inter-electrode gap distance in order of (a) millimeters, (b) microns and (c) nanometers.

It could be observed, that in case of the inter-electrode gap in order of millimeters or greater, mostly bush-like plasma is observed, when in the case of microgaps (several microns or tens of microns) plasma structure is mostly filamentary. Moreover, in the case of gaps of nanometer scale, structure of plasma is still not studied well. Recently, microplasmas are taking growing interest due to possibility of development of compact devices for diagnostics of liquids, nanoparticles formation and modification of the liquid. One of promising applications is use of atomic emission spectroscopy of microplasmas generated in highly conductive sea water for elemental composition analysis and impurities detection. However, microplasmas in highly conductive liquids, such as sea water, are poorly studies (especially in sea water under high pressure). Therefore, more detailed study of microplasma discharges in sea water and deep sea water is required for development of compact analytical tools.

2.4 Composition analysis of sea water

In the case of sea water, complex composition of sea water is a main problem related to elemental composition analysis and impurities detection. Owing to big number of components (including chemically reactive ones) in various concentrations, composition analysis of sea water is typically performed in laboratory conditions on specialized equipment.

2.4.1 Laboratory methods

Inductively coupled plasma mass spectrometry (ICP-MS) is a type of mass spectrometry where the sample is ionized with inductively coupled plasma and then introduced in a mass spectrometer to separate and quantify ions. Schematic of the ICP-MS is presented on the Figure 2.5.

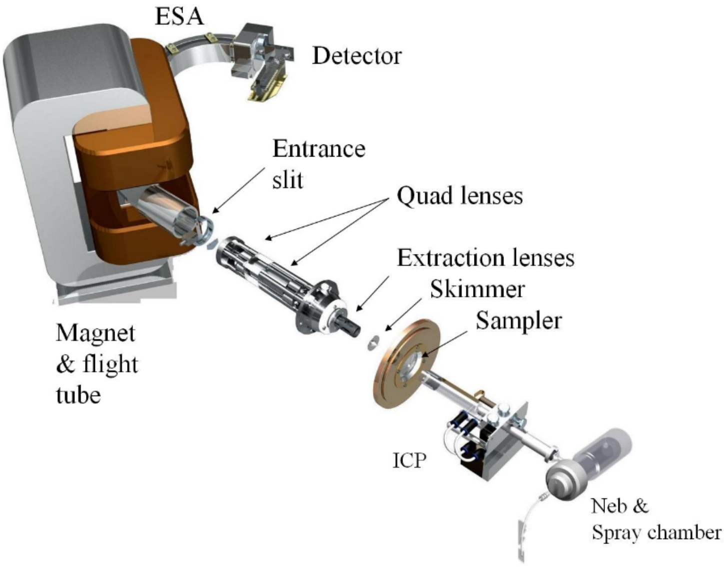

Figure 2.5. Schematic of the ICP-MS device.

Using ICP-MS it is possible to detect metals and several non-metals at in such a low concentration as one part in 10^{15} (part per quadrillion, ppq) on non-interfered low-background isotopes. This is achieved by ionizing the sample with inductively coupled plasma and then using a quadrupole mass spectrometer to separate and quantify those ions. Main advantage of the ICP-NS method is extremely high accuracy; however, analysis could be performed only in laboratory conditions and require sampling. Moreover, depending on the type analyzed material, it could require special preparation of the sample and it is impossible to study some types of solid materials. Despite the high accuracy of the method, requirement of sampling and transport of the samples makes analysis of deep sea water long and complicated using ICP-MS [16,29,49,72,73].

One of other common technics of composition analysis is laser induced breakdown spectroscopy (LIBS). Atomic emission spectroscopy of laser spark at the surface of the sample (or in the gas, depending on type of the sample) is used in this method. Schematic of the LIBS device is presented on Figure 2.6. Laser spark is formed by irradiation of the sample by laser beam. A very hot plasma is formed in a laser spark (up to 40000 K at electron concentrations up to ~ 10^{18} cm^{-3}). In this case, the plasma of the flame extracted from completely different samples often has similar characteristics, which is good for analysis of various samples. Main advantage of the LIBS method, comparing to ICP-MS, is possibility to work with any type of samples without special preparation; however, detection limits of this method are relatively low (order of ppm).

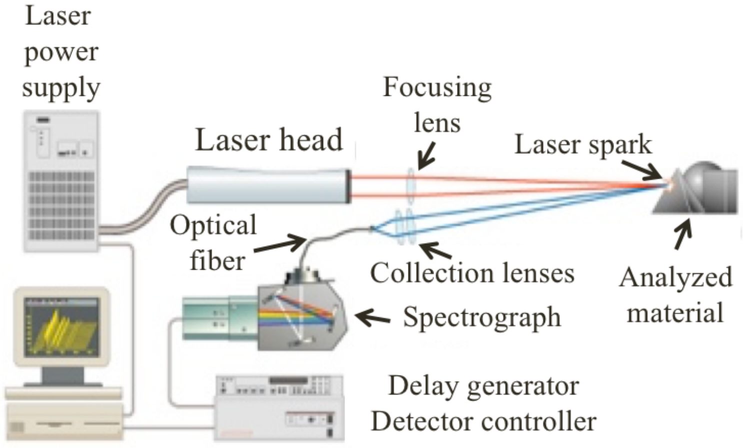

Figure 2.6. Schematic of the LIBS device.

In both cases, ICP-MS and LIBS, and in any other laboratory method there is one major disadvantage for composition analysis of deep sea water – necessity in sampling and transport of the samples. Considering huge amount of water in oceans, analysis of sea water in wide areas using laboratory methods will be complicated, slow and costly. Perfect solution for that problem will be use of atomic emission spectroscopy of plasmas generated in water, which makes possible on-site measurements.

2.4.2 OES of plasma generated in liquid

One of the possible ways to detect impurities in water is the spectral analysis of different types of plasmas generated in the water examined. In this case, if plasma could be generated and analyzed in a liquid, there is no need for sampling and transport of samples, which could hasten measurements and reduce the cost. Comparing to laboratory method, OES of plasmas in liquids has lower resolution and detection limit (tens of ppm); however, this kind of measurements could be performed on-site. Moreover, use of microplasma discharges could be generated using compact setup, which looks promising for development of compact analytical tools. Considering high requirements to composition analysis accuracy in resent biochemical and oceanography research activities, perfect solution will be use of OES of microplasmas in deep-sea water for fast analysis and check of target elements, collection of samples at locations where target element was detected by OES of microplasma, and precise study of small amounts of collected samples in laboratory conditions.

Chapter 3. Methods and experimental

3.1 Experimental conditions and materials

Four types of liquid, namely ultrapure water (UPW, electrical conductivity 55 nS/cm at 25.3°C), naturally sampled deep sea water (DSW, sampled at 374m depth offshore Cape Muroto, Japan, electrical conductivity 44.2 mS/cm at 19.8°C), artificial sea water composed of 10 main components (10ASW, electrical conductivity 45.1 mS/cm at 20.3°C) and reference solutions with ultrapure water each containing a single component from the 10ASW (1 M NaCl, 1 M $MgCl_2$+H_2O, 1 M Na_2SO_4, 1 M $CaCl_2$, 1 M KCl, 1 M $NaHCO_3$, 1 M KBr, 1 M $NaHCO_3$, 1 M H_3BO_3, 1 M $SrCl_2$+H_2O, 0.1 M NaF, 0.1 M HCl, 0.25 M NaOH) were used for the experiments. Elemental composition of the 10ASW is shown in Table 3.1. The main composition of DSW was almost the same as 10ASW; however, natural DSW contained small amounts of additional impurities such as NO_3, Si, P, Mn, Fe, Cu, Pb and Cd.

Table 3.1. Elemental composition of the 10ASW in grams for 1 kg of water.

Ingredient	Mass (g)
NaCl	23.939
$MgCl_2$+$6H_2O$	10.849
Na_2SO_4	3.994
$CaCl_2$	1.123
KCl	0.667
$NaHCO_3$	0.196
KBr	0.098
H_3BO_3	0.027
$SrCl_2$+H_2O	0.004
NaF	0.003

The microplasma discharge was operated using a needle-to-plane, pin-to-pin or rod-to-rod electrode system immersed in liquid to be examined. A probe needle of high electrical conductivity Pd alloy (NPS Inc. P26-10-20 × 1"), a probe needle of high electrical conductivity and thermally stable W (NPS Inc. W20-05-10 × 1 ½"), cut of chemically stable Pt wire (The Nilaco corp. 99.98%, diameter of 200 μm) or cut of stainless steel wire (Nilaco Company SUS304, 0.5 mm in diameter) were used as the needle electrode with the radius of the tip varied in a range 4-200 μm. Elemental composition of Pd alloy needle is presented in Table 3.2. As the plate electrode a polished platinum (Pt) plate 15 mm x 15 mm in square and 0.5 mm in thickness, was used.

Table 3.2. Elemental composition of the Pd alloy in percent.

Ingredient	%
Pd	34.71
Ag	29.89
Cu	14.19
Pt	10.00
Au	9.90
Fe	0.02
Ni	0.01

3.2 Experimental devices

A pulse current source, consisting of a capacitor (C = 47, 100, 220, 440 and 660 nF), inductor (L = 67, 100, 150 and 470 µH) and MOSFET switch was used to supply the discharge. 440 and 660 nF capacitors were obtained by parallel connection of 220 nF capacitors. Serial numbers of components used in the pulse current source are presented in Table 3.3.

Table 3.3. Serial numbers of used electric parts.

Component	Serial number
47 nF capacitor	ECQE12473KF
100 nF capacitor	ECQE12104KF
220 nF capacitor	ECQE12224KF
67 µH inductor	TCV-670-9A-8026
100 µH inductor	TCV-101-9A-8026
150 µH inductor	TCV-151-9A-8026
470 µH inductor	TCV-471-9A-8026
MOSFET	SCT2080KE

The capacitor was charged through a resistor by a regulated DC power supply to resulting voltage in range 100-800 V. The MOSFET switch was closed during the discharge, to apply current pulse to the gap between the electrodes. Circuit generated a single pulse with current and voltage waveforms depended on the parameters of C, L and the resistance

(R) of the liquid between the electrodes. Simplified schematic of the pulse current source is presented on Figure 3.1. The voltage and current waveforms were stored in a digital oscilloscope using a high voltage probe and a current probe (IWATSU-LeCroy AP015).

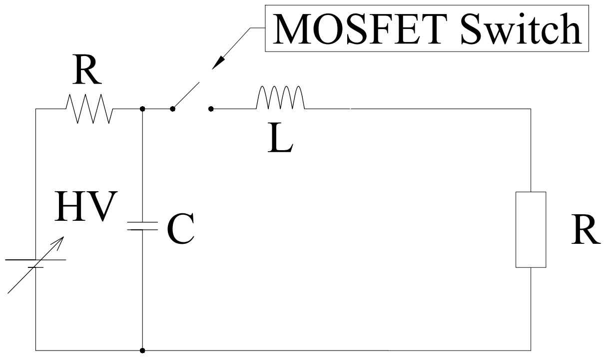

Figure 3.1. Simplified schematic of pulse current source.

The optical emission spectrum from the plasma was collected using quartz UV lens (mid-size collimator 88-181 and focus guide 88-186; Fiberguide Industries Limited) and fed into a multi-channel spectrometer (Ocean Optics USB4000, measurements range 200-850 nm, optical resolution 1.34 nm) through a quartz optical fiber (Ocean Optics P400-1-SR). The sensitivity of spectrometer and optical fiber was calibrated using Deep-UV Deuterium & Tungsten Halogen light source Ocean Optics DH-2000-DUV. Accumulating time of the spectrometer was set at 4 ms.

Optical absorption spectroscopy was operated using a conventional double beam UV–vis spectrometer (Hitachi U-3900) with quartz cuvettes (Hellma Analytics 100-QS).

In order to cover all microplasma discharge process by OES measurements, some triggering delays were introduced to the experiments and synchronized to the exposure time of the spectroscope (Figure 3.2), resulting in accumulation of the optical emission during the entire microplasma discharge.

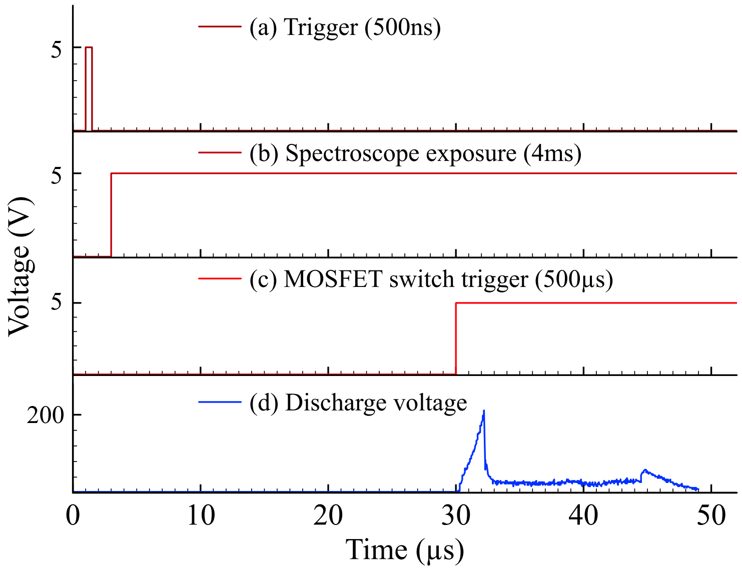

Figure 3.2. Triggering timings: (a) initial trigger produced by pressing the triggering button (500 ns TTL output), (b) trigger for running OES measurements (exposure time was set at 4 ms, measurements started with 4.5 μs delay after the initial trigger), (c) trigger for closing the MOSFET switch and running measurements by oscilloscope (duration 500 μs with delay 25 μs from the start of OES measurements), (d) voltage waveform of the microplasma discharge on the triggering timescale.

Chapter 4. Generation of the micro-arc discharge in highly conductive sea water at atmospheric pressure

4.1 Introduction

Plasmas in dielectric and low-conductivity liquids are studied extensively and are already used in different applications such as water treatment and nanoparticles formation. In the case of highly conductive sea water, direct discharges in liquid are extremely difficult and the main mechanism of discharges is bubble formation due to Joule heating and plasma discharge in a gaseous medium. The bubble formation process in a highly-conductive liquid is complex, due to a high current density and large energy loss related to current heating of the surrounding liquid, which does not participate in the microplasma discharge. In addition, recent research related to plasma formation in the highly-conductive liquids, has been mostly carried out using large breakdown voltages (up to 100 KV) and large gaps between the electrodes (ranging from several millimeters up to ten centimeters, which is considered to be large for microplasma discharge). However, in the case of microplasma generated with micro-gaps (several tens of micrometers) between electrodes, the smaller gap the greater influence of the bubble formation process and the experimental conditions on the plasma generation to such an extent that the reproducibility of the experiments is likely to be adversely affected [18,21,28,46,69,74,75].

There are several approaches to conduct stable process of bubble formation and plasma initiation in highly-conductive liquid. One of the possible ways is use of liquid electrode plasma (LEP) system. Principle of the LEP method is presented on Figure 4.1.

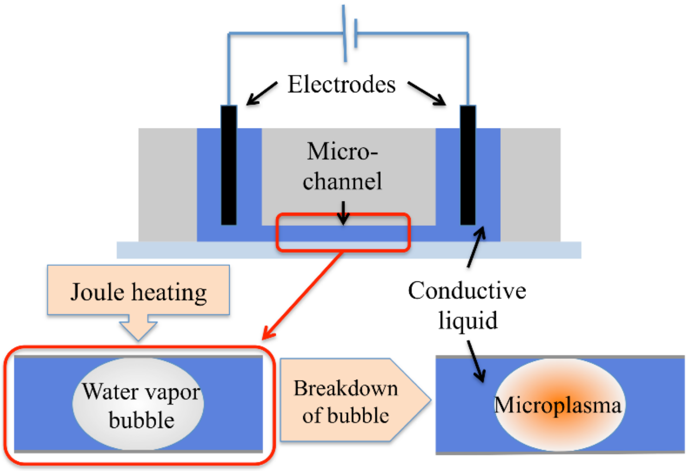

Figure 4.1. Principle of the LEP method.

In the LEP method, a discharge chamber, filled with a highly-conductive liquid, is separated in two parts by a micro-channel and electrodes are introduced to different parts. After applying voltage to the electrodes, LEP configuration allows to concentrate all current in the micro-channel, resulting in a local heating of water and the bubble formation. After formation of the bubble in the micro-channel, the gap will be filled by vapor, size of the gap will be defined by diameter and length of the micro-channel, highly-conductive liquid will play role of electrodes. The LEP method helps to solve problems of heating of the surrounding liquid and allows to operate discharges under low breakdown voltages (less than 1 KV). However, in LEP setup plasma causes damage to the micro-channel, resulting in change of the channel volume and discharge conditions; moreover, adjustment of gap is complicated due to necessity of changing of micro-channel to modify the gap, which limits possible applications of LEP configuration. Promising way to set and keep the discharge gap is use of the needle-to-plane configuration of electrodes with micromanipulator, due to the possibility to set the gap distance before each discharge. In this approach; however, due to contact of the entire surface of the electrodes with highly-conductive liquid, significant current goes through the surrounding liquid resulting in a large energy loss. Consequently, more detailed study of effect of experimental conditions on the discharge, pre-heating and bubble formation phases of microplasma discharge in sea water is required for stable low voltage (less than 1 KV) plasma generation using the needle-to-plane electrode system [13–15,17,18].

4.2 Objectives

In this part of the research, investigation of the micro-arc discharge process in highly-conductive sea water will be presented. To achieve reproducible micro-arc discharges it was important to understand mechanism of the discharge, to investigate the effect of the experimental conditions on the discharge, and to find optimal conditions for the reproducible generation of the discharges. For that purpose, effect of the experimental conditions (value of capacitor and inductor used in the circuit, length of the discharge gap, and voltage of the charged capacitor) were studied and optimal parameters for reproducible discharges were defined. To study the role of bubble formation process in the discharge, various methods of the needle electrode insulation were applied. By use of electrodes with various insulation, for the first time it was confirmed that the micro-arc discharge was generated only after formation of the bubbles, which were covering entire discharge gap. Moreover, to study local effects in the discharge gap, mathematical model of pre-heating phase was developed. Results of the modelling showed, that reproducible micro-arc discharges could be generated even using damaged by erosion needle electrodes. Further, the applicability of the micro-arc discharges to the on-site elemental composition of the sea water is discussed.

4.3 Experimental end methods

For the experiments, two types of sea water were used: 10ASW and DSW. A schematic of the experimental setup is presented in Figure 4.2. For operation of microplasma discharges, the needle-to-plane electrode system was used. The plate electrode was placed on the bottom of a quartz cuvette of inner size of 18 mm x 18 mm in which 1 milliliter of 10ASW was fed, resulting in 2 mm water depth inside the cuvette due to the surface tension effect. The needle electrode was suspended by a micromanipulator, which was used for precise control of the gap length. The gap length of 10-40 μm, measured from the position of electrical contact, was set using a scale on the micromanipulator.

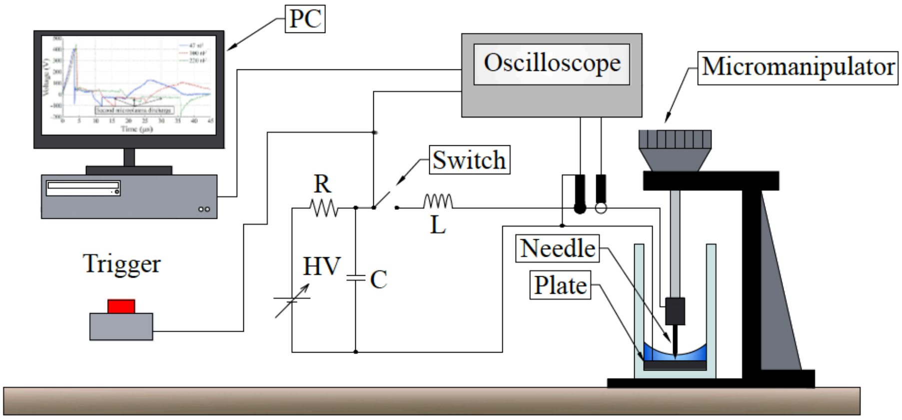

Figure 4.2. Experimental setup.

Due to high electrical conductivity of sea water, it was necessary to supply a large current to obtain a high voltage, required for electrical breakdown with a micro-arc discharge. A pulse current source, consisting of a capacitor C = 16, 47, 100, 220 nF, an inductor L = 47, 100, 150 μH, and a MOSFET switch was used to supply a current pulse. The capacitor was charged by a regulated DC power supply through a resistor to resulting voltage of 500-750 V. During the discharge, the MOSFET switch was closed, in order to apply a current pulse to the gap between the electrodes. The circuit generated a single pulse (over dumping) or several dumping oscillations depending on the C, L, and resistance of sea water between the electrodes. Current and voltage waveforms of the pulse were dependent on the parameters of C, L and the resistance (R) of the 10ASW between the electrodes. The pulse current source was manually operated using a single trigger, the MOSFET switch was kept closed for 100 μs to completely cover all discharge processes. Furthermore, to prevent excessive heating of water in the microgap and keep temperature same before each discharge, sufficient intervals (for more than 30 s) between the discharges were applied. In presented experiments, a positive pulse was applied to the needle electrode, while the plane electrode was electrically grounded. The maximum voltage and current for this setup were 1 kV and 30 A, respectively.

4.4 Typical current & voltage waveforms and effect of circuit elements

Typical current, voltage, and electrical conductivity waveforms with and without microplasma discharge in 10ASW are shown in Figure 4.3. Figure 4.3 (a) shows the typical waveforms of voltage and current when a microplasma discharge was not ignited using 100 μH inductance and a 100 nF capacitor charged to 600V. The voltage and current followed the same waveform of dumping oscillation with the peak voltage of 350V and the peak current of 15A. The waveform was almost in agreement with the simple calculation using a solid resistor instead of sea water, except for a large current region, because of magnetic flux saturation of inductance.

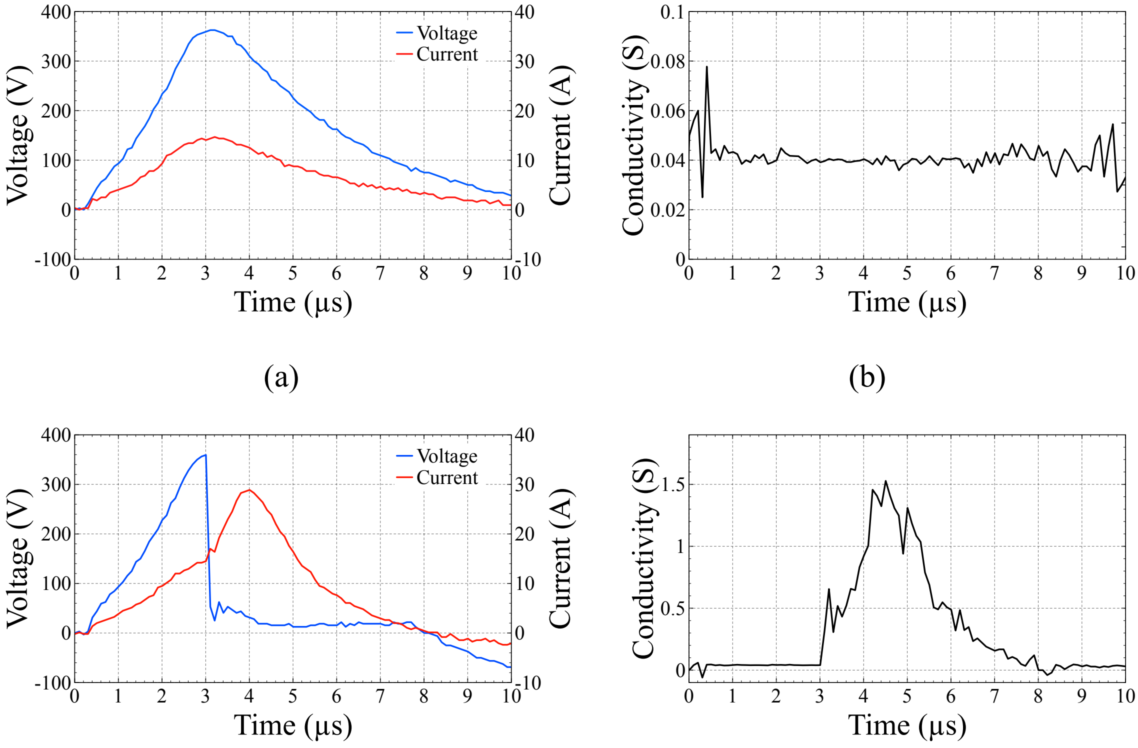

(a) (b)

(c) (d)

Figure 4.3. Typical waveforms for (a) current and voltage, (b) evaluated conductivity without microplasma discharge, (c) current and voltage, and (d) conductivity with microplasma discharge when L = 100 μH and C = 100 nF.

As shown in Figure 4.3 (b), the electrical conductivity of the sea water between the electrodes, which is the ratio of current to voltage, was almost constant at 43 mS (resistance about 23 Ω) even during the discharge without plasma. The evaluated electrical conductance between the electrodes was not only for the small volume beneath the needle, but also including the whole entire medium surrounding the needle.

Using the same circuit, when the charged voltage was increased to 610 V, which is over the critical value, microplasma generation was observed, as shown in Figure 4.4. Before a microplasma discharge, as shown in Figure 4.3 (c), the voltage increased as similarly observed for non-plasma discharge until the maximum of 350 V at 3 μs, when the voltage abruptly decreased due to formation of the microplasma discharge. During the microplasma discharge sustained for 5 μs, the voltage was almost constant at 20 V. Due to the low voltage, the microplasma discharge could be explained by the cathode arc discharge scheme. The current waveform followed the same trend as the voltage until the ignition of micro-arc discharge at 3 μs. After the ignition, however, the current increased further until the peak of 30 A at 4 μs and then decayed until the termination of micro-arc discharge. After the termination of the positive current at 8 μs, the voltage and current turned to negative oscillation due to the inversed charge of the capacitor.

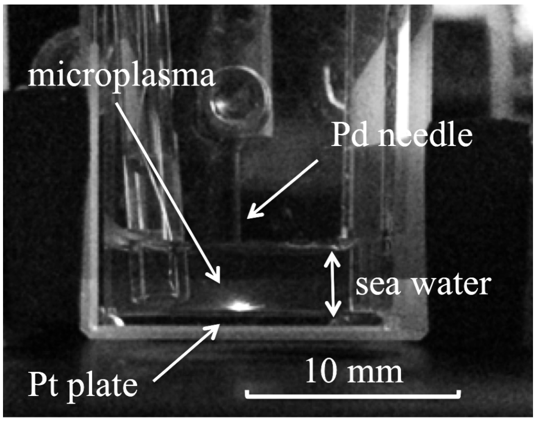

Figure 4.4. Photograph of the micro-arc in sea water.

Figure 4.3 (d) shows electrical the conductivity between the electrodes for the micro-arc discharge. During the micro-arc discharge, the conductance markedly increased due to the termination of electrodes by the plasma. Because of the almost constant voltage with variation of current during the micro-arc discharge, the conductance waveform almost followed to the current waveform. After the termination of micro-arc discharge, the conductance quickly recovered to the original value.

4.4.1 Effect of the capacitor charging voltage and capacitance on I&V waveforms

To control operation of the micro-arc discharge, it was necessary to understand effect of each experimental parameter on the discharge. For that purpose, micro-arc discharges were operated using various voltages when other experimental parameters were kept the same.

Figure 4.5 shows three sets of voltage and current waveforms at different voltages of charged capacitor of 700, 750 and 800 V, when L = 47 μH, C = 100 nF and discharge gap of 20 μm were kept the same. When the charging voltage was increased from 700 to 800 V, the pace of the voltage and current waveforms changes was increased, resulting in faster micro-arc discharge ignition and a peak shift of 0.2 μs. Although the peak current was not strongly affected by the charging voltage, the decay of the current during micro-arc discharge was slightly slow and the total duration of micro-arc discharge was slightly extended. By increasing the charging voltage, due to the increase in the electrostatic energy stored in the capacitor, the micro-arc discharge was sustained for a bit longer duration. However, there was a critical charging voltage required for the ignition of micro-arc discharge. To prevent electrodes erosion, it is better to minimize the charging voltage to stable minimum value, to decrease the total energy of micro-arc discharge.

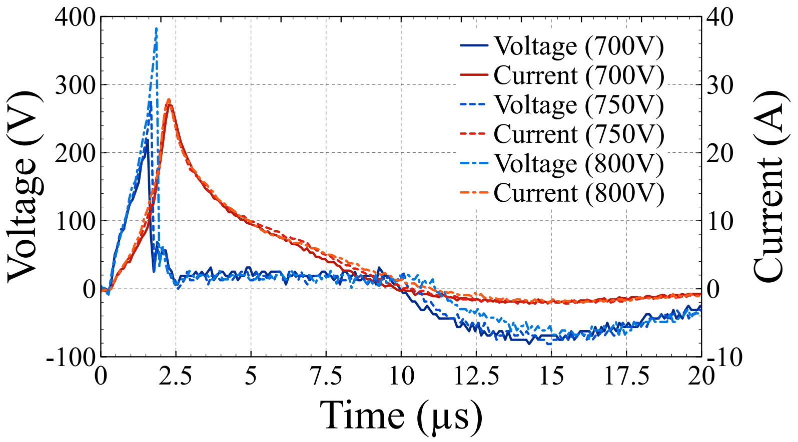

Figure 4.5. Current and voltage waveforms at various charging voltage of the capacitor.

The effect of the capacitor in the impulse generator on micro-arc discharge was examined using a constant inductance L = 47 μH, a constant charging voltage of 650 V and discharge gap of 20 μm. Figure 4.6 shows the effect of capacitance (*C*) on the peak current and duration of micro-arc discharge. By increasing capacitance, the peak current and discharge duration were increased similarly. It was confirmed that the minimum capacitance for reproducible micro-arc discharges under the examined conditions was 15.6 nF. Using the minimum capacitance, we reduced the duration of micro-arc discharge to 4 μs and the peak current to less than 4 A.

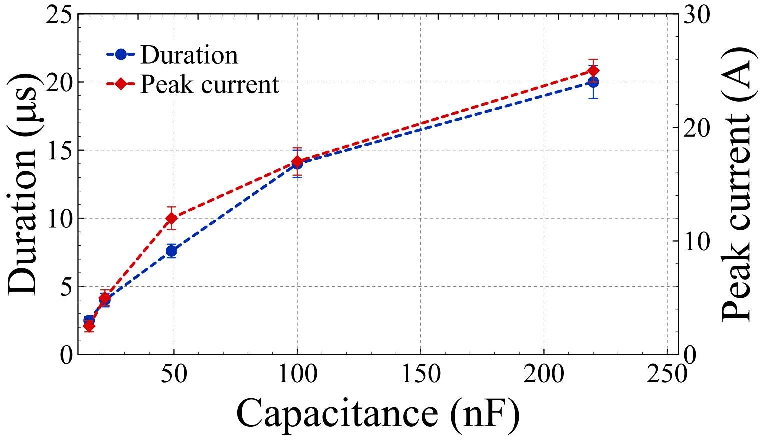

Figure 4.6. Effects of capacitance on the peak current and duration of micro-arc discharge when L = 47 µH and the charging voltage was 650 V.

Below the minimum capacitance, no micro-arc discharge was obtained. By decreasing the capacitance, the total energy stored in the capacitor became insufficient for the ignition of discharge. The results showed that some critical pre-heating energy is required for the ignition of micro-arc discharge. They indicate that the pre-heating energy was used for bubble formation between the electrodes and that mechanism of microplasma formation is bubble breakdown.

4.4.2 Effect of the inductor on I&V waveforms

Using the minimum capacitance in the previous experiment, C = 15.6 nF, and the same charging voltage of 650 V, we examined the effect of inductance (*L)* on micro-arc discharge. Figure 4.7 shows voltage and current waveforms at inductances of 47, 150, and 330 µH. With the increase in the inductance, as expected from circuit calculation, the oscillation frequency decreased. Before the ignition of micro-arc discharge, the voltage and current increased more slowly; consequently, the micro-arc discharge started later, and the discharge duration became longer.

It was observed, as shown in Figure 4.7 (a), that the micro-arc discharge started late after reaching the peaks of voltage and current. The figure clearly shows that the discharge ignition is more dependent on the critical energy for pre-heating and bubbles formation than on the breakdown voltage, because the breakdown voltage is less lower than the peak voltage. After the optimization, using L = 150 µH, C = 15.6 nF, and charging voltage of 650 V, the micro-arc discharge could be ignited at a breakdown voltage of 130 V, a peak current of 4 A, and the duration for 3 µs which prevent the serious erosion of the electrodes.

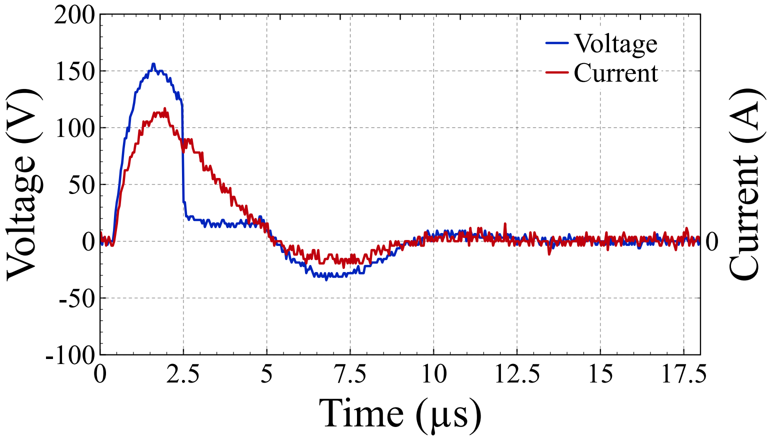

(a)

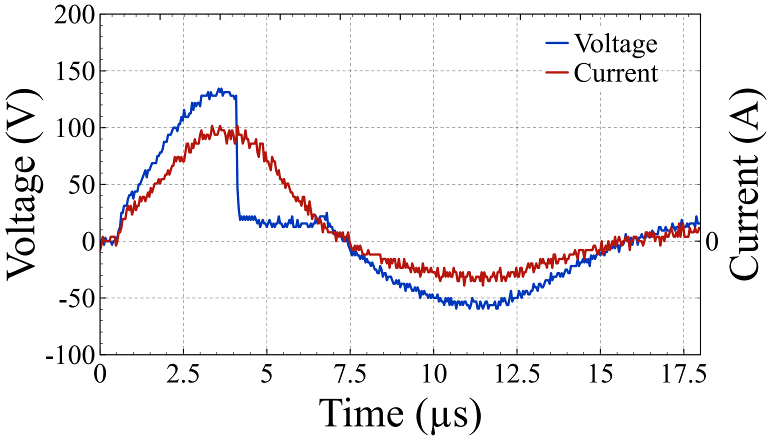

(b)

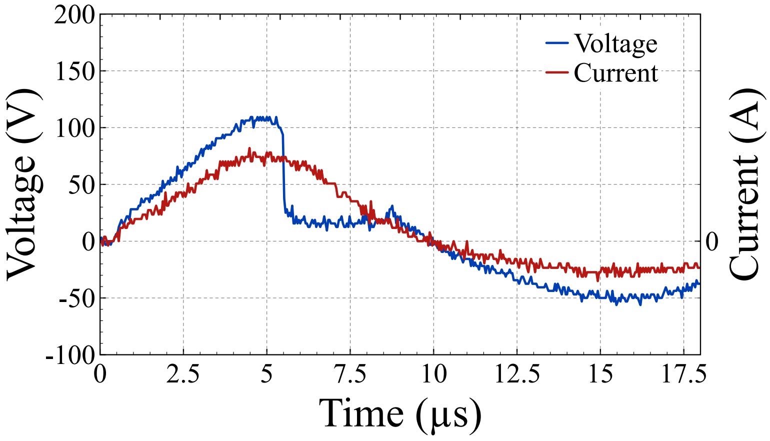

(c)

Figure 4.7. Voltage and current waveforms using the minimum 15.6 nF capacitor and the same charging voltage of 650 V at various inductances of (a) 47, (b) 150, and (c) 330 µH.

From the voltage and current waveforms, it was evaluated, that the joule energy for pre-heating was in the range from 0.8 to 0.9 mJ for all the experiments, while the micro-arc discharge energies were 0.1 mJ for L = 47 μH and 0.2 mJ for L = 150 and 330 μH. In the case of 47 μH inductance, when the micro-arc discharge started, a big portion of capacitor power was already consumed for pre-heating, resulting only in the decaying phase of power was available for the micro-arc discharge. Most of the energy was not used for micro-arc discharge plasma but used for pre-heating. For the operation of plasma for optical emission spectroscopy, it seems better to supply a sufficient energy during the discharge if the electrodes are stable.

4.5 Insulation of the needle electrode

High current causes significant energy loss on heating of water, which surrounds electrodes and does not participate in the plasma formation process. To avoid the current flow through the surrounding water, two types of insulation of the needle electrode were applied, as shown in Figure 4.8.

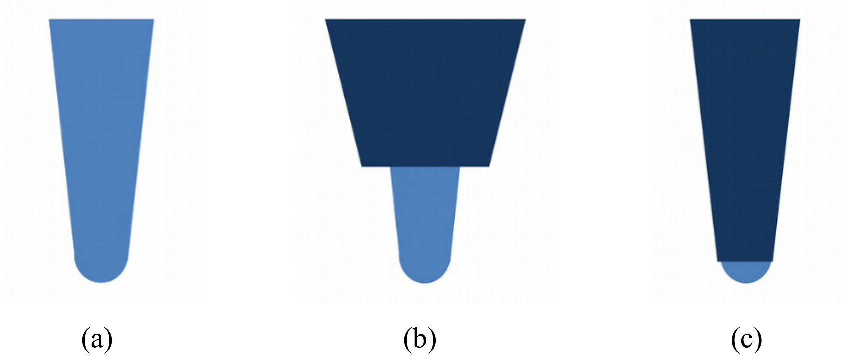

Figure 4.8. Needle electrodes (a) without insulation, (b) with insulation by heat-shrinking tubing, (c) with insulation by PTFE spray.

In the case of the original needle electrode without insulation [Figure 4.8. (a)], the entire surface of the needle immersed in the water (around 2 mm deep) conducts current, resulting in heating of the surrounding liquid by the dispersed current.

By applying heat-shrinking tubing for insulation of the sides of the needle electrode [Figure 4.8 (b)], the length of the open part of the electrode, which contacts with water, could be reduced to 500 μm. However, due to inaccuracy of cutting of the edge of heat-shrinking tubing, it was difficult to control the length of the open part of the needle electrode, which was ranged from 500 to 1000 μm.

Another method is use of polytetrafluoroethylene (PTFE) spray for insulation of sides of the needle electrode, which allows more precise insulation of the needle electrode with only tip (50 μm in radius) open, as shown in Figure 4.8 (c). To control the length of part not coated by insulation, tip of the needle electrode was introduced into a soft material using micromanipulator and PTFE spray was applied to surface of the needle electrode which remained uncovered.

Current, voltage and electrical conductivity dependencies for microplasma discharges generated using needle electrode without insulation were precisely discussed in the Chapter 4.4. For the comparison of dependencies please refer to the Figure 4.3.

Typical current and voltage and electrical conductivity, waveforms with and without microplasma discharge, in 10ASW, using needle electrode insulated by heat-shrinking tubing (length of the open part of the electrode is 700 μm) are shown in Figure 4.9.

Figure 4.9 (a) shows typical waveforms of voltage and current without microplasma discharge using the same circuit with a capacitor charged to 570 V. A significant difference appeared in the voltage waveform comparing to the non-insulated needle case. As shown in Figure 4.9 (c) the electrical conductivity of the 10ASW between the electrodes, as the current/voltage ratio, was relatively constant at 12 mS (R = 83 Ω) for first 2 μs. After that, conductivity started to decrease to 7 mS and kept same value till the end of the pulse.

Based on the observation of the bubble formation process during applying the current pulse (Figure 4.10), it can be assumed that decrease of conductivity is caused by bubbles formed in the discharge gap. However, in the case of using non-insulated needle electrode, there was no noticeable decrease of conductivity during the time of applying the current pulse. It can be explained by reduction of the surface of needle electrode that contacts with liquid by applying insulation, which increases impact of the bubbles on the contact surface, resulting in decreasing of conductance. Using the same circuit and keeping the same water level and position of the needle electrode, when the charging voltage was increased to 580 V (10 V over the critical value), microplasma discharge plasma was observed. Before a microplasma discharge, as shown in Figure 4.9 (b), voltage waveform was approximately same to the no microplasma discharge case, until the peak point of 360 V at 3 μs, where microplasma discharge was initiated and voltage rapidly decreased, due to the high conductivity caused by plasma. During the microplasma discharge, which was sustained for 8 μs, the voltage of 20 V was relatively constant. The current waveform followed the same trend as the voltage, until the ignition of microplasma discharge at 3 μs. After the ignition; however, the current started to increase from 4 A, at the moment of breakdown, to the peak of 7 A at 4.5 μs and decayed until the termination of microplasma discharge. After the termination of the positive current at 11 μs, the voltage and current turned to negative oscillation due to the reversed charging of the capacitor.

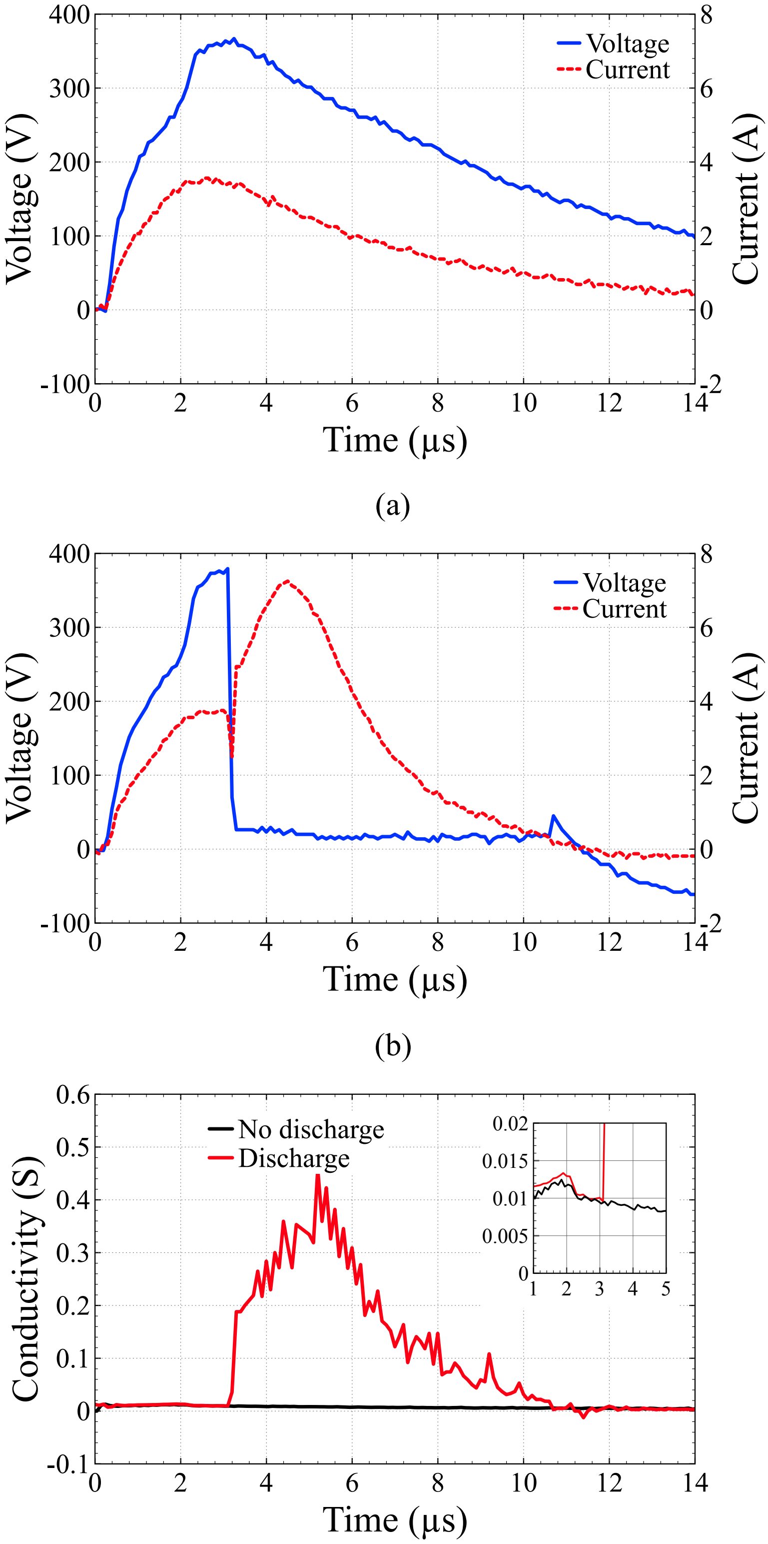

(a)

(b)

(c)

Figure 4.9. Discharge, operated with insulated by heat-shrinking tubing needle electrode, typical waveforms for (a) current and voltage without microplasma discharge, (b) current and voltage with microplasma discharge and (c) evaluated conductivity for both cases.

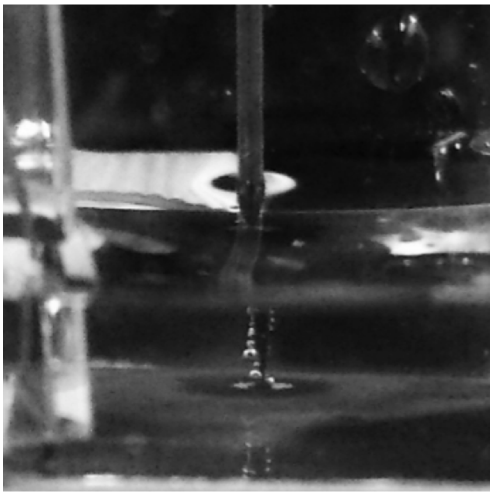

Figure 4.10. Photo of bubbles, formed during applying of the current pulse without microplasma discharge.

Figure 4.9 (c) shows electrical conductivity between the electrodes during the microplasma discharge as the ratio of current and voltage. For first 3 μs, the conductivity followed the same trend as the no discharge case. The same reproducible gradual decrease of conductivity after first 2 μs of pre-heating phase was detected and can be explained by the bubble formation process. It can be concluded that, in the case of microplasma discharge in highly conductive 10ASW, discharge happens after formation of bubbles, due to Joule heating caused by the current. After the bubble is formed, the discharge is initiated in the gas phase. It can be noted that, in this case, the conductivity during microplasma discharge follows the similar trend as in the non-insulated needle case.

To confirm the assumption that microplasma discharge initiates after formation of bubbles, the needle electrode with the PTFE spray insulation was used. In this case, only the tip of the needle electrode participate in the process and the influence on bubble formation should be the most significant.

Typical current, voltage and electrical conductivity, waveforms with and without microplasma discharge, in 10ASW, using needle electrode insulated by the PTFE spray (open part of needle electrode is only the tip with a radius of 50 μm) are shown in Figure 4.11.

Figure 4.11 (a) shows waveforms of voltage and current and Figure 4.11 (c) shows electrical conductivity of the 10ASW between the electrodes, as the current/voltage ratio, without microplasma discharge, using a 100 μH inductance and a 100 nF capacitor charged to a voltage of 650 V (it was necessary to use a bigger values of capacitance and voltage to generate microplasma discharge, due to significant difference in process, comparing to the cases with usage of non-insulated and insulated by heat-shrinking tubing needle electrodes).

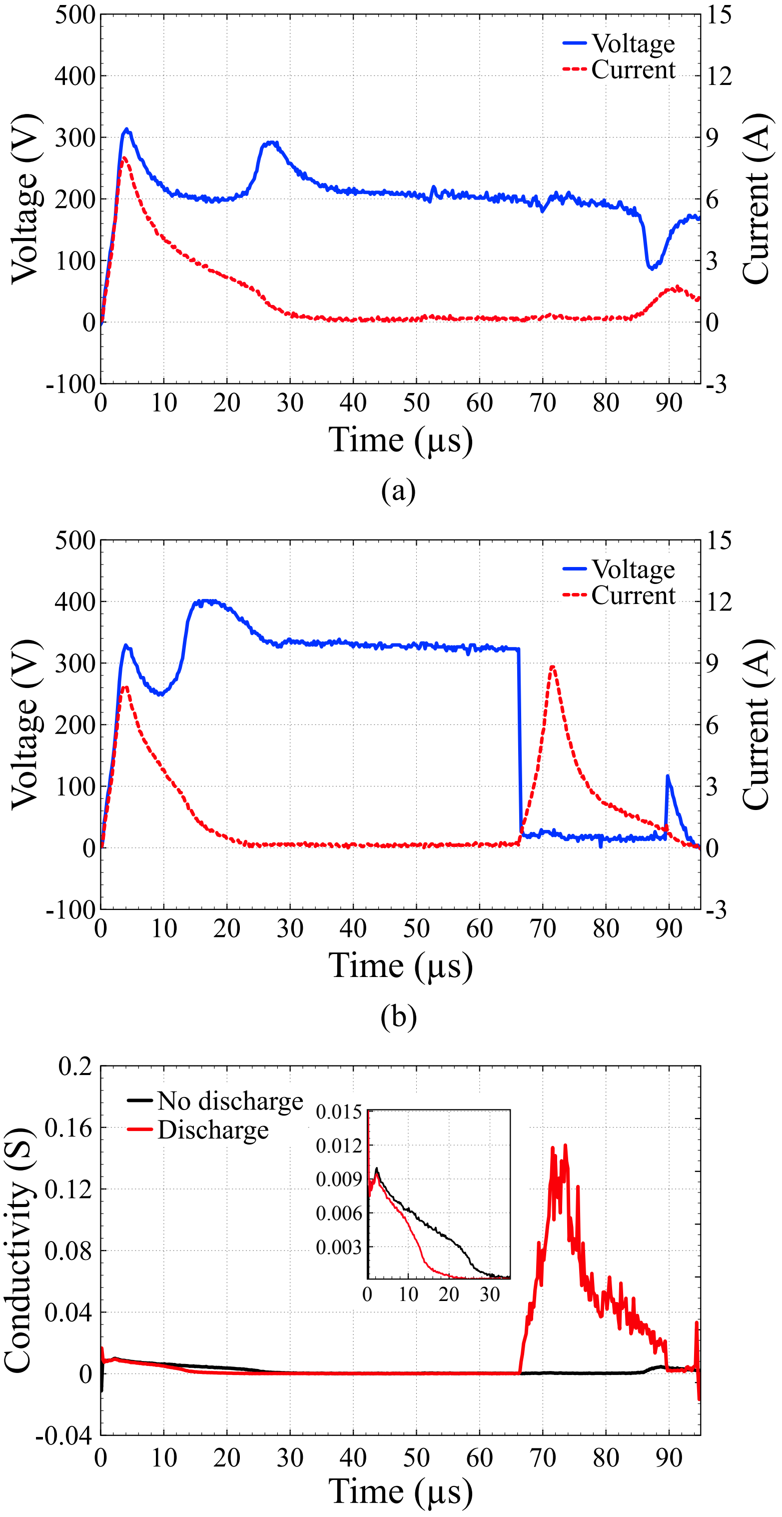

(a)

(b)

(c)

Figure 4.11. Discharge, operated with insulated by the PTFE spray needle electrode, typical waveforms for (a) current and voltage without microplasma discharge, (b) current and voltage with microplasma discharge and (c) evaluated conductivity for both cases.

Figure 4.11 (b) shows waveforms of voltage and current and Figure 4.11 (c) shows electrical conductivity of the 10ASW between the electrodes, as the current/voltage ratio, with microplasma discharge (from 67 to 90 μs), using the same experimental conditions. It can be noted, that in the case of insulation of needle electrode by the PTFE spray, the process becomes not reproducible. Due to the high impact of the bubble formation process and migration of bubbles in the discharge area, electrical parameters of discharge are not stable, resulting in affecting reproducibility of experiments. From conductivity plots [Figure 4.11 (c)] it can be noted that, after pre-heating phase, conductivity drops to value close to 0. This can be explained by filling of all the discharge gap by bubbles, resulting in the insulation of needle electrode tip by the vapor. Due to significant change of the resistance in the circuit induced by bubble formation and migration processes, the shape of current, voltage, and conductivity waveforms may vary in experiments under same conditions.

It took 35 μs and 25 μs for decreasing of conductivity to almost 0 and breaking circuit in the cases for Figure 4.11 (a) and (b) respectively. The difference in time required for bubble formation in the cases for Figure 4.11 (a) and (b) resulted in the different voltages (200 and 330 V respectively) remaining in the capacitor when the circuit was broken by the bubble formation.

In the case of Figure 4.11 (b), the microplasma discharge was accidently ignited at 67 μs, due to initial electrons possibly induced by the cosmic ray, under the voltage sufficient for the conventional gas discharge scheme. On the other hand, in the case of Figure 4.11 (a), the conductivity started to increase unexpectedly at 86 μs and the circuit started to discharge again, because the microgap was partially connected with sea water due to migration of the bubble or decrease in the bubble size, resulting in spending all energy remained in capacitor on Joule heating of water without microplasma discharge.

It can be concluded that, the excess localization of the current was not appropriate for application due to poor reproducibility of discharge. However, by using of PTFE spray coating it was confirmed that in the case of needle-to-plane electrodes configuration, the microplasma discharge in highly-conductive liquid is initiated after bubble formation process. Moreover, it was clarified that the discharge occurs after formation of the bubble of size, sufficient to fill entire discharge gap with vapor.

Insulation by heat-shrinking tubing caused a significant increase of microplasma discharge duration to 8 μs from 4.6 μs for non-insulated needle electrode and a decrease of the charging voltage to 580 V from 610 V.

These results can be explained by reducing the amount of energy, spent on Joule heating of surrounding water, by decreasing the side current flow from the needle electrode. Energy stored in charged capacitor is spent on four processes during applying the current pulse. The first process is pre-heating of water for starting the formation of the bubble, the second process is the bubble formation, the third process is sustaining of plasma discharge and the forth is a loss of energy on current flow through bulk water and additional resistance of the circuit.

For non-insulated needle electrode, energy spent on pre-heating phase (first 2.7 μs before breakdown) calculated from experimental voltage and current measurements was 5.4 mJ. In the case of insulated by heat-shrinking tubing needle electrode, under the same conditions, it was 2.8 mJ, which was almost half of the non-insulated needle electrode case. This excessive energy allowed to increase the duration of microplasma discharge from 4.6 μs to 8 μs and reduced total energy spent on the other processes, which decreased the critical voltage of capacitor charging from 610 V to 580 V.

4.6 Erosion of the electrodes

High current during the discharge causes significant damage of the needle electrode. Moreover, migration of the arc spot during the discharge causes relatively uniform erosion of the electrode material from the tip of the needle. It results in change of shape of the tip from hemispherical (with radius dependent on the used needle) to relatively flat (with area dependent of needle angle and length of remained needle). Possible shapes for needle with 50 μm radius of the tip are presented in Figure 4.12 (a). Figure 4.12 (b) shows typical current and voltage waveforms for the microplasma discharge in 10ASW, operated using original (not damaged by erosion) and damaged needle electrode, 47 nF capacitor charged to resulting voltage of 650 V, 67 μH inductance and gap between the electrodes of 20 μm.

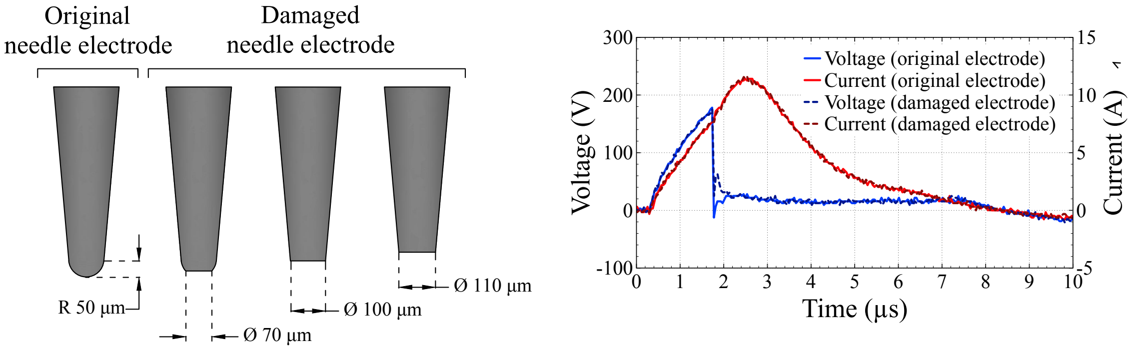

(a) (b)

Figure 4.12. (a) Original needle electrode geometry and damaged needle electrodes geometries with 70 μm, 100 μm and 110 μm in diameter flat surface of the tip and (b) typical current and voltage waveforms for micro-arc discharge in sea water.

In both cases, discharge process can be separated on three phases: (1) pre-heating phase, (2) microplasma discharge, and (3) negative oscillation due to reversed charge on the capacitor. During the pre-heating phase, the voltage and current followed the same waveform of a dumping oscillation with the peak voltage of 190 V and peak current of 8 A. During the microplasma discharge, sustained for 5.2 µs, the voltage was almost constant at 20 V and the current increased further until the peak value of 12 A at 2.2 µs to turn for the decay until the termination of the plasma. After the termination of the positive current at 7.2 µs, the voltage and current turned to negative oscillation due to inversed charge of the capacitor.

In previous work it was confirmed that, bubble formation process plays a key role in the generation of micro-arc discharge in sea water, and variation in electrodes tip shape should have effect on the discharge generation [17,18]. However, from the experiments [Figure 4.12 (b)] it could be observed that there was no significant difference in the current and voltage waveforms of micro-arc discharges generated using original and damaged needle electrode. Considering possible application of the OES spectrometry of microplasma arc discharges in sea water for elemental composition analysis, it was necessary to check effect of the needle electrodes tip shape on measured optical emission spectra.

Optical emission spectra for five consistent microplasma discharges operated in 10ASW using W needle electrode are presented on Figure 4.13.

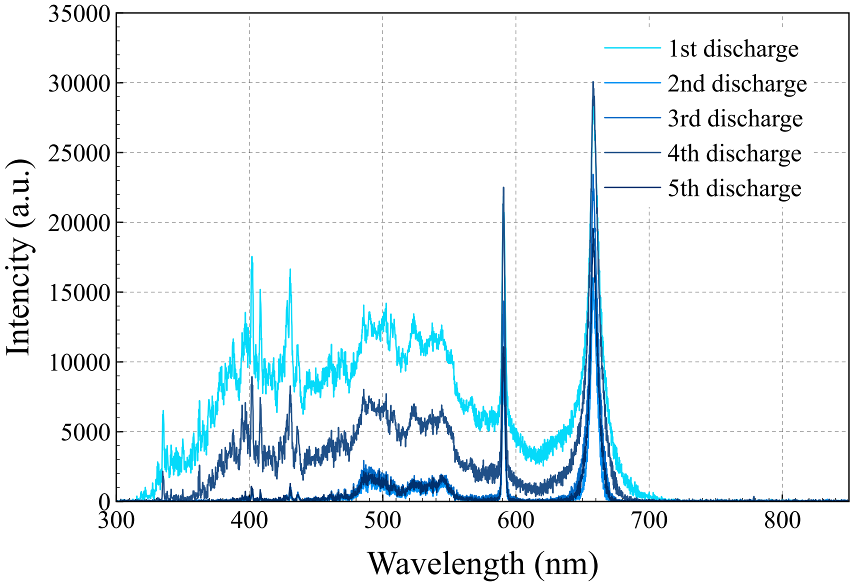

Figure 4.13. Instability of the measured optical emission spectra.

The first discharge was generated using original needle electrode, when following discharges were generated using needle electrode with modified shape of the tip owing to erosion caused by the high discharge current. It can be observed, that intensity of measured optical emission for the discharge operated using not damaged needle electrode was much stronger comparing to the following discharges. Moreover, during the experiments it was confirmed, that discharges operated using not original needle electrode produced reproducible strong intensity of optical emission (some variations were observed due to the focusing accuracy and small variation of the discharge duration), when in the case of damaged needle electrodes, intensity of the measured optical emission was varied in a wide range.

Considering the same experimental conditions (except the shape of needle electrode tip) and current and voltage waveforms, observed instability of intensity of the measured OES spectra can be caused by damage of the needle electrode or inaccuracy of focusing system. To confirm effect of the focusing system on the measured spectra experiments were performed with variable orientation of the lens. Lens was mounted on precise 3d micromanipulator, and to focus lens on the discharge gap, light source was connected by optical fiber to the lens and focusing was performed using micromanipulator and observation of light focused by the lens. In that approach lens was tilt with angle up to 10º to the surface of the plate electrode, as it showed on Figure 4.14 (a).

Due to observation of the discharge gap with some angle to the plate electrode, part of the gap was covered by the needle electrode, and emission from the covered part was not collected by the lens. Moreover, due to the migration of the arc spot during the discharge, optical emission spectra collected by the system depended on position of the arc. In the case of original needle electrode, owing to hemispherical shape of the needle tip, depending on angle of measurement there was a smaller area covered by the needle, resulting in collecting emission from bigger area of the gap and stronger intensity of the measured spectra. Usage of not damaged needle electrodes for measurements can solve problem with instability of measured intensity; however, it makes OES of microplasma discharges not applicable for on-site measurements, owing to necessity in change of the needle before each discharge.

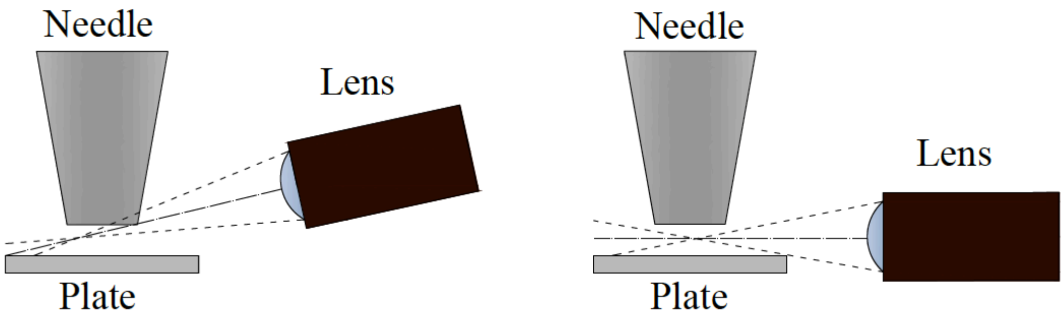

(a) (b)

Figure 4.14. Mounting of lens during measurements (a) with an angle and (b) parallel to the plate electrode.

That problem can be partially solved by mounting lens parallel to the plate electrode during the focusing as presented on Figure 4.14 (b). In that case, it was possible to reduce covered by electrodes part of the gap and perform more reproducible measurements. Optical emission spectra measured using lens mounted parallel to the pate electrode are presented on Figure 4.15.

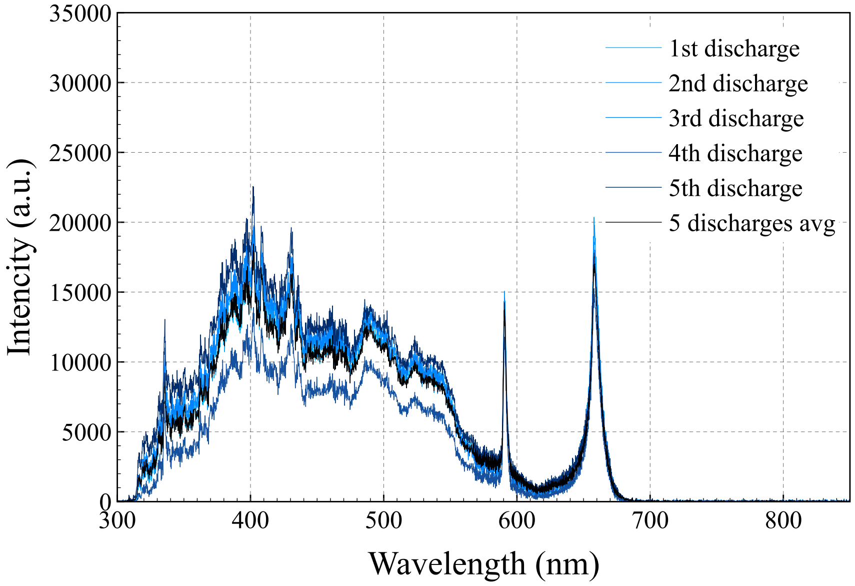

Figure 4.15. Optical emission spectra measured using lens mounted parallel to the plate electrode.

It can be noted, that in this case intensity of the measured optical emission and observed peaks were much more reproducible, than in case with tilted lens. Moreover, there was no significant difference between measured spectra of first discharge, operated using the original needle electrode, and following discharges operated using damaged needle. Reproducible spectra enabled averaging of measured optical spectra from several microplasma discharges. Example of the spectrum obtained by averaging of five spectra of microplasma discharges is presented on Figure 4.15, curve “5 discharges avg”. Averaging of the optical emission measurements allowed to reduce signal-to-noise ratio and to obtain spectra of higher quality, which can be essential for elemental composition analysis due to simplification of assigning of emission peaks. However, due to some instability in the micro-arc discharge duration, there were still some small variations in measured spectra intensity (intensity of the 4th discharge is smaller, comparing to other discharges presented on Figure 4.15).

4.7 Mathematical modelling

To analyze the effect of shape of the needle electrodes tip on the pre-heating phase and to confirm results observed in the experiments, mathematical model was developed, and simulations were performed for variable shapes of the tip. For mathematical modelling of the pre-heating phase two geometries of the needle electrode tip were used: original hemispheric and damaged with 100 µm in diameter flat surface of the tip [Figure 4.12 (a)].

4.7.1 Mathematical model

Model was solved into two blocks:

- RLC oscillation model with defined increment in time, which allowed to simulate current and voltage waveforms generated by the pulse current source

- Local process in the discharge gap and surrounding sea water, which allowed to observe changes of parameters of the sea water in the discharge area and gave insight of the pre-heating phase.

In the first block for calculation of current and voltage waveforms general equation system for RLC oscillator with defined steps in time was used. Switching time of the MOSFET was assumed 0 s.

Current through the circuit for every step in time was estimated using Equation 4.1:

$$\mathrm{I_i = I_{i-1} + V_{L(i-1)} \Delta\tau / L} \tag{4.1}$$

Where $\mathrm{I_{i-1}}$ and $\mathrm{V_{L(i-1)}}$ were current and voltage applied to inductor in previous time step, $\Delta\tau$ was time increment. Voltage on inductor was calculated by subtraction of the voltage applied to the electrodes from the voltage remained in the capacitor. Voltage applied to the electrodes for every step in time was calculated using Ohm's Law:

$$\mathrm{V_{Ri} = I_i R_i} \tag{4.2}$$

Where $\mathrm{R_i}$ was sum of resistance of the circuit and resistance of water between the electrodes. Resistance of the circuit was estimated from fitting of the experimental data and resistance of water between the electrode was determined from the model of local process in the discharge gap as sum of values for each mesh point.

In the second calculation block for pre-heating phase, calculation of the electric field distribution in the discharge gap was performed using the value of voltage applied to the electrodes calculated in the previous time step of the RLC oscillation. Examples of calculated electric field distributions for original and damaged needle electrodes are presented on Figure 4.16 (a) and (b) respectively.

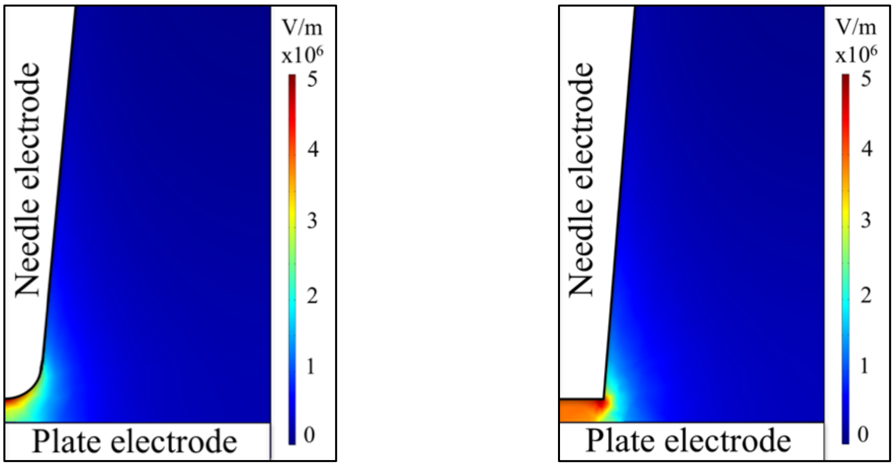

(a) (b)

Figure 4.16. Electric field distribution for the (a) original and (b) damaged needle electrode cases.

It can be noted, that change of shape of the needle electrode tip caused significant difference in electric field distribution in the discharge gap; however, electric field in the surrounding liquid can be considered the same.

Current density distribution in the gap was calculated using conductivity values for every mesh element from the previous step in time and calculated electric field profile. Amount of energy delivered to the liquid by joule heating in every point of the mesh was evaluated using current density distribution in the gap and resistivity of each mesh element:

$$dQ = I^2 R dt \tag{4.3}$$

Temperature profile was calculated using estimated from Equation 4.3 amount of energy delivered to each mesh point and temperature distribution in previous step in time, considering heat transfer in the liquid:

$$c_v \frac{\partial T(\vec{x}, t)}{\partial t} = \nabla(\chi \nabla T(\vec{x}, t)) + q_v(\vec{x}, t) \tag{4.4}$$

Examples of the temperature profiles calculated using Equation 4.4 for original and damaged needle electrodes are presented on Figure 4.17 (a) and (b) respectively.

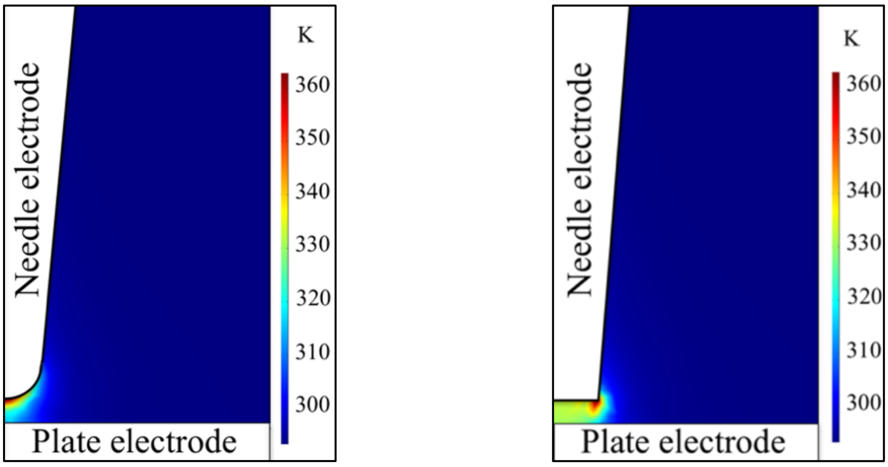

(a) (b)

Figure 4.17. Temperature profile of sea water for the (a) original and (b) damaged needle electrode cases.

Effect of shape of the needle electrode tip on the temperature profile is similar to effect on the electric field distribution and difference between damaged and not damaged needle electrode can be observed mostly in the discharge gap. Insignificant difference in the electric field and temperature profile was observed due to thermal transfer in the sea water and electrodes. Conductivity of liquid for each mesh point was estimated using temperature profile and interpolation of tabulated values of conductivity of sea water for different temperature. After estimation of conductivity of water for each element of the mesh, total resistance of water between the electrodes was estimated and used in the calculation of the next step in time of the RLC oscillation block. Similar temperature profile of the surrounding liquid resulted in almost same values of the total resistance of water between the electrodes. Moreover, there was no significant effect of the needle electrodes tip shape on the bubble formation process.

4.7.2 Results of mathematical modelling

Calculated in mathematical model and measured from experiments current and voltage waveforms during pre-heating phase for original and damaged needle electrode are presented in Figure 4.18.

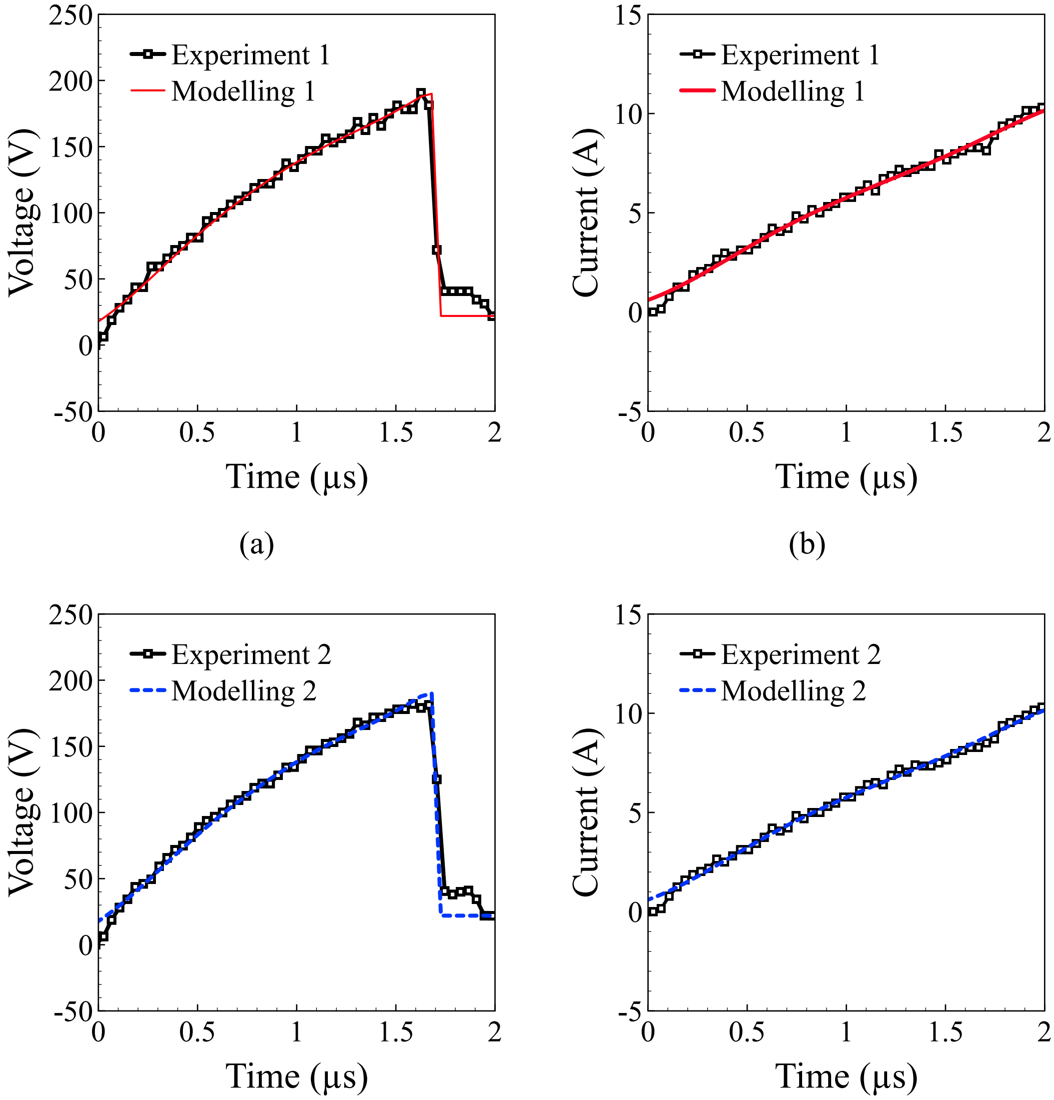

(a) (b) (c) (d)

Figure 4.18. Experimental data and results of mathematical modelling of pre-heating phase for (a) voltage applied to the electrodes and (b) current using original needle electrode, (c) voltage applied to the electrodes and (d) current using damaged needle electrode.

Very good agreement of current and voltage waveforms for pre-heating phase obtained from mathematical modelling and experimental data can be observed in both cases with use of original [Figure 4.18 (a) and (b)] and damaged [Figure 4.18 (c) and (d)] needle electrodes. Moreover, it can be observed, that there was no significant difference in the current and voltage waveforms during the pre-heating phase for original and damaged needle electrode. Similar results were observed in the experiments [Figure 4.12 (b)], where was no significant effect of the tip shape on current and voltage waveforms. That effect can be explained by high conductivity of sea water. Due to high conductivity, significant current goes through surrounding water which does not participate in the plasma generation process. Effects of the needle electrode's tip geometry on the local processes in the discharge gap, observed in the modelling results, were compensated by the current in the surrounding liquid. Considering good correlation of experimental data and modelling results it can be concluded, that shape of tip of the needle electrode effects only on local process in the discharge gap, which has no significant influence on the pre-eating phase.

It can be concluded, that for operation of micro-arc discharges in highly conductive liquids there was no strong effect of shape of tip of the needle electrode on pre-heating phase. That phenomena allows to use damaged needle electrodes for operating of discharges, which can be essential for conducting on-site measurements due to possibility of carrying out measurements without replacement of the electrodes. However, usage of damaged needle electrodes introduces more strict requirements to the focusing system in order to collect optical emission spectra from entire discharge.

4.8 Conclusions

Micro-arc discharge was successfully generated in highly conductive sea water at high pressure by applying pulse currents to the needle-to-plane electrodes placed with microgap. Custom pulse current source with tunable electric parameters was developed to supply the discharge. The microplasma was sustained by the cathode arc mechanism and the breakdown was induced not by any critical voltage but by sufficient pre-heating energy delivered during discharge. After optimization, the micro-arc plasma was ignited at 130 V, the minimum energy for pre-heating of sea water was 0.8 mJ and the minimum energy for the micro-arc plasma was 0.1 mJ.

Two types of insulation of needle electrode were used to study role of the bubble formation process. The complete insulation of the side wall of needle electrode was successfully achieved by the PTFE spray coating. By using needle electrodes insulated by PTFE spray, it was confirmed, that microplasma was initiated after bubble formation. Moreover, it was clarified that the discharge occurs after filling of entire discharge gap with vapor by bubble. Usage of the heat-shrinking tubing insulation allowed the reduction of current flow through the surrounding water, which reduced energy consumption on pre-heating phase and allowed to obtain breakdown using capacitor charged to smaller voltages and finally increased the duration of microplasma discharge.

Mathematical model of pre-heating phase was developed for investigation of the effect of shape of the needle electrodes tip on micro-arc generation process. Mathematical modelling results showed good agreement with experimental data. Results of the simulation confirmed that the shape of tip of needle electrode effected only on local process in the discharge gap and had no effect on current and voltage waveforms during the pre-heating phase. It was confirmed, that there was no effect of the needle electrode’s tip shape on optical emission and electrodes could be successfully reused for the measurements. However, usage of damaged needle electrodes introduced strict requirements to the focusing system.

Chapter 5. Optical emission spectrometry

5.1 Introduction

There have been many studies dedicated to the exploration and use of marine resources; however, owing to numerous possible applications and huge amount of water presented in various conditions (temperature, pressure, elemental composition), the precise analysis of sea water is complicated. The complex composition of sea water causes problems in the identification and separation of the constituent elements (sometimes at low concentrations), which makes composition analysis complicated. There are many methods for determining of the composition of sea water, such as the inductively coupled plasma (ICP) mass spectroscopy of sprayed liquid and optical absorption spectroscopy of the examined liquid. However, most of these methods are performed in laboratories at specialized locations and require large equipment (depending on the accuracy of measurements, the sizes of laboratory devices can vary from a table top to a room), the sampling of water, sample transport, and sometimes special preparation of samples before measurements. The necessity of sampling, long time of analysis, usage of complex equipment, and high power consumption make the elemental composition analysis of deep sea water using the above-mentioned methods long, complicated and as result costly. The most promising way to solve the problems stated above is the development of compact diagnostic tools which can provide rapid on-site analysis of elemental composition of deep sea water and contaminant detection. However, the on-site identification of elemental composition of natural deep sea water is challenging [4,9,10,12,14,15,49,72,73].

One of the promising methods to identify elemental composition of water is a spectral analysis of different types of plasmas generated in examined liquid. There are many ways to generate microplasmas in highly conductive liquids, such as an electrolyte cathode and liquid electrode plasma (LEP), which allow the generation of discharges under low voltages (less than 1 kV). Moreover, prototypes of on-chip devices for composition analysis and impurity detection have already been developed. However, in the case of LEP on-chip devices, a microchannel system is commonly used for the generation of microplasma. The use of a microchannel introduces new limitations related to the initiation of discharges in liquids with a different electrical conductivity and pressure, in addition to problems with the adjustment of the discharge gap. The above-mentioned problems could be solved using an electrode system with a precisely controlled microgap. A promising approach for the development of a compact tool for on-site measurements is the use of a needle-to-plane or needle-to-needle electrode system with a precise micromanipulator owing to the possibility of adjustment of the discharge gap before each discharge. Recent research shows that, use of microgaps enables reproducible ignition of plasma discharges by applying low voltages to the electrodes, even in the case of conductive liquids. Generation of microplasmas using low voltages could be potentially used in development of compact diagnostic tool for on-site measurements in sea water and elemental composition analysis. To this end, the atomic emission spectroscopy of short (1-100 μs) microplasma discharges is promising because of its low energy consumption and simple discharge setup. Moreover, the use of micro-arc discharges is promising for the on-site analysis of deep sea water (2 km and more depth) due to the increase of intensity of optical emission of the arc discharges with the increase of pressure [15,17–19,25,33,53].

5.2 Objective

In this part of the research, investigation of the optical emission spectra of micro-arc discharges generated in highly-conductive sea water will be reported and applicability of the atomic emission spectroscopy of micro-arc discharges to elemental composition analysis of sweater will be presented. For that purpose, effect of the experimental conditions (examined liquid, materials of the electrodes and electrical parameters of the discharge) on the measured optical emission spectra were studied; moreover, reproducibility of measured spectra was confirmed and averaging of multiply measurements was performed. Use of reference solutions spectra was proposed for elemental composition analysis of sea water by atomic emission spectrometry. Using reference solutions method, emission peaks for main components of sea water and metal contaminants from the electrodes were clearly assigned in the spectra. Moreover, by proposed method Fe contaminants in sea water were successfully detected, and for present setup detection limit was 300 ppm.

5.3 Experimental and methods

In this chapter for generation of discharges were used 10ASW, DSW, reference solutions and ultrapure water. As shown in Figure 5.1, the microplasma discharge was generated using a needle-to-plane electrode system placed in a quartz cuvette with inner dimensions of 18 mm × 18 mm, in which 1 mL of liquid was introduced, resulting in a water depth of 2 mm inside the cuvette owing to the surface tension effect.

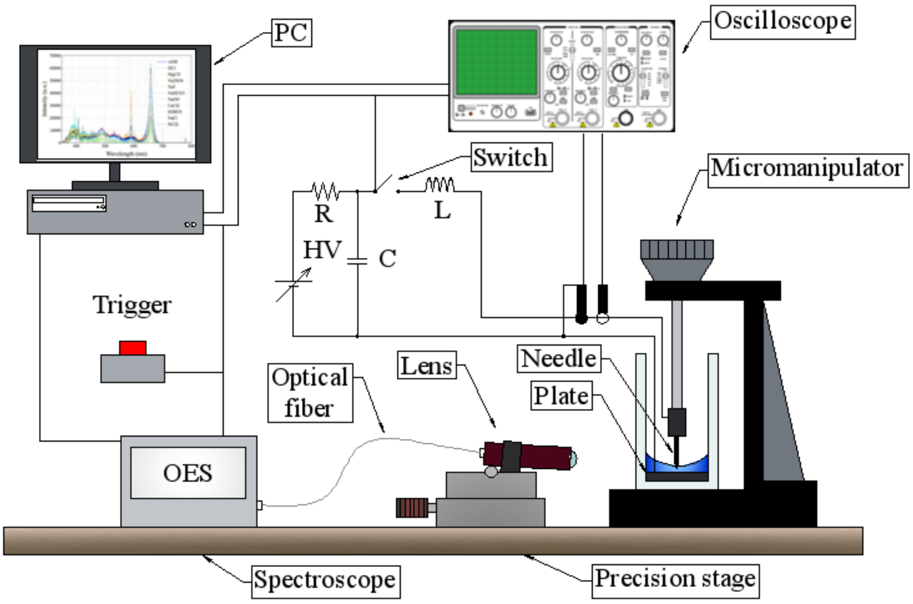

Figure 5.1. Experimental setup.

The Pd alloy probe, W probe and Pt wire cut were used as a needle electrode. The needle electrode was suspended by a micro manipulator, which was used for precise control of the gap length. The gap length of 20-200 μm, measured from the position of electrical contact, was set using a scale on the micromanipulator. As the plate electrode, a polished platinum (Pt) plate having an area of 15 mm × 15 mm and thickness of 0.5 mm was used.

A pulse current source, consisting of a capacitor ($C = 220, 440$ nF), inductor ($L = 67, 100, 150$ μH) and MOSFET switch was used to supply the discharge. The capacitor was charged through a resistor by a regulated DC power supply to resulting voltage of 650-800 V. To reduce erosion of the needle electrode in the cases of Pd alloy and Pt needles, a positive pulse was applied to the needle electrode (anode) whereas the plane electrode (cathode) was electrically grounded. On the other hand, higher melting temperature of W allowed to operate discharge with W needle electrode as cathode by applying negative pulse to it.

To confirm that the optical absorption of the examined liquid does not affect optical emission measurements, optical absorption spectroscopy was performed for each liquid used in the experiments. For all the liquids, optical transmission was close to 100% at wavelengths greater than 300 nm, and transmission rate change was observed in the deep ultraviolet range at wavelengths less than 300 nm (Figure 5.2). Wavelengths greater than 300 nm, which were not affected by absorption, was used in optical emission spectra for the analysis. In this region, the transmission of the optical fibre can be considered constant (Figure 5.2), and it was assumed that the optical fibre had no influence on the measured spectra.

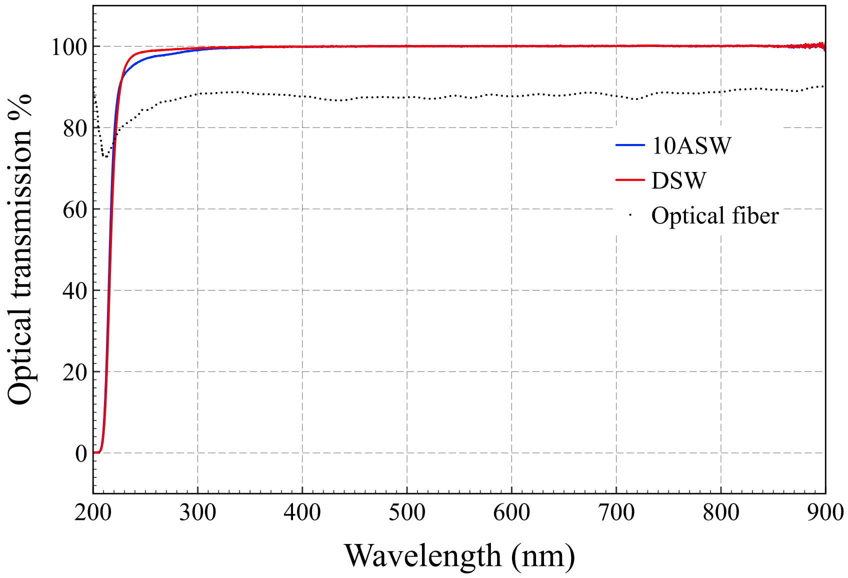

Figure 5.2. Optical transmission spectra for the 10ASW, DSW and optical fiber.

In order to cover all microplasma discharge process by OES measurements, triggering delays were introduced to the experiments and synchronized to the exposure time of the spectroscope, as it was showed in the chapter 3, resulting in accumulation of the optical emission during the entire microplasma discharge.

5.4 Optical emission spectra Pd alloy needle

Typical current and voltage waveforms for microplasma discharges generated in the 10ASW and DSW by using a Pd alloy needle electrode as the anode, a 67-μH inductor, and a 220-nF capacitor charged to a resulting voltage of 650 V are presented in Figure 5.3. The same discharge conditions and similar values of conductivity of 10ASW and DSW resulted in the same current and voltage waveforms of microplasma discharges in both cases. The discharge process can be divided into three phases: (1) pre-heating phase, (2) microplasma discharge, and (3) subsequent oscillation owing to the reversed charge on the capacitor.

In the pre-heating phase, water in the discharge gap and surrounding the electrodes was heated by high electric current, resulting in a rapid boiling and formation of the bubbles. Recent research confirmed that microplasma discharge initiates after the formation of bubbles that cover the entire discharge gap [17]. Fluctuations in the bubble formation process and migration of the bubbles results in a variation of duration of the pre-heating phase in the range of 2.5-3.1 μs for 10ASW and 2.5-3.2 μs for DSW. This variation can be explained by the different amounts of energy spent on the pre-heating phase, which are 5.51-5.92 mJ for 10ASW and 5.49-5.95 mJ for DSW (the energy was evaluated from the current and voltage waveforms). After the pre-heating phase, the entire discharge gap was filled by vapor and microplasma discharge initiated in the gaseous medium. After breakdown, owing to the termination of the electrodes by plasma, the voltage rapidly decreased to 20 V and was relatively constant during the entire microplasma discharge phase. On the other hand, after the formation of the plasma, the conductivity of the plasma channel was higher than that of the water, resulting in the increase of the current to a peak point of 24.5 A with subsequent decay until the termination of microplasma discharge. Considering a low voltage, a relatively high current during the discharge, and low melting temperatures of both electrodes (approximately 1300 K for Pd alloy and 2041 K for Pt, which are less than the temperature required for the arc discharge with a hot cathode), the microplasma discharge process can be explained by a cold cathode arc scheme in a gaseous medium. The duration of the microplasma discharge was mostly determined by the amount of energy in the capacitor and inductor at the moment of breakdown. However, it can be noted from Figure 5.3, that the termination time of microplasma discharge varied in the range of 21-25 μs, resulting in the variation of microplasma discharge duration (17.6-21 μs for 10ASW and DSW) under the same conditions. The variation of duration of the pre-heating phase results in the variation of energy stored in the capacitor up to 4 mJ; however, this energy difference is not sufficient to cause a 4-μs difference in the microplasma discharge duration.

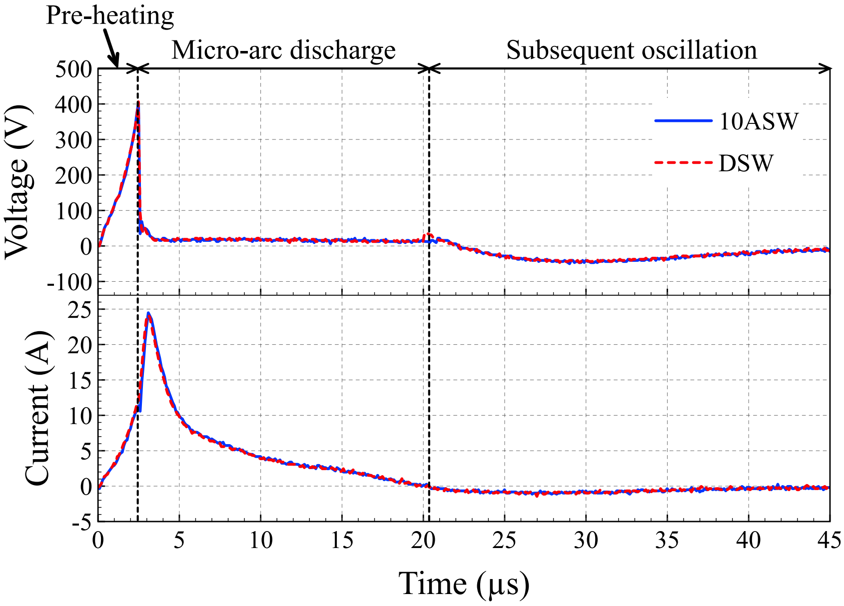

Figure 5.3. Voltage and current waveforms of micro-arc discharges generated in 10ASW and DSW using Pd alloy needle electrode, 67 μH inductor and 220 nF capacitor charged to 650 V.

Considering that the variation of energy stored in the system at the moment of breakdown had no significant influence on the microplasma discharge duration, it can be assumed that the instability in duration of the discharge is related to the dynamics of the bubbles, processes in the plasma, and changes in the liquid-gas interface. The instability in duration of microplasma discharges resulted in insignificant variations of intensity of measured spectra owing to the accumulation of optical emission during the entire discharge.

Typical optical emission spectra for the microplasma discharge generated in 10ASW and DSW by using a Pd alloy needle electrode, 67-μH inductor, and 220-nF capacitor charged to a resulting voltage of 650 V are shown in Figure 5.4. It can be noted from the spectra that the positions of all observed peaks were the same for micro-arc discharges operated in 10ASW and DSW, which implies that the origins of the optical emission peaks were the same in both liquids. It was assumed that the optical emission peaks in the spectra originated primarily from the materials present in 10ASW and the electrodes.

For the assignment of emission peaks appearing in the spectra, atomic spectral lines of components of 10ASW (Table 3.1) and materials used in the electrodes (elemental composition of the Pd alloy is presented in Table 3.2) were compared to the NIST database [76].

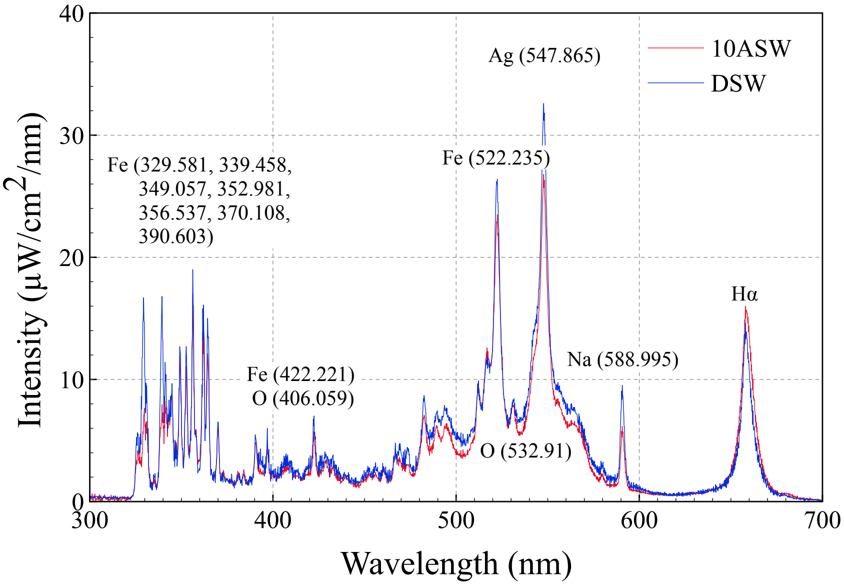

Figure 5.4. Optical emission spectra of micro-arc discharges generated in 10ASW and DSW using Pd alloy needle electrode, 67 μH inductor and 220 nF capacitor charged to 650 V.

The similar shape and intensity of the Hα peak for both liquids showed that the plasma characteristics (electron density and temperature) were almost the same. Owing to the overlapping of the Hβ peak with a large number of other emission peaks in the measured spectra, the electron densities and temperatures were roughly estimated using only the Hα peak. The Hα peak was fitted with a Voight function, and the Voight fitting consisted mostly of the Lorentz component while the Gauss component was negligibly small. Electron density can be estimated using fractional widths $\alpha_{1/2}$, $\alpha_{1/4}$, and $\alpha_{1/8}$ from the line centre (where Stark profiles have 1/2, 1/4, and 1/8 of their intensities, respectively) and Equation (5.1) [77,78].

$$N_e(H_\alpha) = 8.02 \times 10^{12} (\Delta\lambda_{1/2}/\alpha_{1/2})^{3/2}\ \text{cm}^{-3} \tag{5.1}$$

where $\Delta\lambda_{1/2}$ is the full width at half maximum (FWHM) of the line in Å and $\alpha_{1/2}$ is the fractional width from the line centre, which is a weak function of electron density and temperature through the ion-ion correlation and Debye shielding correction. Precise values of $\alpha_{1/2}$ for the Balmer series can be found elsewhere [79]. For determining values missing in the table, the tabulated data were interpolated (Figure 5.5). By using Equation (5.1) and the values of fractional widths, the electron density and temperature can be estimated to be in the range of $(3.26 \pm 1.05) \times 10^{18}$ cm^{-3} and 9000-15000 K, respectively. The estimated values can be considered typical for the arc discharge (Figure 2.3), which correlates well with the assumption that the observed microplasma discharge was arc discharge with a cold cathode.

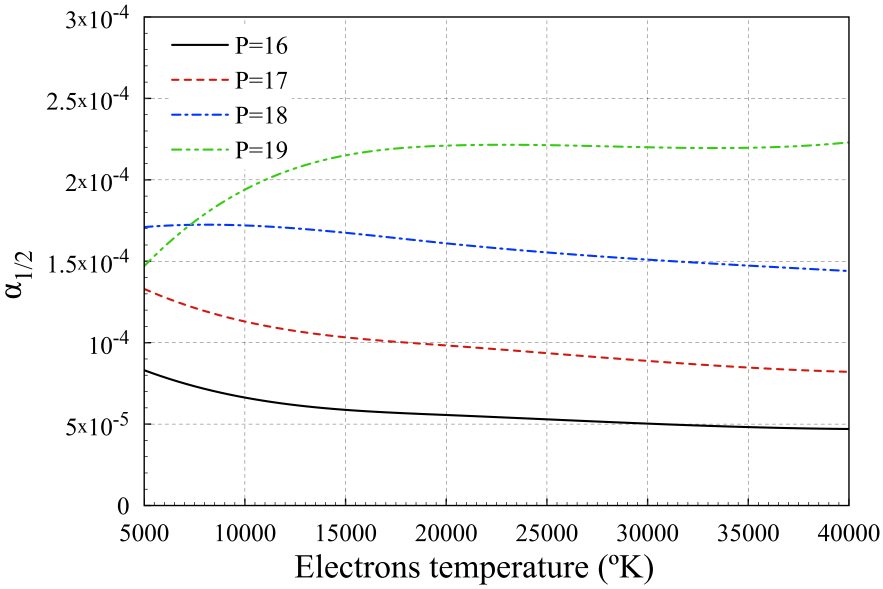

Figure 5.5. Dependency of interpolation of the tabulated fractional widths $\alpha_{1/2}$ on electron temperature for an electron density of $N \approx 10^P$ cm^{-3} (the legend shows the values of P).

In the spectra, peaks for Ag (547.865 nm), Na (588.995 nm), and Hα can be clearly detected. On the other hand, a strong peak at 522 nm cannot be clearly assigned owing to several possible elements such as Cl (522.136 nm) and Fe (522.235 nm), which have emission peaks close to 522 nm. The difference in wavelength between the peaks for Cl and Fe is less than the resolution of the spectroscope used. A possible approach for the separation of the emission peaks for materials present in the electrodes and materials present in the analysed liquid is the use of optical emission spectra of microplasma discharge in ultrapure water as reference. For the generation of microplasma discharges in low-conductivity liquids (such as ultrapure water), a different scheme with a high-voltage power supply is required because the used pulse current circuit does not work in the case of low-conductivity liquids.

To identify unassigned peaks [such as the 522-nm peak in Figure 5.4], spectra of microplasma discharges generated in reference solutions can be used. In the case of reference solutions, microplasma discharges can be reproducibly generated because the reference solutions have sufficient conductivities, which are close to the conductivity of sea water. As shown in Figure 5.6, for assigning the 522-nm peak, two types of liquids were used as reference solutions: solutions containing Cl ($CaCl_2$ and HCl) and solutions without Cl (Na_2SO_4, NaOH, and NaF). In the observed spectra, the emission peak at 522 nm appeared in all reference solutions, which confirms that the emission peak originates from a material used in the electrodes. This further confirms that the emission peak cannot be assigned to Cl (522.136 nm); thus, it can be clearly assigned as Fe (522.235 nm).

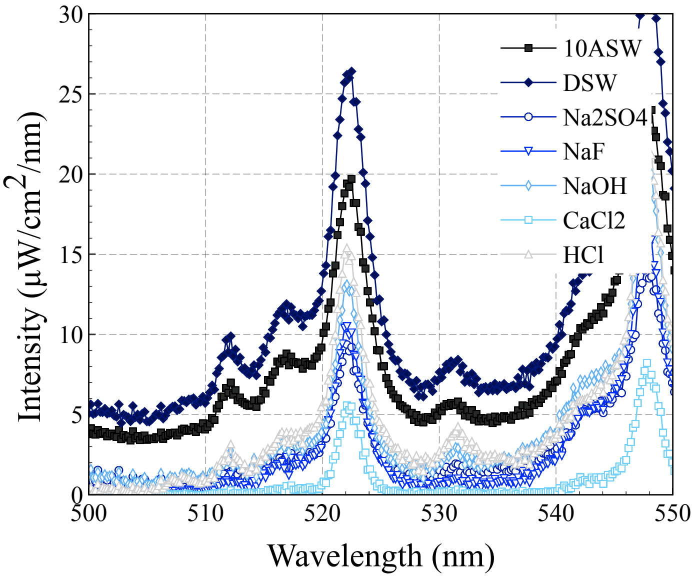

Figure 5.6. Comparison of optical emission of micro-arc discharges generated in 10ASW, DSW and reference solutions in the area of emission peak at 522 nm.

Owing to the complex elemental composition of sea water and materials with a high intensity of optical emission used in the Pd alloy needle electrode (Table 3.2), many peaks with similar wavelengths appeared for different materials in the range of 350-550 nm. The low resolution of the spectroscope used, relatively high noise level, continuum emission, and broadening of peaks make the assigning procedure using only a database of spectral lines impossible. In such a condition, one possible approach exists for elemental composition analysis – the use of a reference solution, as in the assigning of the Fe (522.235 nm) peak. Many other peaks observed in the spectra (Figure 5.4) for Fe (329.581, 339.458, 349.057, 352.981, 356.537, 370.108, 390.603, and 422.221 nm) were assigned using the reference solution method.

5.5 Optical emission spectra Pt needle

Typical current and voltage waveforms for microplasma discharges generated in 10ASW and DSW by using a Pt needle electrode, 67-μH inductor, and 220-nF capacitor charged to a resulting voltage of 650 V are shown in Figure 5.7.

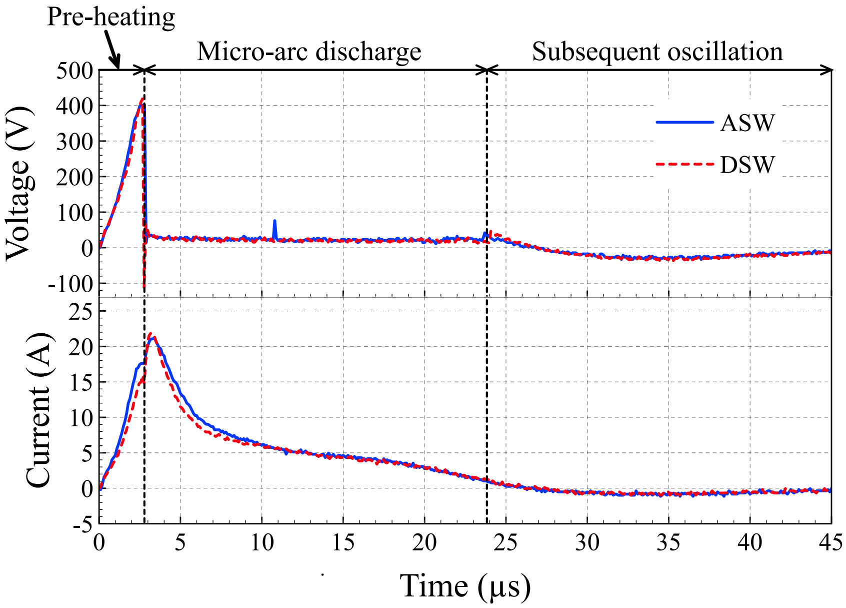

Figure 5.7. Voltage and current waveforms micro-arc discharges generated in 10ASW and DSW using Pt needle electrode, 67 μH inductor and 220 nF capacitor charged to 650 V.

The durations of the pre-heating and micro-arc discharge phases for the Pt needle electrode case were 2.5-3 μs and 17-22 μs, respectively, which are similar to the Pd alloy needle electrode case. The similar current and voltage waveforms between the Pt and Pd alloy needle electrode cases can be explained by the same discharge mechanism. However, owing to the difference in conductivity (approximately 30 × 10^6 S/cm for Pd alloy and 9.3 × 10^6 S/cm for Pt) and shape of the electrode tip, an insignificant difference in the current and voltage waveforms can be observed. The materials of both the needle electrodes have melting temperatures below the temperature required for generating the arc discharge with a hot cathode, resulting in a cold cathode arc process scheme [53]. It can be concluded that the use of different materials with low melting temperatures, such as Pt and Pd alloy, for the needle electrode does not strongly affect the microplasma discharge process.

Typical optical emission spectra for the microplasma discharges generated in 10ASW and DSW by using a Pt alloy needle electrode, 67-μH inductor, and 220-nF capacitor charged to a resulting voltage of 650 V are shown in Figure 5.8. Because the peak positions in the spectra measured for both liquids are the same, the emission spectra originated mostly from materials present in 10ASW and the electrodes.

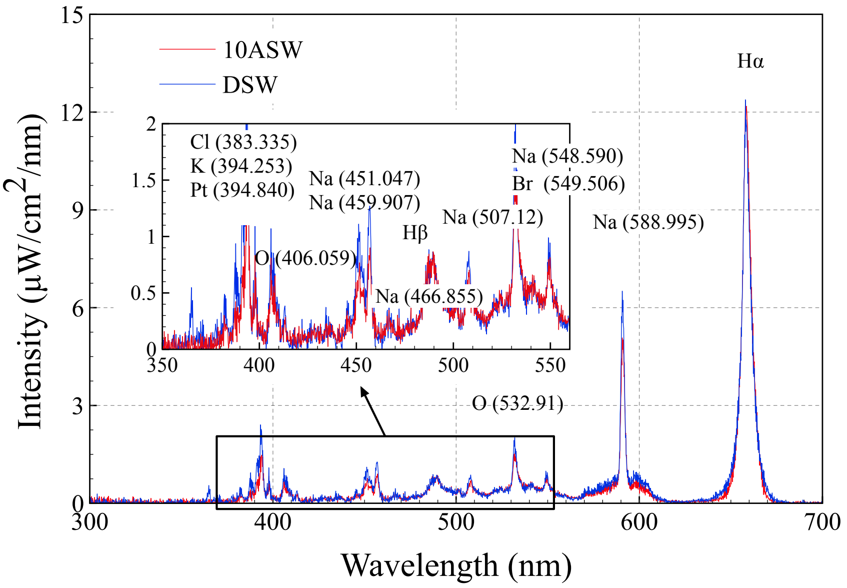

Figure 5.8. Optical emission spectra of micro-arc discharges generated in 10ASW and DSW using Pt needle electrode, 67 μH inductor and 220 nF capacitor charged to 650 V.

In the case of a Pt needle electrode, only peaks for Na (588.99 nm), Hα, and Hβ can be clearly assigned. For identifying the other peaks shown in Figure 5.8 [Cl (383.335 nm), K (394,253 nm), Pt (394.840 nm), Na (451.047, 459.907, 466.855 and 548.590 nm) and Br (549.506 nm)], the approach of using reference solutions was applied. A significant difference in the optical emission spectra can be observed in comparison to the Pd alloy needle electrode case. Owing to the decrease of the number of emission peaks compared to the Pd alloy needle electrode case, the Hβ peak could be clearly assigned.

The Hβ peak observed in the spectra allowed the precise estimation of electron temperature by using the integrated intensity ratio of Hα and Hβ peaks, as expressed in Equation (5.2) [77]

$$kT_e = (E_n - E_m) ln\left(\frac{A_m g_m \lambda_n i_n K_n}{A_n g_n \lambda_m i_m K_m}\right) \tag{5.2}$$

where $i_{n,m}$ are spectrally integrated emission line intensities given by Equation (5.3) [77]

$$i_{n,m} = \int I_{n,m}(\omega) d\omega \tag{5.3}$$

Considering an accuracy of ±10% of the method, electron temperature can be estimated in the range of 12300 ± 1230 K. By using Equation 5.1 and fractional width for the estimated electron temperature, electron density can be estimated in the range of $(2.87 \pm 0.91) \times 10^{18}$ cm^{-3}.

The estimated electron density for the Pt needle electrode case was in the range of typical values for arc discharge (Figure 2.3), and in the same manner as for the Pd alloy needle electrode case, it can be concluded that the microplasma discharge process follows a cold cathode arc discharge scheme owing to the low melting temperature of Pt [53].

It can be noted that the use of different materials for the needle electrode causes significant changes in the measured optical emission spectrum. In the case of the Pd alloy needle electrode, mostly elements from the needle electrode were observed in the spectra owing to the high number of components with strong optical emission in the alloy. In contrast, Pt shows relatively low optical emission, which results in the observation of emission peaks mostly from the elements present in the sea water (Table 3.1).

5.6 Optical emission spectra W needle

Current and voltage waveforms for five consistent micro-arc discharges generated in 10ASW operated using W needle electrode as anode, 67 μH indictor, and 220 nF capacitor charged to resulting voltage of 650 V are presented in Figure 5.9. The durations of the pre-heating and microplasma discharge phases for the W needle electrode case were 2.5-4 μs and 12-22 μs, respectively. Compared to the Pd alloy and Pt needle electrode cases, the use of the W needle electrode as the anode has a significant impact on the reproducibility of experiments. A large variation in the durations of pre-heating and micro-arc discharge phases causes poor reproducibility of the measured optical emission spectra, resulting in problems with averaging and a high noise ratio.

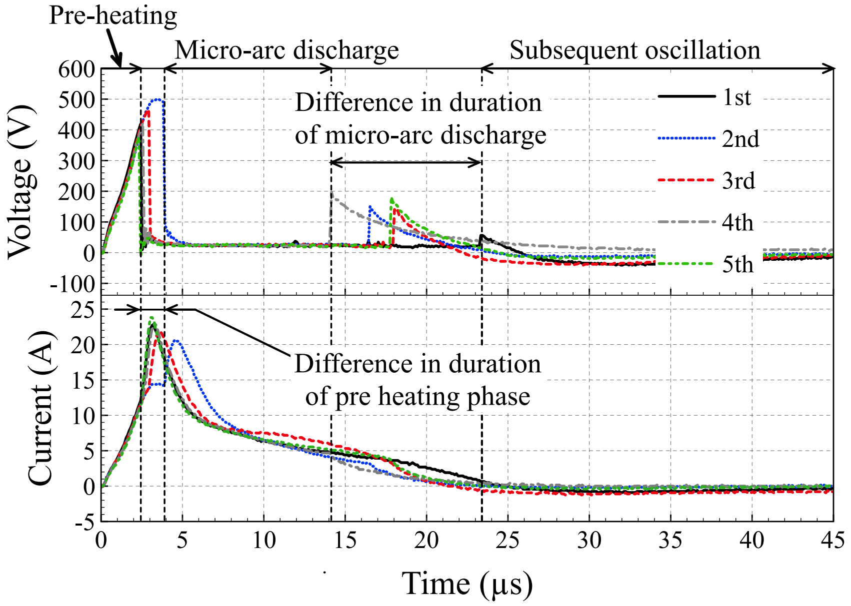

Figure 5.9. Voltage and current waveforms for five micro-arc discharges generated in 10ASW using W needle electrode as anode, 67μH inductor and 220 nF capacitor charged to 650 V.

Moreover, the use of the W needle electrode and 150-μH inductor allows the occasional generation of a second microplasma discharge during the subsequent negative oscillation phase. Current and voltage waveforms for micro-arc discharges generated in 10ASW by using a W needle electrode as the anode; 150-μH inductor; and 47-, 100-, and 220-nF capacitors charged to a resulting voltage of 650 V are shown in Figure 5.10. It could be observed that micro-arc discharges were generated during the negative oscillation for all values of capacitance, even in the case of the 47-nF capacitor. The possibility of generation of a second micro-arc discharge with the use of a small capacitance (47 nF) shows that the appearance of the second discharge does not strongly depend on the energy stored in the capacitor at the beginning of the process. The phenomenon of the second micro-arc discharge could be explained by the arc discharge with the hot cathode mechanism. The first arc discharge causes strong heating of the W needle electrode because of the high melting temperature of W. Considering a relatively small delay between the first and second microplasma discharges (4-8 μs), at the moment of initiation of the second discharge, the temperature of the needle electrode remained sufficiently high for thermal electron emission. At the beginning of the process, the needle electrode functioned as the anode; however, at the negative oscillation, it changed to the cathode, and owing to the high temperature of the needle electrode, it was possible to initiate the second micro-arc discharge with the hot cathode mechanism.

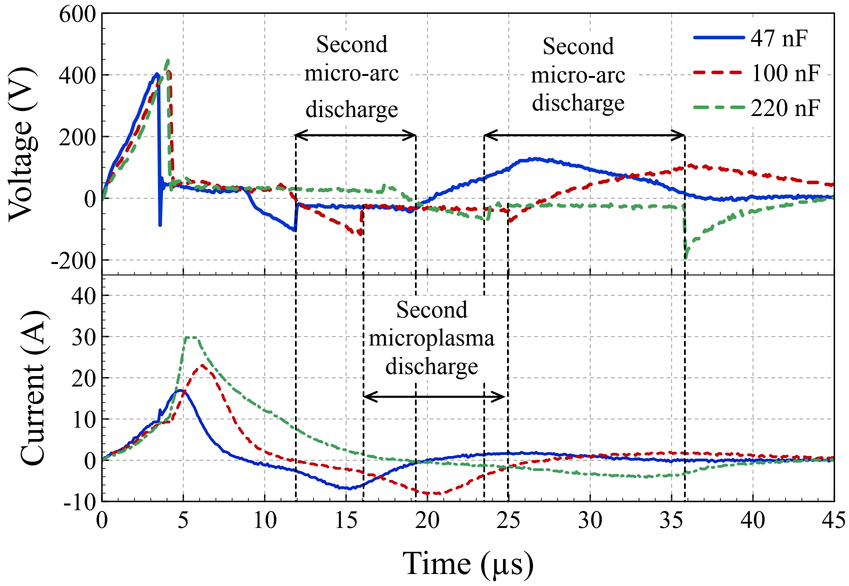

Figure 5.10. Voltage and current waveforms for micro-arc discharges generated in 10ASW using W needle electrode as anode, 150 μH inductance and 47, 100, 220 nF capacitors charged to 650 V.

To confirm this hypothesis, micro-arc discharges were generated in 10ASW using a W needle electrode as the cathode by applying a negative current pulse. Current and voltage waveforms for the arc discharge generated in 10ASW by using a W needle electrode as the cathode, 67-μH inductor, and 220-nF capacitor charged to a resulting voltage of 150 V are shown in Figure 5.11.

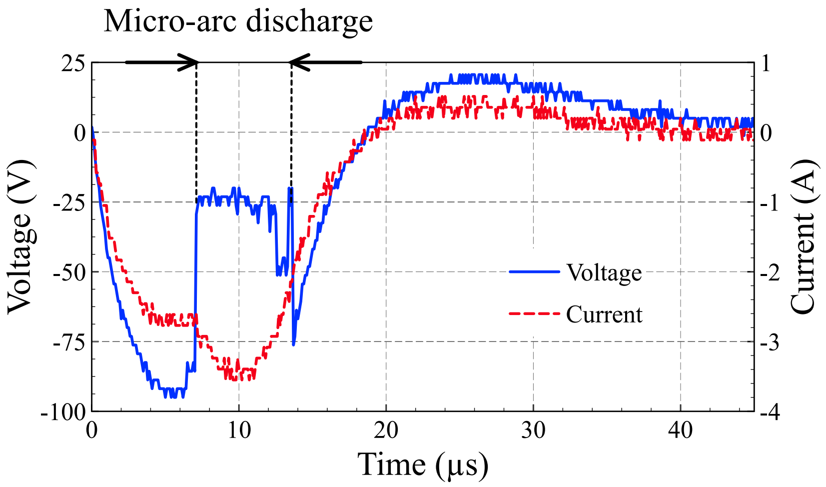

Figure 5.11. Voltage and current waveforms for micro-arc discharge generated in 10ASW using W needle electrode as cathode, 67μH inductor and 220 nF capacitor charged to 150 V.

It could be observed that, in the case of the W needle electrode functioning as the cathode, micro-arc discharges could be generated at low breakdown voltages (less than 100 V), which is similar to the breakdown voltages for the second micro-arc discharge during negative oscillation. On the other hand, in the case of the W needle electrode functioning as the anode, no microplasma discharge was generated under the same conditions (67-μH inductor and 220-nF capacitor charged to a resulting voltage of 150 V), for the generation of the microplasma discharge, it was necessary to charge the capacitor to a resulting voltage greater than 580 V, which could be explained by the different mechanisms of the cold cathode arc comparing to the previous case. Moreover, the second micro-arc discharge was not observed in the cases of the Pd alloy and Pt needle electrodes owing to the insufficient melting temperatures of Pd alloy and Pt, which correlates with the hypothesis that the second discharge during negative oscillation is arc discharge with the hot cathode mechanism. The second micro-arc discharge was unstable owing to the insufficient energy stored at the capacitor as well as low current and voltage values at the moment of discharge. Poor reproducibility of the microplasma discharges generated using the W needle electrode as the anode and the occasional generation of the second micro-arc discharge resulted in irreproducible measured optical emission spectra, which limits the application of microplasma discharges generated using a W needle electrode as the anode, especially for elemental composition analysis.

Typical optical emission spectra for the microplasma discharges generated in 10ASW using a W needle electrode as the anode, 67-μH inductor, and 220-nF capacitor charged to a voltage of 650 V are shown in Figure 5.12.

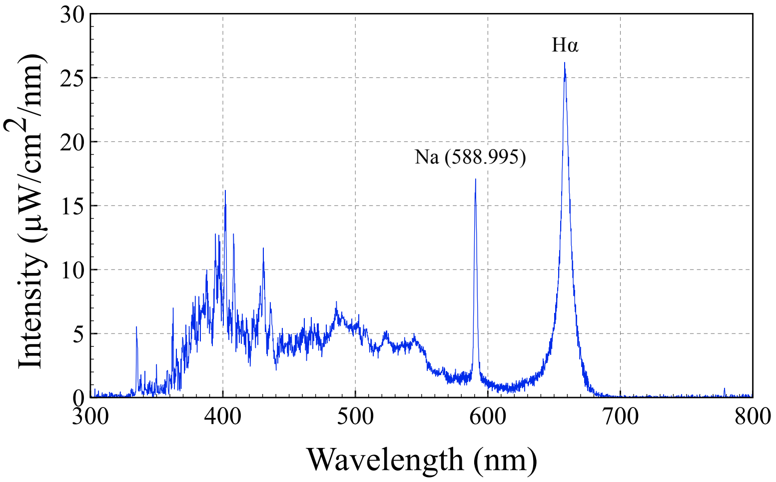

Figure 5.12. Optical emission spectra of microplasma discharge operated using W needle electrode as anode, 67μH inductor and 220 nF capacitor charged to 650 V.

Because the noise level is comparable to the intensity of emission peaks and the reproducibility of measured spectra is poor, only the most intense emission peaks for Hα, Na, and W were assigned.

To prevent the second microplasma discharge during the negative oscillation, the W needle electrode was originally used as the cathode by applying a negative voltage. Typical current and voltage waveforms for microplasma discharges generated in 10ASW using a W needle electrode as the cathode, 150-μH inductor, and variable capacitors (47, 100, and 220 nF) charged to a voltage of 650 V are shown in Figure 5.13.

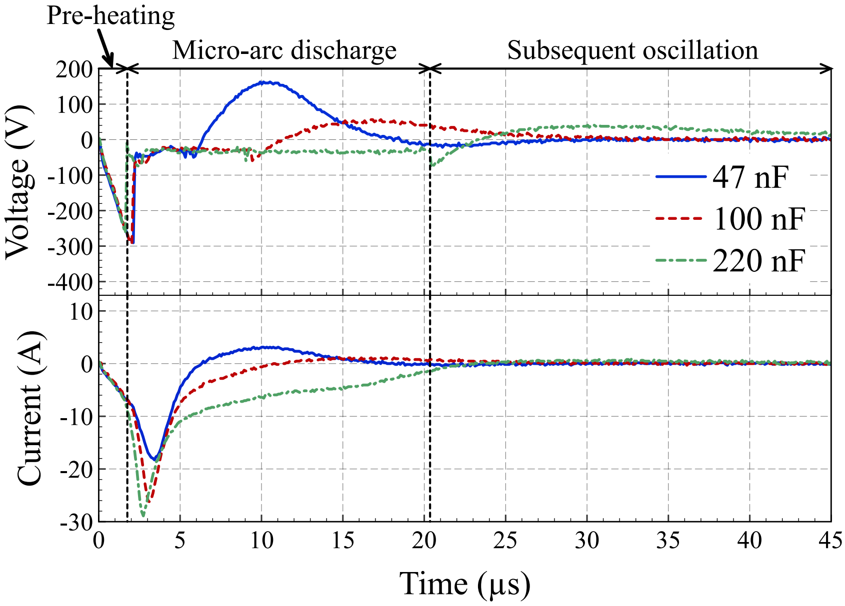

Figure 5.13. Voltage and current waveforms for micro-arc discharges generated in 10ASW using a W needle electrode as cathode; 150-μH inductor; and 47-, 100-, and 220-nF capacitors charged to 650 V

In this case, during the oscillation subsequent to termination of the first microplasma discharge, the high-temperature W needle electrode functioned as the anode owing to the reversed voltage, when the cathode was a Pt plate, which prevented the second micro-arc discharge with the hot cathode mechanism. Moreover, the use of the needle electrode as the cathode allows the generation of highly reproducible microplasma discharges owing to the arc discharge with the hot cathode mechanism, which positively impacts the optical emission measurements and allows precise analysis of the peaks of emission spectra. On the other hand, because the melting temperatures of Pt and Pd alloy are less than that of W (3695 K for W), the present method is not applicable to the previous cases and is limited to the case of needle electrodes with materials having a sufficient melting temperature for generating the hot-cathode arc discharge.

Typical optical emission spectra for microplasma discharge generated in 10ASW and DSW by using a W needle electrode, 67-µH inductor, and 220-nF capacitor charged to 650 V are shown in Figure 5.14. Because of the same peak positions in the spectra measured for both liquids, it can be assumed that the emission spectra originated primarily from materials present in 10ASW and the electrodes. In the observed spectra, peaks for Hα, Hβ, and Na (588.99 nm) can be clearly detected. Because the microplasma discharge was more stable than in the previous cases, it was possible to observe the O (777.194 nm) peak. However, there were several emission peaks, which required the use of reference solutions to be assigned. By using spectra of discharges in the reference solutions, the emission peaks can be assigned as W (382.011, 387.386, 392.436, and 397.547 nm). As expected, owing to the relatively high optical emission of W, peaks for W were dominant in the measured spectra.

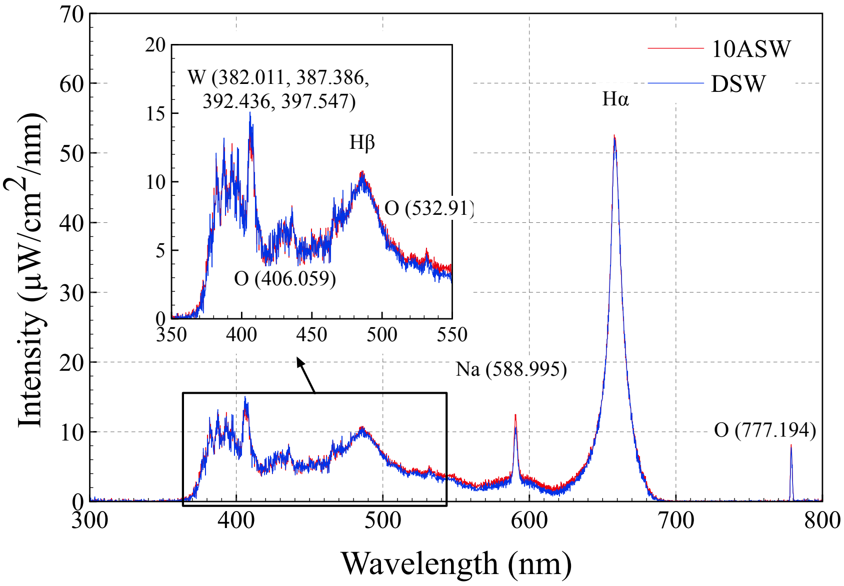

Figure 5.14. Optical emission spectra of micro-arc discharges generated in 10ASW and DSW using a W needle electrode as cathode, 67-µH inductor, and 220-nF capacitor charged to 650 V.

By using the same approach as for the Pt needle electrode case, the electron density and temperature can be estimated to be in the range of (1.86 ± 0.84) × 10^{18} cm^{-3} and 11800 ± 1180 K, respectively. The estimated electron temperature and density for the W needle electrode case are in the range of typical values for arc discharge (Figure 2.3).

5.7 Comparison of OES with different needles

Comparing all the presented spectra of microplasma discharges generated using Pd alloy, Pt, and W needle electrodes, significant differences among the spectra can be noted and related to the materials of the used electrodes.

The comparison of optical emission spectroscopy (OES) spectra of discharges generated using electrodes based on various materials can be used for the identification of emission peaks, in addition to the comparison of the spectra of reference solutions with the spectra of the liquid to be examined. In the experiments, two emission peaks were observed at wavelengths close to 406 and 533 nm. Moreover, these peaks appeared in all measured OES spectra for microplasmas generated using any of the three available needle electrodes (Pd alloy, Pt, and W) and in all used liquids (10ASW, DSW, and reference solutions). It can be concluded that the emission peaks originated from elements present in all the conducted experiments. A possible origin of the peaks can be the Pt from the plate electrode or pure water, which were present in all experiments. However, only oxygen has emission peaks at wavelengths close to those of the observed peaks; therefore, it can be considered that the peaks are O 406.059 nm and O 532.91 nm.

The observed results showed that, for the elemental composition analysis of sea water, it is necessary to choose electrode materials with low optical emission to avoid peaks of the electrode materials in the measured optical spectra. Moreover, owing to the high chemical activity of sea water, materials used in the electrodes should be chemically stable. Considering these two criteria, the most promising electrode material for the elemental composition analysis of sea water is Pt owing to its relatively low optical emission and chemical stability.

On the other hand, the optical spectra of microplasma generated using the Pd alloy and W needle electrodes show the possibility of identification of metals from the electrodes, even in small concentrations (0.02% of Fe in the Pd alloy needle), which makes the introduced method applicable for the detection of metals with high optical emission (such as rare-earth and rare metals) in sea water. Moreover, measurements were conducted using a simple spectroscopy setup, which is promising for the development of a compact analytical tool for on-site measurements. The proposed method can potentially be applied for the exploration of underwater metal deposits owing to the higher concentration of metal ions in the sea water close to the deposits. However, for analysis of concentrations, further improvement in plasma stability and the optical emission measurement system is required.

5.8 Detection of Fe in sea water

Typical current and voltage waveforms for micro-arc discharges in 10ASW operated using 220 and 440 nF capacitors charged to 750 V (all other conditions were the same) are shown in Figures 5.15 (a) and (b), respectively. One of the important requirements for the application of micro-arcs in OES measurements and elemental composition analysis is the control of discharge duration and optical emission intensity. From the current and voltage waveforms of discharges operated using 220 and 440 nF capacitors, it can be noted that capacitance has a strong effect on discharge duration. This effect can be explained by the amount of energy stored in the capacitor at the start of the microplasma discharge. In the case the of the 440 nF capacitor, compared with that of 220 nF, a larger amount of energy stored in the capacitor at the end of the pre-heating phase enabled the increase in the duration of the micro-arc discharge from 10 to 15 μs and peak current from 12 to 21 A.

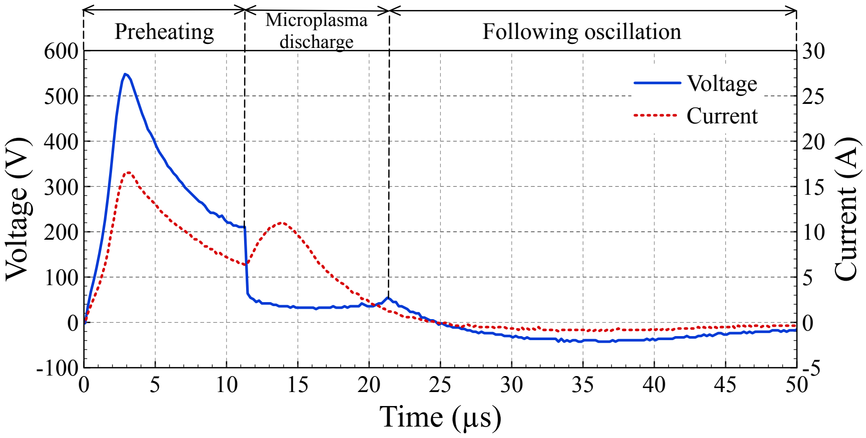

(a)

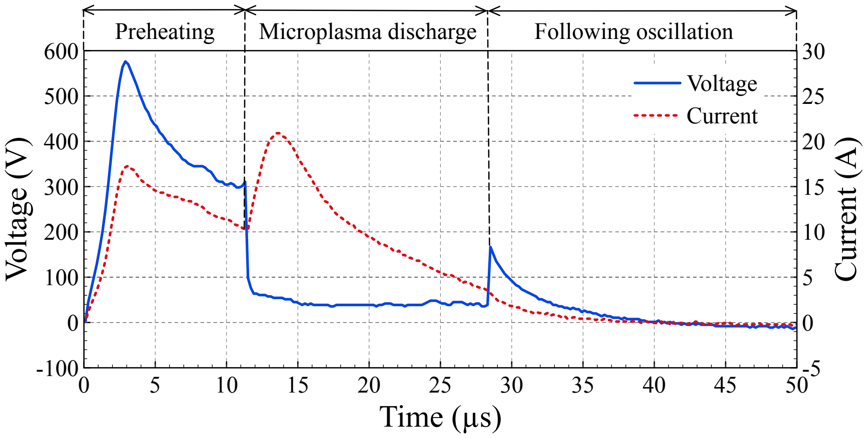

(b)

Figure 5.15. Typical current and voltage waveforms for micro-arc discharges operated in 10ASW using (a) 220 nF capacitor and (b) 440 nF capacitor.

From the emission spectra, as shown in Figure 5.16, it can be observed that the duration of the microplasma discharge and peak current causes significant differences in the measured optical emission spectra. In the case of the 220 nF capacitor, the duration of the microplasma discharge and peak current were 10 μs and 12 A, respectively, and, as a result, only four peaks (Hα, Hβ, Na, and O) with relatively low intensity are observed in the spectrum. For assigning the emission peaks, the NIST atomic spectra line database was used [76].

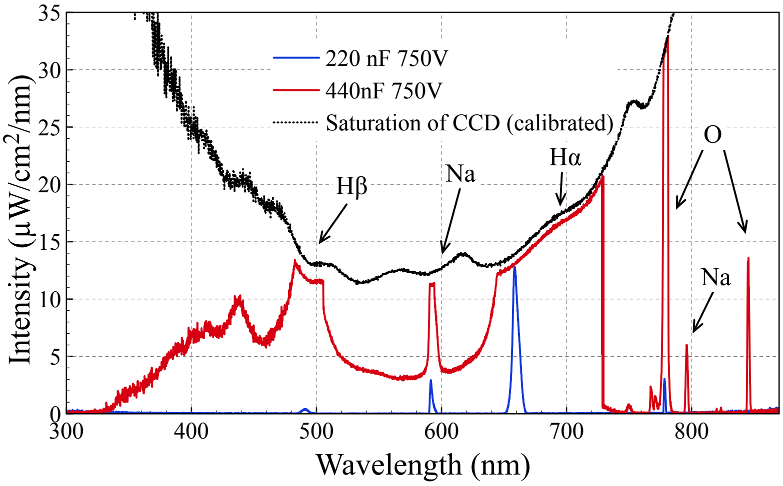

Figure 5.16. Comparison of optical emission spectra of discharges operated using 220 nF and 440 nF capacitors.

However, in the case of the 440 nF capacitor, the discharge duration and peak current were increased to 16 μs and 21 A, respectively, resulting in a significant increase in emission intensity. The intensity of the dominant peaks exceeded the saturation level of the CCD detector of the spectrometer. The wavelength dependence of sensitivity was calibrated, resulting in the curvature of saturation level. In addition, new emission peaks appeared, which were not detected previously. It is challenging to assign emission peaks in the region below 750 nm owing to the intensity of continuum emission, occasional saturation, significant noise, and numerous emission peaks from W and sea water. In the region greater than 750 nm, however, because of the longer duration of discharge with higher intensity when using the 440 nF capacitor, it becomes possible to observe some sharp emission peaks. Those peaks are not affected by continuum emission nor surrounded by a large number of very close emission peaks, which could be used for elemental analysis.

The optical emission spectra for microplasma discharges in 10ASW and a mixture of 10ASW with the standard Fe solution (the resulting concentration of Fe was 500 ppm) are shown in Figure 5.17 (a).

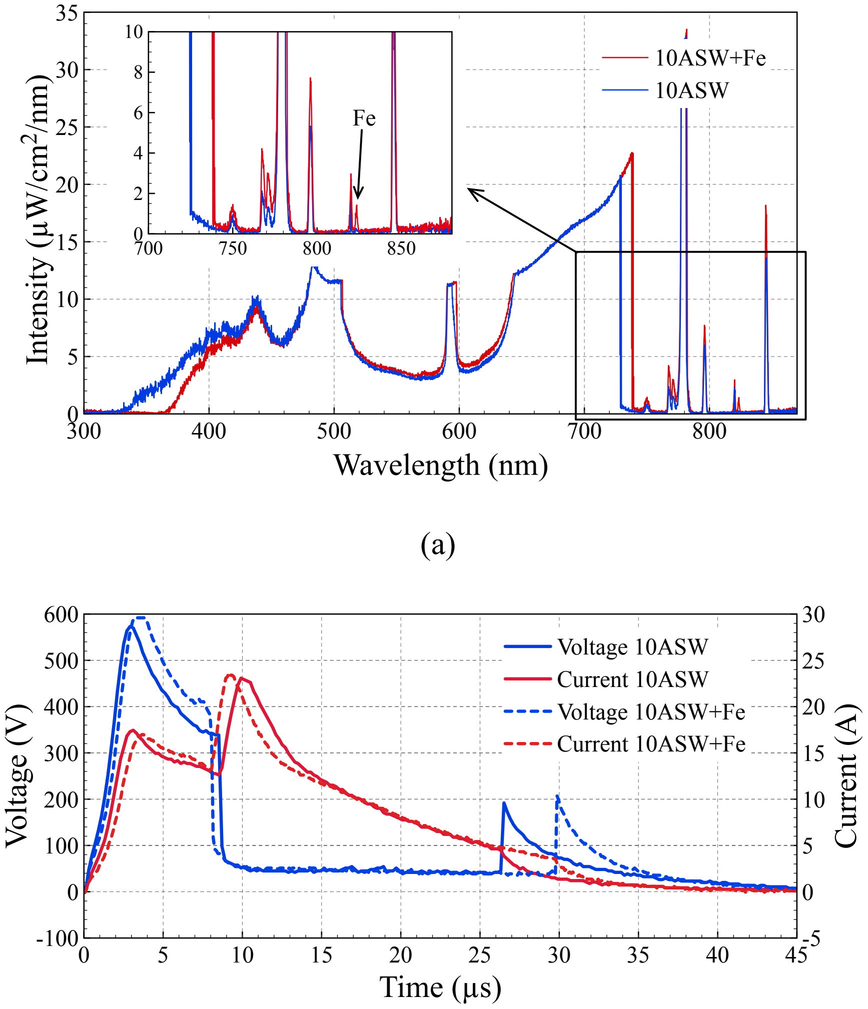

(a)

(b)

Figure 5.17. Comparison of (a) optical emission spectra and (b) current and voltage waveforms for discharges operated in 10ASW and mixture of 10ASW and standard Fe solution.

It can be observed that in the case of the solution with Fe, an additional peak appeared in the spectrum at 823 nm, which was not observed in 10ASW. A small difference can be observed in the current and voltage waveforms [Figure 5.17 (b)] between these discharges. It can be assumed that the difference in discharge characteristic is related to an insignificant change in electrical conductivity upon the addition of Fe solution to 10ASW. Despite the small difference in discharge duration, the total energy delivered to the microplasma may be considered approximately the same owing to the small amount of current remaining at the end of the discharge. Moreover, similar shapes of the Hα and Hβ emission peaks confirm approximately the same plasma parameters for micro-arcs generated in 10ASW and the mixture of 10ASW and a Fe solution. Considering these similar plasma parameters, it can be concluded that the emission peak at 823 nm originates from Fe in the solution and can be assigned as Fe [823.716 nm, transition from level 3d6(5D)5s to level 3d6(5D)5p].

To examine the detection limit of Fe concentration in the present system, discharges were operated in the mixtures of 10ASW and standard Fe solutions of different concentrations (200, 300, 500, and 1000 ppm of Fe). The enlarged spectra for the solutions with different concentrations of Fe are shown in Figure 5.18 (a). Moreover, to confirm the assignment of the emission peak at 819 nm, the emission spectra of the NaCl reference solution is added to Figure 5.18 (a) as an example.

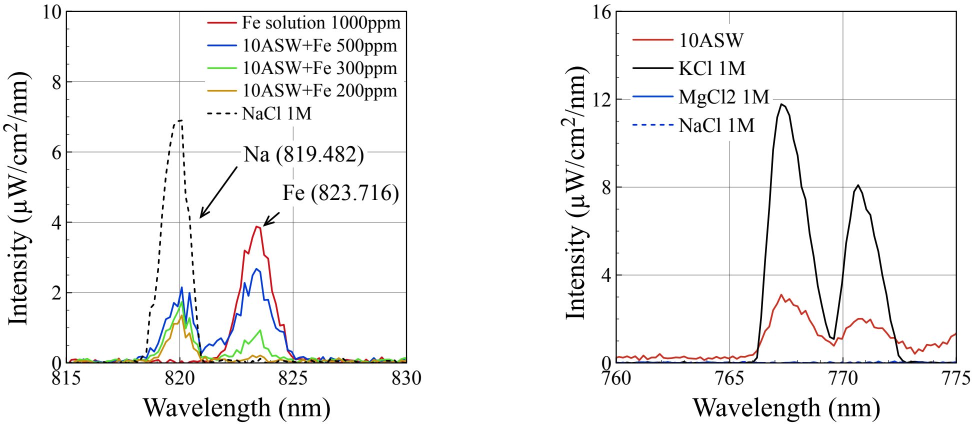

(a) (b)

Figure 5.18. Optical emission spectra of micro-arc discharges generated in (a) solutions with various concentrations of Fe for defining detection limit and (b) reference solutions for assignment emission peaks.

Considering the observation that the emission peak at 819 nm appeared only in solutions that contained Na, the peak can clearly be assigned to Na (819.482 nm). For the comparison of OES measurements at different Fe concentrations, owing to some instabilities of discharges with variation of the measured optical emission intensity, the similarity of clearly identified peaks, such as Na (819.482 nm), Hα, and Hβ, was confirmed. In the spectra, a strong correlation of the Fe emission peak (823.716 nm) intensity with the Fe concentration in solutions was observed. The Fe emission intensity was maximum in the standard Fe solution (1000 ppm) without 10ASW. The Fe emission intensity gradually decreased with decreasing concentration of Fe from 500 to 300 ppm. However, it can be noted that the Fe peak intensity was not proportional to the concentration of Fe. Despite choosing spectra with similar intensities and shapes of well-assigned peaks, it was challenging to find spectra with exactly the same intensity of all emission peaks except for Fe. This noted problem causes variations of the intensity of the Fe emission peak, which makes concentration analysis challenging and limits the present setup to impurity detection applications. With the decrease in the concentration of Fe to 200 ppm, there was no significant Fe peak appearing at the wavelength close to 823.716 nm. The emission peak for Fe at a concentration of 200 ppm was comparable to the noise level in this experiment. It can be concluded that the detection limit of Fe in sea water when using this experimental configuration is 300 ppm.

Additionally, by using the same approach as that for the Na emission peak, unidentified peaks at 767 and 771 nm could be assigned to K, owing to the observation that the emission peaks appeared only in the solutions containing K (10ASW, KCl) but not in the other solutions ($MgCl_2$, NaCl), as shown in Figure 5.18 (b).

The proposed method can be used for the on-site detection of metals (such as Fe or rare metals) or other elements with high optical emission in sea water. It is possible to conduct the measurements with a simple spectroscopy setup, which appears applicable to the design of a compact system for onsite measurements. The proposed method can be potentially applied to the exploration of underwater metal deposits, because of the higher concentrations of metal ions in water close to the deposits. For precise concentration analysis, however, further improvements of plasma stability (electrode system and discharge circuit) and the optical emission measurement system (reducing the signal-to-noise ratio, improving the focusing system, use of a spectroscope with a higher resolution, time-resolved spectroscopy) are required.

5.9 Conclusions

In this study, we performed the elemental composition analysis of sea water using the optical emission spectroscopy of micro-arc discharges. For that purpose, we investigated micro-arc discharges generated in 10ASW and DSW by using various experimental setups. By analysing the optical emission spectra, we confirmed that the presented setup and experimental conditions allow the generation of micro-arc discharges with a cold or hot cathode (depending on the electrode materials) in highly conductive sea water. Moreover, the generation of micro-arc discharges was confirmed by estimation of electron temperatures and densities for discharges generated under various conditions. The use of needle electrodes with a high melting temperature (such as W) resulted in the change of discharge mechanism and problems with the reproducibility of measurements (owing to the appearance of the second unstable micro-arc discharge with the hot cathode mechanism), which can be solved using a needle electrode as the cathode from the beginning of the process.

For the analysis of the optical emission spectra and identification of emission peaks, the optical emission spectra of reference solutions were used. It was confirmed that, by using the reference solution method, elemental analysis can be performed using a simple spectroscopy setup, which suggests that the presented approach is promising for the development of compact analytical tools. In the observed spectra, emission peaks for sea-water elements (H, O, Na, Cl, K, and Br) and electrode materials (Ag, Fe, W, and Pt) were clearly assigned. An emission peak corresponding to the incorporated Fe was successfully and clearly identified in the emission spectra. The intensity of the Fe peak increased with increasing Fe concentration. The detection limit in this experiment was 300 ppm.

Atomic emission spectroscopy was successfully applied to the elemental composition analysis, which demonstrates the potential of the proposed method for the on-site analysis of water recourses and the exploration of underwater deposits of metals and other substances. The proposed method potentially enables the design of a compact device for on-site elemental composition analysis of sea water owing to its simple experimental setup and small power supply.

Chapter 6. Micro-arc discharge in sea water at high pressure

6.1 Introduction

One of the promising methods to identify elemental composition of water is a spectral analysis of different types of plasmas generated in examined liquid. Recent research shows that it is possible to generate microplasma discharges in highly-conductive liquids using low voltages and compact setup. Moreover, use of micro-arc discharges looks promising for analysis of deep-sea water due to increase of optical emission intensity from the arc with increase of pressure. This work is the first challenge to generate micro-arc discharges in highly conductive and highly pressurized sea water for demonstration of on-site operation in deep-sea. It has been confirmed, in our previous studies, the micro-arc discharge process in highly conductive sea water is separated in three phases; pre-heating, micro-arc discharge and subsequent oscillation. Bubble formation during pre-heating phase plays key role in the ignition process for generation of micro-arc discharge in sea water at atmospheric pressure. The increase of pressure could have difficulty of bubble formation with resulting in poor reproducibility It is necessary to confirm that micro-arc discharges can be operated even at such a high pressure as deep sea.

6.2 Objective

In this part of the research, investigation of micro-arc discharges generated in highly-conductive sea water at high pressure will be presented. For that purpose, effect of the experimental conditions (electrode system, pressure, circuit parameters) on the discharge process was studied; moreover, reproducibility of generation of micro-arc discharges at high pressure was confirmed. For generation of micro-arc discharges at high pressure, high pressure chamber and two types of electrode systems were developed. Micro-arc discharges were successfully generated in highly conductive sea water at high pressure using same impulse current generator as for the atmospheric pressure case. Moreover, results measured for high pressure were compared to the atmospheric pressure case.

6.3 Experimental and methods

A schematic of the experimental setup is presented in Figure 6.1. Discharges were operated inside a high-pressure chamber using pulse current source. Pressure was sustained by high pressure pump (FLOM, Inc., Dual pump KP-22-01) and controlled by valve in a range of 0.1-19 MPa. The pulse current source, consisting of a capacitor (C = 440, 660 nF), inductor (L = 67, 100, 150 μH) and MOSFET switch was used to supply the discharge. The capacitor was charged through a resistor by a regulated DC power supply to resulting voltage of 650-800 V.

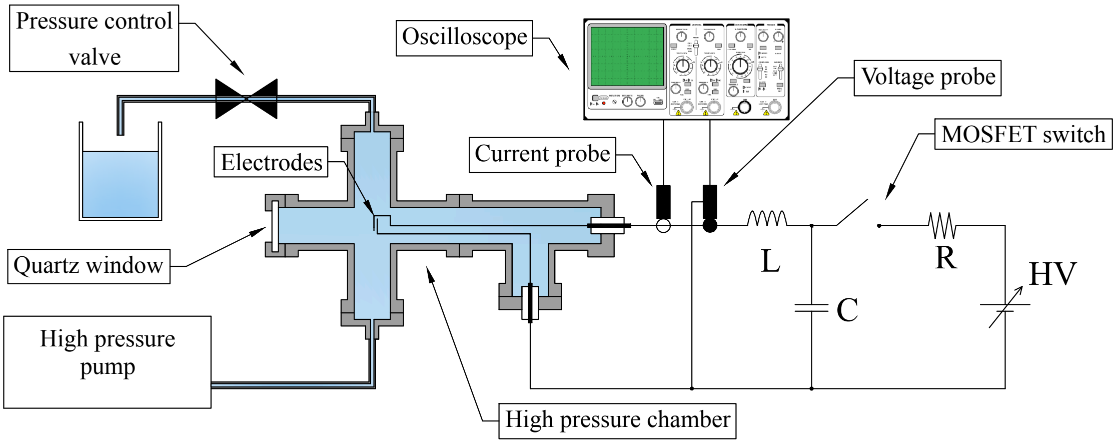

Figure 6.1. Experimental setup for generation of micro-arc discharges at high pressure.

In present experiments, discharges were operated in 10ASW using two types of electrodes, which were introduced inside the chamber. Schematic of two types of electrode systems are presented in Figure 6.2. In the case of pin-to-pin electrode system, two needle electrodes (NPS Inc. P26-10-20 × 1") were placed facing to each other with fixed gap of 150 μm. To reduce current trough the surrounding liquid, sides of the needle electrodes were insulated and only tip with length of 0.3 mm remained open. In the case of rod-to-rod electrodes, two pieces of stainless steel wire (Nilaco Company SUS304, 0.5 mm in diameter) were placed parallel with the gap of 150 μm. To avoid current through the surrounding liquid, most of side faces were insulated as it shown in Figure 6.2 resulting in width of the discharge gap of 1 mm.

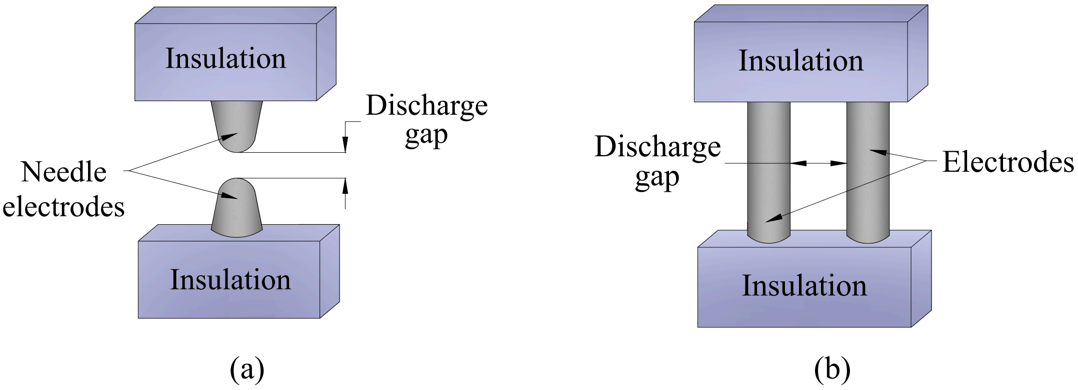

Figure 6.2. Schematic of (a) pin-to-pin and (b) rod-to-rod electrode systems.

The voltage and current waveforms were stored in a digital oscilloscope using a high voltage probe and a current probe (IWATSU SS 281).

6.4 Generation of micro-arc discharge using pin-to-pin electrodes

Voltage waveforms for microplasma discharges generated in 10ASW using 150 µH inductor, 440 nF capacitor charged to voltages in a range of 650-800 V and various pressure in a range from atmospheric (0.1 MPa) to 17.5MPa are shown in Figure 6.3.

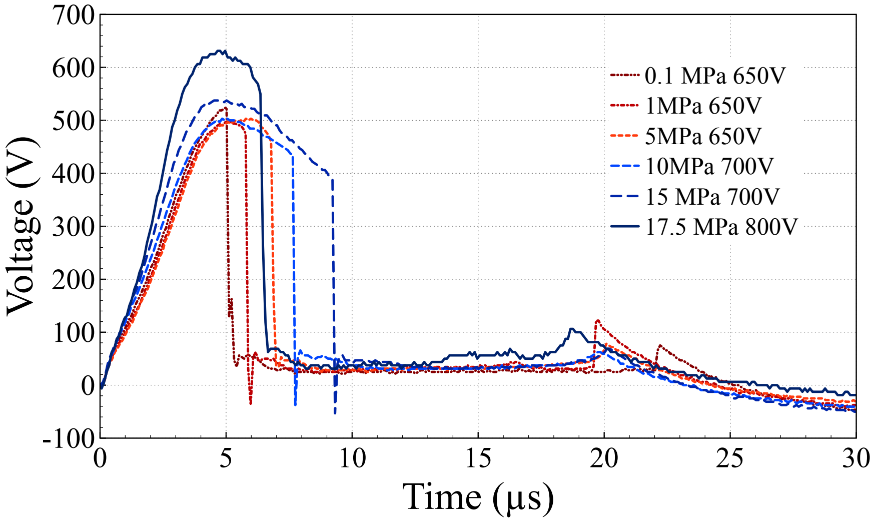

Figure 6.3 Voltage waveforms for microplasma discharges generated using 150 µH inductor, 440 nF capacitor, and various values of charging voltage of capacitor and pressure

By using the pin-to-pin electrode system, micro-arc discharges were successfully generated in highly conductive sea water even at high pressures up to 17.5 MPa which was equal to 1.75 km in depth for the first time. It could be observed that discharge process for the case of high pressure follows the same scheme as for the atmospheric pressure case: pre-heating phase, micro-arc discharge and subsequent oscillation. It was confirmed that pre-heating phase is paying the key role in the discharge process also at high pressure. From voltage waveforms, it could be observed that micro-arc discharges could be generated in a range of pressure from 0.1 to 5 MPa using the capacitor charged to 650 V. However, increase of pressure results in increase of duration of pre-heating phase from 5 µs for atmospheric pressure to 7 µs for 5 MPa. Moreover, for generation of micro-arc discharge at higher pressure, it was necessary to charge the capacitor to 700 V for 10-15 MPa case and to 800 V for 17.5 MPa.

These results clearly show that, for generation of micro-arc discharge at high pressure, it is necessary to deliver more energy during pre-heating phase. However, it was not possible to perform statistical measurements using the pin-to-pin electrode system due to erosion of the electrodes. For studying effects of pressure on the pre-heating energy, it is necessary to perform repeating measurements in the same conditions with variation of pressure. For experiments in the high pressure discharge chamber, electrodes were installed with a fixed gap without manipulation. The erosion of the needle electrodes, which was precisely discussed in chapter 4.6 (figure 4.12 (a)), resulted in increase of discharge gap. The increasing of the discharge gap limits the number of discharges possible to repeat using the same electrodes to 30-50 times depending on the conditions. By considering the problems of reproducibility using the pin-to-pin electrode system, precise study of effect of pressure on the pre-heating energy is quite difficult.

6.5 Generation of micro-arc discharge using rod-to-rod electrodes

The problem of erosion of needle electrodes could be solved using the rod-to-rod electrode system, as it shown on Figure 6.2 (b). Two rod electrodes are placed parallel with micro-gap and discharge is generated in the gap. Usage of the rod-to-rod electrode system significantly increases the facing surface of the electrodes in the gap, which allows the discharge to compensate damage caused by erosion. Even if a part of the electrode was locally damaged by arc, the configuration of whole the electrode system was almost same as before. The next discharge will be generated in another place of the discharge gap where electrodes remain not damaged. Moreover, due to larger size of the electrodes, comparing to the pin-to-pin case, heat transfer from the electrode surface to the bulk reduces damage caused by the high current. In the case of rod-to-rod electrode system, volume of the discharge gap was increased significantly comparing to the pin-to-pin electrodes with resulting in increase of energy required for pre-heating phase. To generate reproducible discharges at high pressure up to 19 MPa using the rod-to-rod electrode system, it was necessary to use 660 nF capacitor which was 33% larger than that in the pin-to-pin electrodes case charged to 750 V.

Current and voltage waveforms for three discharges generated in 10ASW at 19 MPa pressure using 150 μH inductor and 660 nF capacitor charged to 750 V are shown in Figure 6.4. Rod-to-rod electrode system allows us to generate reproducible micro-arc discharges even at high pressure up to 19 MPa which is equal to 1.9 km depth. It was found that duration of pre-heating phase could be change with pressure. Difference in duration of pre-heating phase could be explained by fluctuations in bubble formation process and dynamics of the bubbles in the discharge gap.

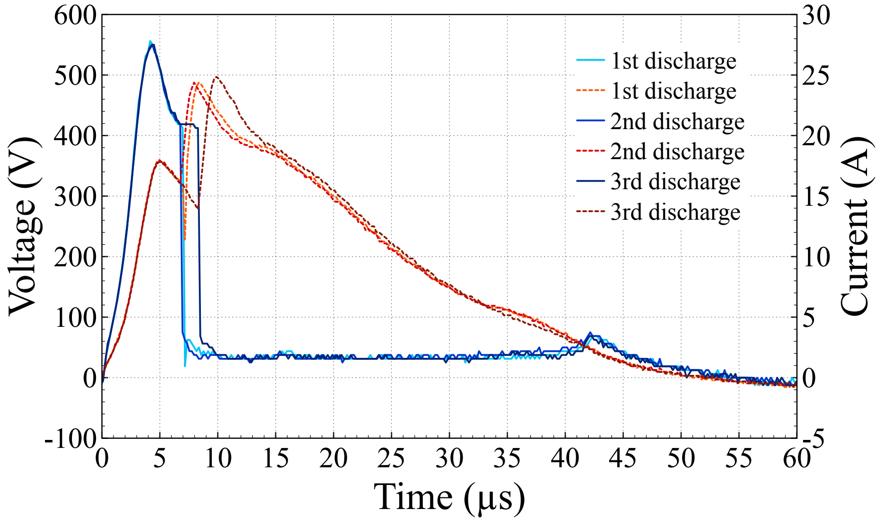

Figure 6.4 Current and voltage waveforms for three discharges generated in 10ASW at 19 MPa pressure using 150 μH inductor and 660 nF capacitor charged to 750 V.

To study effect of pressure on the energy required for pre-heating phase, discharges were generated at pressure in a range of 0.1-19 MPa using the same discharge conditions (150 μH inductor, 660 nF capacitor charged to 750 V, and same rod-to-rod electrode system with 150 μm discharge gap). Dependency of the energy consumed during pre-heating phase on the pressure is shown in Figure 6.5.

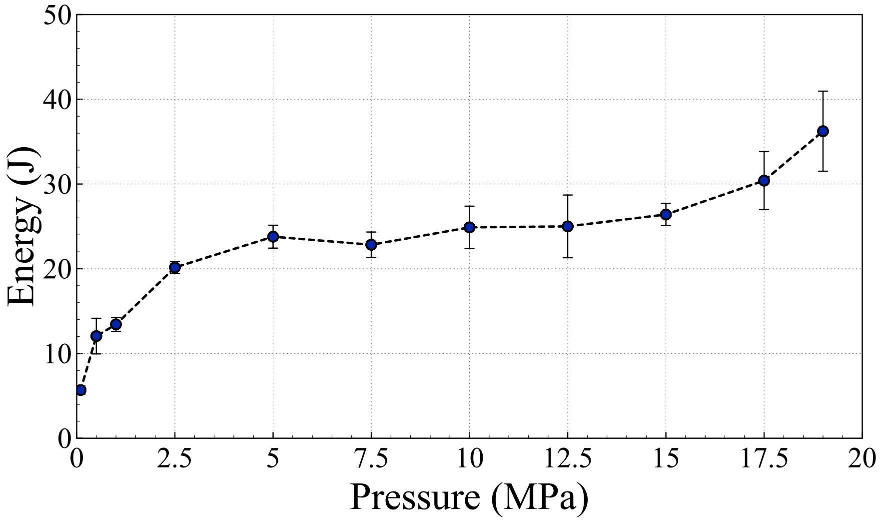

Figure 6.5 Effect of pressure on amount of energy consumed during pre-heating phase

The pre-heating energy was evaluated from current and voltage waveforms. In Figure 6.5, the plots of energy for each discharge condition were averages for three times of repeating discharges. The error bars represent instability of duration of pre-heating phase which was discussed above. It can be clearly observed that energy consumption during pre-heating phase is increasing with increase of pressure. The pre-heating energy for generation of discharge at atmospheric pressure was 5.5 μJ and that at 19 MPa was 36 μJ, and which was almost 7 times higher. A trend of increasing pre-heating energy with increase of pressure becomes clear while there is no clear explanation at this point for almost same energy during the range of pressure from 5 to 15 MPa.

6.6 Conclusions

Micro-arc discharges generated in sea water at high pressure were investigated. For generation of micro-arc discharges, electrodes were introduced into a high pressure chamber and discharges were generated by the same pulse current source as for atmospheric pressure case. Using a pin-to-pin electrodes system, micro-arc discharges were successfully generated in highly conductive sea water even at high pressures up to 17.5 MPa for the first time. Analysis of current and voltage waveform shows that process of generation of micro-arc discharge at high pressures is same to the atmospheric pressure case and that the process can be divided into three phases; pre-heating, micro-arc discharge and subsequent oscillation. Energy consumption on pre-heating phase was increasing with increase of pressure. The usage of pin-to-pin electrode system allowed us to generate micro-arc discharges at high pressure using relatively small amount of energy comparing to other types of discharges, due to strong electric field focusing between the electrodes with small volume of sea water owing to the insulation of side faces of needle electrodes. Erosion of the electrodes caused by high current during the discharge limits number of discharges times reproducibly generated using the same electrodes below 30. To overcome this disadvantage, a rod-to-rod electrode system was developed. In the case of rod-to-rod electrode system, due to increase of the surface of the electrodes, erosion caused by high current does not have significant impact on the reproducibility of the next discharge. In the case of rod-to-rod electrode system, volume of the discharge gap was increased with resulting in increase of power consumption by 30% by comparing to the pin-to-pin electrode system. By using the rod-to-rod electrode system, it was possible to generate reproducible micro-arc discharges at high pressures up to 19 MPa; moreover, due to improved durability of the electrodes, it was possible to make analysis of effect of pressure on the power consumption during pre-heating phase. It has been confirmed that the increase of pressure results in increase of power required for pre-heating phase. The evaluated pre-heating enargy n the case of 19 MPa was almost seven times higher than that for the atmospheric pressure case.

Chapter 7. Summary

In the study, systematic analysis of the micro-arc discharge in sea water and optical emission spectra of the plasma was presented in order to develop compact device for on-site measurements.

Micro-arc discharge was successfully generated in highly conductive sea water by applying pulse currents to the needle-to-plane electrodes placed with micro-gap. A custom-made pulse current source with tunable electric parameters was developed to supply the discharge. The microplasma was sustained by the cathode arc mechanism and the breakdown was induced not only by any critical voltage but by sufficient pre-heating energy. After optimization, the micro-arc plasma was ignited at 130 V, the minimum energy for pre-heating of sea water was 0.8 mJ and the minimum energy for the micro-arc plasma was 0.1 mJ. Two types of insulation of needle electrode were used to study the bubble formation process. The complete insulation of the side wall of needle electrode was successfully achieved by the PTFE spray coating. By using needle electrodes insulated by PTFE spray, it was confirmed that microplasma was initiated after bubble formation. It was clarified that the discharge occurs after filling the entire discharge gap with vaporized water. By using heat-shrinking tubing insulation on the side faces of needles, the current flow through the surrounding water was diminished with resulting in reduction of pre-heating energy, decrease of charging voltage required for ignition and/or increase of discharge duration.

Mathematical model of pre-heating phase was developed for investigation of the effect of shape of the needle electrodes tip on micro-arc generation process. Mathematical modelling results showed good agreement with experimental data. It has been confirmed from the results of the simulation that the shape of tip affected only on local process in the discharge gap and had no effect on current and voltage waveforms during the pre-heating phase. It was also confirmed that there was no effect of the needle electrode's tip shape on optical emission and electrodes could be successfully reused for repeating measurements. For usage of damaged needle electrodes repeatedly, however, it is necessary to strictly align the optical system including focusing lens.

The elemental composition analysis of sea water using the optical emission spectroscopy of micro-arc discharges was performed. For that purpose, micro-arc discharges generated in 10ASW and DSW by using various experimental setups were investigated. By analysing the optical emission spectra, it was confirmed that the presented setup and experimental conditions allow the generation of micro-arc discharges with a cold or hot cathode (depending on the electrode materials) in highly conductive sea water. The electron temperatures and densities in the micro-arc plasma were estimated by analysis on Hydrogen atomic emission peaks under various conditions. The use of needle electrodes with a high melting temperature (such as W) resulted in the change of discharge mechanism and problems with the reproducibility of measurements (owing to the appearance of the second unstable micro-arc discharge with the hot cathode mechanism), which can be solved using a needle electrode as the cathode from the beginning of the process.

For the analysis of the optical emission spectra and identification of emission peaks, the optical emission spectra of reference solutions were investigated. It has been confirmed that. by using the reference solution method, elemental composition analysis can be performed using the simple spectroscopy setup, which suggests that the presented approach is promising for the development of compact analytical tools. In the observed spectra, emission peaks for sea water elements (H, O, Na, Cl, K, and Br) and electrode materials (Ag, Fe, W, and Pt) were clearly assigned. It has been succeeded to detect 300 ppm of Fe ions intentionally added into 10ASW by the atomic emission spectroscopy. This study demonstrated the potential of the proposed method for the on-site analysis of water recourses and the exploration of underwater deposits of metals and other substances.

Micro-arc discharges generated in sea water at high pressure were investigated. For generation of micro-arc discharges in pressurized sea water, electrodes were introduced in a high pressure chamber and discharge was generated by the same pulse current source as for atmospheric pressure case. Using pin-to-pin electrodes system, micro-arc discharges were successfully generated in highly conductive sea water even at high pressures up to 17.5 MPa for the first time. Analysis of current and voltage waveforms showed that the process of generation of micro-arc discharge at high pressure was same as that of the atmospheric pressure case and could be divided into the three phases consisting of pre-heating, micro-arc discharge and subsequent oscillation. The power consumption in pre-heating phase was increased with increase of pressure. By using pin-to-pin electrode system, micro-arc discharges were generated at high pressure with relatively small amounts of energy as compared to other types of discharges due to strong electric field focusing between the electrodes with small volume of water in the discharge gap owing to the insulation of the needle electrodes side faces. The erosion of electrodes caused by high current during the discharge limits number of discharges times which could be reproducibly and repeatedly generated using the same electrodes to 30 times. To overcome this disadvantage, a rod-to-rod electrode system was developed. In the case of rod-to-rod electrode system consisting of 2 parallel metal rods, due to increase of the surface of the facing electrodes, possible erosion caused by high current does not have significant impact on the reproducibility of the next discharges. In the case of rod-to-rod electrode system, volume of the water in the discharge gap was increased with resulting in increase of power consumption by 30% as compared to the pin-to-pin electrode system. By using the rod-to-rod electrode system, it was enabled to generate reproducible micro-arc discharges at high pressures up to 19 MPa for many times due to improved durability of the electrodes. Effects of pressure on the power consumption during pre-heating phase has been successfully analyzed. It has been confirmed that increase of pressure results in increase of power required for pre-heating phase. The pre-heating energy for ignition of micro-arc discharge increased by 7 times at 19 MPa as compared to the atmospheric pressure.

References

[1] G.P. Glasby, Deep Seabed Mining: Past Failures and Future Prospects, Mar. Georesources Geotechnol. **20** (2002) 161–176.

[2] K. Bostrom, H. Kunzendorf, Marine Mineral Exploration., Elsevier Oceanogr. Ser. Elsevier, Amsterdam. **41** (1986) 21–53.

[3] P. Bruneton, Geological environment of the Cigar Lake uranium deposit, Can. J. Earth Sci. **30** (1993) 653–673.

[4] A.A. Gowen, R. Tsenkova, M. Bruen, C. O'donnell, Vibrational Spectroscopy for Analysis of Water for Human Use and in Aquatic Ecosystems, Crit. Rev. Environ. Sci. Technol. **42** (2012) 2546–2573.

[5] J.M. Lee, E.A. Boyle, Y. Echegoyen-Sanz, J.N. Fitzsimmons, R. Zhang, R.A. Kayser, Analysis of trace metals (Cu, Cd, Pb, and Fe) in seawater using single batch nitrilotriacetate resin extraction and isotope dilution inductively coupled plasma mass spectrometry, Anal. Chim. Acta. **686** (2011) 93–101.

[6] R.M. Boiteau, J.N. Fitzsimmons, D.J. Repeta, E.A. Boyle, Detection of iron ligands in seawater and marine cyanobacteria cultures by high-performance liquid chromatography-inductively coupled plasma-mass spectrometry, Anal. Chem. **85** (2013) 4357–4362.

[7] J. Wu, E.A. Boyle, Determination of iron in seawater by high-resolution isotope dilution inductively coupled plasma mass spectrometry after Mg(OH)2 coprecipitation, Anal. Chim. Acta. **367** (1998) 183–191.

[8] C.G. Wilson, Y.B. Gianchandani, Spectral Detection of Metal Contaminants in Water Using an On-Chip Microglow Discharge, IEEE Trans. Electron Devices. **49** (2002) 2317–2322.

[9] I. Rodushkin, T. Ruth, Determination of Trace Metals in Estuarine and Sea-water Reference Materials by High Resolution Inductively Coupled Plasma Mass Spectrometry, J. Anal. At. Spectrom. **12** (1997) 1181–1185.

[10] H. Kumagai, M. Yamanaka, T. Sakai, T. Yokoyama, Determination of trace metals in sea-water by inductively coupled plasma mass spectrometry interfaced with an ion chromatographic separation system, J. Anal. At. Spectrom. **13** (1998) 579–582.

[11] J.S. Oh, H. Yajima, K. Hashida, T. Ono, T. Ishijima, I. Serizawa, H. Furuta, A. Hatta, In-situ uv absorption spectroscopy for observing dissolved ozone in water, J. Photopolym. Sci. Technol. **29** (2016) 427–432.

[12] Q. Lu, S. Yang, D. Sun, J. Zheng, Y. Li, J. Yu, M. Su, Direct determination of Cu by liquid cathode glow discharge-atomic emission spectrometry, Spectrochim. Acta Part B At. Spectrosc. **125** (2016) 136–139.

[13] N.H. Tung, M. Chikae, Y. Ukita, P.H. Viet, Y. Takamura, Sensing technique of silver nanoparticles as labels for immunoassay using liquid electrode plasma atomic emission spectrometry, Anal. Chem. **84** (2012) 1210–1213.

[14] Y. Kohara, Y. Terui, M. Ichikawa, K. Yamamoto, T. Shirasaki, K. Kohda, T. Yamamoto, Y. Takamura, Atomic emission spectrometry in liquid electrode plasma using an hourglass microchannel, J. Anal. At. Spectrom. **30** (2015) 2125–2128.

[15] A. Kitano, A. Iiduka, T. Yamamoto, Y. Ukita, E. Tamiya, Y. Takamura, Highly sensitive elemental analysis for Cd and Pb by liquid electrode plasma atomic emission spectrometry with quartz glass chip and sample flow, Anal. Chem. **83** (2011) 9424–9430.

[16] T. Shih, W. Chen, Y. Sun, Open-channel chip-based solid-phase extraction combined with inductively coupled plasma-mass spectrometry for online determination of trace elements in volume-limited saline samples, J. Chromatogr. A. **1218** (2011) 2342–2348.

[17] V. Gamaleev, J. Oh, H. Furuta, A. Hatta, Investigation of Effect of Needle Electrode Configuration on Microplasma Discharge Process in Sea Water, IEEE Trans. Plasma Sci. **45** (2017) 754–760.

[18] V. Gamaleev, Y. Okamura, K. Kitamura, Y. Hashimoto, J.-S. Oh, H. Furuta, A. Hatta, Investigation of microplasma discharge in sea water for optical emission spectroscopy, Jpn. J. Appl. Phys. **55** (2016) 07LC03.

[19] V. Gamaleev, H. Furuta, A. Hatta, Detection of metal contaminants in seawater by spectral analysis of microarc discharge, Jpn. J. Appl. Phys. **57** (2018) 8–13.

[20] R. Burlica, M.J. Kirkpatrick, B.R. Locke, Formation of reactive species in gliding arc discharges with liquid water, J. Electrostat. **64** (2006) 35–43.

[21] P.H. Ceccato, O. Guaitella, M.R. Le Gloahec, A. Rousseau, Time resolved nanosecond imaging of the propagation of a corona-like plasma discharge in water at positive applied voltage polarity, J. Phys. D Appl. Phys. **43** (2010) 175202.

[22] K.K. Chiu, T. Sung, S. Teii, The energy consumption of decoloration by using pulsed discharge in water, Proc. Jt. Symp. APSPT-9/SPSM-28 (December 12 -15, 2015, Nagasaki Univ., Japan).

[23] Z. Mijatovic, D. Nikolic, R. Kobilarov, M. Ivkovic, STARK BROADENING OF THE HYDROGEN Hγ SPECTRAL LINE, Publ. Astron. Obs. Belgrade **89** (2010) 217–220.

[24] E. Stambulchik, A. Calisti, H. Chung, M.A. Gonzalez, Spectral Line Shapes in Plasmas, MDPI AG, Basel, Switzerland, 2015.

[25] M. Banno, E. Tamiya, Y. Takamura, Determination of trace amounts of sodium and lithium in zirconium dioxide (ZrO2) using liquid electrode plasma optical emission spectrometry, Anal. Chim. Acta. **634** (2009) 153–157.

[26] K. Tomita, S. Yoshitake, K. Uchino, D. Takenaka, H. Toda, M. Hikita, K. Suzuki, Measurements of Electron Density and Electron Temperature of Arc Discharge Plasmas Containing Metallic Vapors Using Laser Thomson Scattering, Electr. Eng. Japan. **188** (2014) 458–464.

[27] M. Kumai, Y. Takamura, Excitation temperature measurement in liquid electrode plasma, Jpn. J. Appl. Phys. **50** (2011) 96001.

[28] P. Šunka, Pulse electrical discharges in water and their applications, Phys. Plasmas. **8** (2001) 2587–2594.

[29] Y. Seepersad, M. Pekker, M.N. Shneider, D. Dobrynin, A. Fridman, On the electrostrictive mechanism of nanosecond-pulsed breakdown in liquid phase, J. Phys. D. Appl. Phys. **46** (2013).

[30] A. Starikovskiy, Pulsed nanosecond discharge development in liquids with various dielectric permittivity constants, Plasma Sources Sci. Technol. **22** (2013).

[31] R.P. Joshi, S.M. Thagard, Streamer-like electrical discharges in water: Part I. fundamental mechanisms, Plasma Chem. Plasma Process. **33** (2013) 1–15.

[32] D.H. Oza, R.L. Greene, D.E. Kelleher, Collisional broadening of the balmer-transition of H and He+ in plasmas, Phys. Rev. A. **37** (1988) 531–536.

[33] D. Van Khoai, H. Miyahara, T. Yamamoto, P.T. Tue, A. Okino, Y. Takamura, Development of AC-driven liquid electrode plasma for sensitive detection of metals, Jpn. J. Appl. Phys. **55** (2016) 02BC23.

[34] K. Schoenbach, J. Kolb, S. Xiao, S. Katsuki, Y. Minamitani, R. Joshi, Electrical breakdown of water in microgaps, Plasma Sources Sci. Technol. **17** (2008) 24010.

[35] V.M. Atrazhev, V.S. Vorob'ev, I. V. Timoshkin, M.J. Given, S.J. Macgregor, Mechanisms of impulse breakdown in liquid: The role of joule heating and formation of gas cavities, IEEE Trans. Plasma Sci. **38** (2010) 2644–2651.

[36] P. Xiao, D. Staack, Microbubble generation by microplasma in water, J. Phys. D. Appl. Phys. **47** (2014) 355203.

[37] I. V. Timoshkin, M.J. Given, M.P. Wilson, R.A. Fouracre, S.J. MacGregor, Impulse breakdown of liquid water, Annu. Rep. - Conf. Electr. Insul. Dielectr. Phenomena, CEIDP. 562 (2010) 10–12.

[38] V.Y. Ushakov, V.F. Klimkin, S.M. Korobeynikov, Impulse Breakdown of Liquid, Springer Berlin Heidelberg, Berlin, Germany, 2007.

[39] W. An, K. Baumung, H. Bluhm, Underwater streamer propagation analyzed from detailed measurements of pressure release, J. Appl. Phys. **101** (2007) 53302.

[40] I.M. Gavrilov, V.R. Kukhta, V. V. Lopatin, P.G. Petrov, Dynamics of prebreakdown phenomena in a uniform field in water, IEEE Trans. Dielectr. Electr. Insul. **1** (1994) 496–502.

[41] J.C. Devins, S.J. Rzad, R.J. Schwabe, Breakdown and prebreakdown phenomena in liquids, J. Appl. Phys. **52** (1981) 4531–4545.

[42] J. Qian, R.P. Joshi, J. Kolb, K.H. Schoenbach, J. Dickens, A. Neuber, M. Butcher, M. Cevallos, H. Krompholz, E. Schamiloglu, J. Gaudet, Microbubble-based model analysis of liquid breakdown initiation by a submicrosecond pulse, J. Appl. Phys. **97** (2005) 113304.

[43] Y. Seepersad, A. Fridman, D. Dobrynin, Anode initiated impulse breakdown in water: the dependence on pulse rise time for nanosecond and sub-nanosecond pulses and initiation mechanism based on electrostriction, J. Phys. D. Appl. Phys. **48** (2015) 424012.

[44] H.M. Jones, E.E. Kunhardt, The influence of pressure and conductivity on the pulsed breakdown of water, IEEE Trans. Dielectr. Electr. Insul. **1** (1994) 1016–1025.

[45] P. Bruggeman, C. Leys, Non-thermal plasmas in and in contact with liquids, J. Phys. D. Appl. Phys. **42** (2009) 53001.

[46] S. Sun, J. Li, Determination of Zr, Nb, Mo, Sn, Hf, Ta, and W in seawater by N-benzoyl-N-phenylhydroxylamine extraction chromatographic resin and inductively coupled plasma-mass spectrometry, Microchem. J. **119** (2015) 102–107.

[47] P. Bruggeman, T. Verreycken, M. Gonzalez, J. Walsh, M. Kong, L. Christophe, D. Schram, Optical emission spectroscopy as a diagnostic for plasmas in liquids : Opportunities and pitfalls, J. Phys. D. Appl. Phys. **43** (2010) 124005.

[48] T. Furusato, N. Ashizuka, T. Kamagahara, T. Fujishima, T. Yamashita, M. Sasaki, T. Kiyan, Spectroscopic Characteristics of Pulsed Arc Discharge in High-Pressure CO2 up to Supercritical Phase, 19th IEEE Int. Conf. Dielectr. Liq. (ICDL), Manchester, United Kingdom, 25 – 29 June, 2017. (2017) 1–4.

[49] P. Lindahl, M.J. Keith-roach, P.J. Worsfold, Ultra-trace determination of plutonium in marine samples using multi-collector inductively coupled plasma mass spectrometry, Anal. Chim. Acta. **671** (2010) 61–69.

[50] C. Miron, M.A. Bratescu, N. Saito, O. Takai, Time-resolved Optical Emission Spectroscopy in Water Electrical Discharges, Plasma Chem Plasma Process. **30** (2010) 619–631.

[51] P. Bruggeman, E. Ribezl, J. Degroote, J. Vierendeels, C. Leys, Plasma characteristics and electrical breakdown between metal and water electrodes, J. Optoelectron. Adv. Mater. **10** (2008) 1964–1967.

[52] P. Bruggeman, D.C.C. Schram, G.M. A, Y. Aranda, F. Iza, M.G.G. Kong, M.A. Gonzalez, Y.A. Gonzalvo, F. Iza, M.G.G. Kong, C. Leys, OPTICAL EMISSION SPECTROSCOPY OF PLASMAS IN AND IN CONTACT WITH LIQUIDS, III CESPC Proc. (2009) 21–24.

[53] Y.P. Raizer, Gas Discharge Physics, 1st ed., Springer-Verlag Berlin Heidelberg, 1991.

[54] R. Burlica, B. Hnatiuc, E. Hnatiuc, B. Locke, Hydrogen formation in pure water by non-thermal plasma treatment, ISPC19 Conf. Proc. (2009) 2.

[55] J.-S. Oh, M. Kakuta, H. Furuta, H. Akatsuka, A. Hatta, Effect of plasma jet diameter on the efficiency of reactive oxygen and nitrogen species generation in water, Jpn. J. Appl. Phys. **55** (2016) 06HD01.

[56] R. Burlica, B.R. Locke, A. Pulsed, Pulsed Plasma Gliding-Arc Discharges With Water Spray, IEEE Trans. Ind. Appl. **44** (2008) 482–489.

[57] H. Chu, C. Chung, Y. Liu, J. He, Micro-arc Oxidation Treatment on Aluminum under Pressurized Atmosphere, Proc. Jt. Symp. APSPT-9/SPSM-28 (December 12 -15, 2015, Nagasaki Univ., Japan).

[58] L. Matsuoka, K. Yuki, Y. Sonoyama, W. Sasano, S. Namba, Collisional Effects in Saturated Absorption Spectroscopy of Argon Arcjet Plasma, Proc. Jt. Symp. APSPT-9/SPSM-28 (December 12 -15, 2015, Nagasaki Univ., Japan).

[59] B. Jiang, J. Zheng, S. Qiu, M. Wu, Q. Zhang, Z. Yan, Q. Xue, Review on electrical discharge plasma technology for wastewater remediation, Chem. Eng. J. **236** (2014) 348–368.

[60] D.B. Fenneman, R.J. Gripshover, Experiments on Electrical Breakdown in Water in the Microsecond Regime, IEEE Trans. Plasma Sci. **8** (1980) 209–213.

[61] Y. Huang, L. Zhang, X. Zhang, Z. Liu, K. Yan, The Plasma-Containing Bubble Behavior Under Pulsed Discharge of Different Polarities, IEEE Trans. PLASMA Sci. **43** (2015) 1–5.

[62] P. Bruggeman, D. Schram, A. Manuel, R. Rego, M.G. Kong, C. Leys, Characterization of a direct dc-excited discharge in water by optical emission, Plasma Sources Sci. Technol. **18** (2009) 25017.

[63] Y. Jin, C. Cho, H. Ryoo, J. Kim, G. Rim, Long Gap Discharge in Water, J. Korean Phys. Soc. **59** (2011) 3640–3643.

[64] J. Degroote, P. Bruggeman, R. Haelterman, J.Vierendeels, Bubble simulations with an interface tracking technique based on a partitioned fluid- structure interaction algorithm, J. Comput. Appl. Math. **234** (2010) 2303–2310.

[65] H.H. Kim, Y. Teramoto, T. Hirakawa, N. Negishi, A. Ogata, Microbubble Formation in Underwater Pulsed Streamer Discharge, Int. J. Plasma Environ. Sci. Technol. **7** (2013) 109–114.

[66] H. Akiyama, E. Insulation, Streamer Discharges in Liquids and their Applications, lEEE Trans. Dielectr. Electr. Insul. **7** (2000) 646–653.

[67] S.P. Vetchinin, L.M. Vasilyak, V.Y. Pecherkin, V.A. Panov, E.E. Son, Spark discharge in conductive liquid with microbubbles, J. Phys. Conf. Ser. **774** (2016) 12183.

[68] J.E. Foster, B. Sommers, S. Gucker, Towards understanding plasma formation in liquid water via single bubble studies, Jpn. J. Appl. Phys. **54** (2015) 01AF05.

[69] H. Akiyama, Streamer Discharges in Liquids and their Applications, lEEE Trans. Dielectr. Electr. Insul. **7** (2000) 646–653.

[70] H. Nishiyama, R. Nagai, K. Niinuma, H. Takana, Characterization of Multiple Bubble Jet with Pulsed Discharge for Water Treatment, ISPC 19 Conf. Proc. (2009) 4–7.

[71] D. Medvedev, D. Sapunov, M. Demisky, S. Korobtsev, M. Krotov, B. Potapkin, Experimental study of a pulsed electric breakdown in conductive liquid, ISPC19 Conf. Proc. (2009).

[72] W. Bu, J. Zheng, Q. Guo, T. Aono, K. Tagami, Ultra-trace plutonium determination in small volume seawater by sector field inductively coupled plasma mass spectrometry with application to Fukushima seawater samples, J. Chromatogr. A. **1337** (2014) 171–178.

[73] Y.C. Sun, C.Y. Lin, S.F. Wu, Y.T. Chung, Evaluation of on-line desalter-inductively coupled plasma-mass spectrometry system for determination of Cr (III), Cr (VI), and total chromium concentrations in natural water and urine samples, Spectrochim. Acta Part B. **61** (2006) 230–234.

[74] P. Bruggeman, Plasma Chemistry and Catalysis in Gases and Liquids, First Edit, Wiley-VCH Verlag GmbH & Co. KGaA, 2012.

[75] Š. Potocký, N. Saito, O. Takai, Needle electrode erosion in water plasma discharge, Thin Solid Films. **518** (2009) 918–923.

[76] A. Kramida, Yu. Ralchenko, J. Reader, and NIST ASD Team, NIST Atomic Spectra Database (ver. 5.3), (National Institute of Standards and Technology, Gaithersburg, MD) [http://physics.nist.gov/asd] (accessed January 30, 2018).

[77] H.R. Griem, Principles of Plasma Spectroscopy, Cambridge University Press, Cambridge, 1997.

[78] J. Cooper, Plasma spectroscopy, Reports Prog. Phys. **29** (1966) 35–130.

[79] H.R. Griem, Spectral Line Broadening by Plasmas, Academic Press, New York, 1974.